ENERGY, ENVIRONMENT & STORAGE

AN INTERNATIONAL JOURNAL

Volume-5
Issue-3
September, 2025
ISSN: 2791-6197

Editor in Chief
Dr. Selahaddin Orhan AKANSU

ENERGY, ENVIRONMENT AND STORAGE

EES JOURNAL

Founded and Published by Erciyes Energy Association

Energy, Environment and Storage Journal is indexed in Crossref

Copyright ©

Printed in Turkey

ISSN-2791-6197

EES- EDITORIAL BOARD

BOARD MEMBER

VOLUME 5, ISSUE 5, REVIEWER BOARD

EDITORIAL OFFICE

AIM AND SCOPE

Energy, Environment and Storage papers consider the prospects of energy technologies, environment, materials, process control and industrial systems. The Energy, Environment and Storage will be published 3 times per year.

Contributions describe novel and significant applications to the fields of:

- Hydrogen Fuels
- Hydrogen and Fuel Cell
- Hydrogen Economic
- Biomass
- Solar PV Technology
- Solar Thermal Applications
- Wind Energy
- Materials for Energy
- Drones and Energy Applications
- Nuclear Energy and Applications
- Hydro Power
- Fuel Technologies (CNG, LNG, LPG, Diesel, Gasoline, Ethanol, etc.)
- Numerical Modelling
- Energy Storage and Systems
- Battery Technologies
- Energy Management
- Heat and Mass Transfer
- Aerodynamics
- Aerospace and Energy Applications
- Combustion
- Electric Vehicle Transportation
- Off-grid Energy Systems
- Environment Management
- Air Pollution
- Water and Wastewater Pollution
- Water and Wastewater Management
- Waste Management
- Global Warming and Climate Change
- Environmental Ecosystem
- Environmental System Modelling and Optimization
- Ecological Applications or Conservation

VOLUME 5, ISSUE 3

SEPTEMBER 2025

CONTENTS

Energy, Environment and Storage

Journal Homepage: www.enenstrg.com

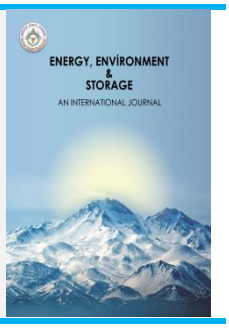

Overview and evaluation of Biogas, Biomethane, and Purification Methods

Volkan Sabri Kül[1*]

[1*]*Erciyes University, Graduate School of Natural and Applied Sciences, (Department of Mechanical Engineering), Kayseri, Türkiye, volkanskul@gmail.com, ORCID:0000-0002-6412-6062,*

ABSTRACT. Biogas and biomethane are renewable gases that should be strongly considered to accelerate decarbonization and reduce greenhouse gas emissions in many sectors. In addition, biomethane is important to provide renewable and more economical energy to consumers using the existing gas infrastructure. Moreover, biomethane can be easily stored and can be used as a balancer for intermittent renewable energy sources such as solar and wind. The EU considers bio-CNG (compressed), bio-LNG (liquefied) fuels to be an effective method in reducing emissions. Therefore, Europe leads the world in biogas and biomethane production. In this study, evaluations and general views were made about the definition of biogas and biomethane, production amounts in the world and purification methods (treatment) of biogas. The main purpose of the current study is to emphasize that biogas provides an important solution for decarbonization and that its usage areas can be expanded by purifying it as biomethane.

Keywords: Biogas, Bomethane, Purilification, Decarbonization

Article History: Received 16.04.2025; Revised: 17.052025; Accepted:18.05.2025; Availableonline: 18.05.2025
Doi: https://doi.org/10.52924/WQUK5640

1. INTRODUCTION

Increasing global energy demand and the rise of global warming have increased the importance of renewable energy sources. According to the "BP World Energy Statistical Review 2022, 71st edition" report, while total world energy consumption was 587 EJ in 2019, it decreased to 564 EJ in 2020 due to the COVID-19 pandemic, which had a global impact. However, with the global recovery from the pandemic, total world energy consumption increased to 595 EJ in 2021, exceeding the consumption of 2019 [1]. According to the "Energy Institute Statistical Review of World Energy 2024, 73rd edition" report, total world energy consumption continued to rise. According to this report, total world energy consumption was 607 and 620 EJ in 2022 and 2023, respectively [2]. In these reports, the sources that meet the world's energy needs in all years are oil, coal and natural gas, respectively. On the other hand, when comparing the data of 2019 and 2023, the change in the resources that meet the world's energy needs is seen as nuclear energy, hydroelectricity, oil, natural gas, coal, renewables energy -3.5, -1.2, 2.2, 2.7% 4.3% 59.4%, respectively. Despite the decrease in hydroelectricity and nuclear energy, the rates of hydroelectricity, oil, natural gas, coal, and renewable energy resources in meeting the world's energy needs have increased. The increase rate of renewable energy sources is striking (Table 1 and Figure 1.a) [1].

Table 1. Primary energy consumption

Exajoules (10^{18} Joule)	**2019**	**2020**	**2021**	**2022**	**2023**	**Energy consumption growth rate between 2019-2023**
Nuclear Energy	25.5	24.4	25.3	24.1	24.6	**-3.5%**
Hydro Electricity	40.2	41.1	40.3	40.6	39.7	**-1.2%**
Oil	192.1	174.2	184.2	191.6	196.4	**2.2%**
Natural Gas	140.6	138.4	145.4	144.3	144.4	**2.7%**
Coal	157.3	151.1	160.1	161.5	164.0	**4.3%**
Renewables	31.7	34.8	39.9	45.2	50.6	**59.4%**
Total	**587.43**	**564.01**	**595.14**	**607.35**	**619.63**	**5.48%**

* volkanskul@gmail.com@gmail.com

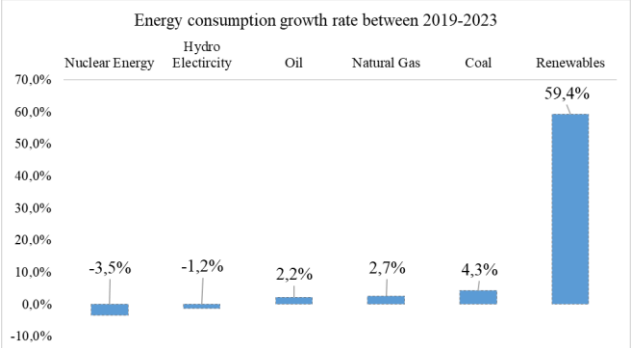

Fig. 1.a. Energy consumption growth rate between 2019-2023

The percentage change of the resources that meet the annual energy consumption by years is presented in Fig1b. According to this figure, it is clearly seen that while the rates of other energy resources other than renewable energy resources fluctuate over the years and can be considered relatively constant, renewable energy resources increase their place in annual energy consumption linearly.

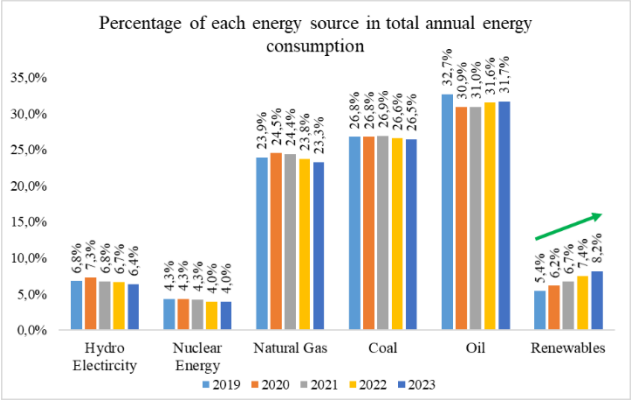

Fig. 1.b. Energy consumption growth rate between 2019-2023

Another report supporting these results, "U.S. According to the Energy Information Administration (EIA), the International Energy Outlook 2019 report, it is predicted that the world energy need will increase by 50% in 2050, and the Asian continent will have the largest share in this increase. According to the same report, it is emphasized that renewable energy sources will be the primary energy source in 2050 [3] (Fig.2).

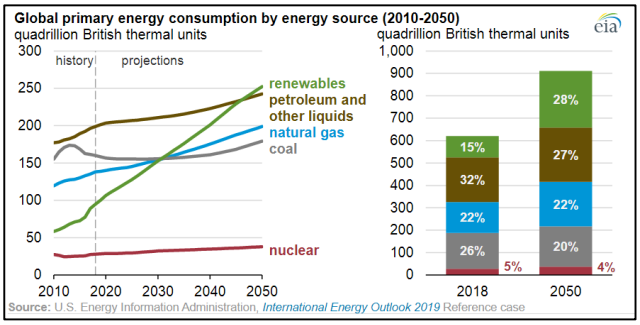

Fig. 2. Global primary energy consumption by energy source 2010-2050 (Source: U.S. Energy Information Administration, International Energy Outlook 2019 Reference case) [3]

Solar and wind energy are the leading sources of renewable energy. However, the production of biofuels as another renewable energy source is increasing rapidly. While the total production of bio gasoline and bio diesel was 1174 tboe/d in 2011, it increased to 1747 tboe/d (Thousand barrels of oil equivalent per day) in 2021 [1]. The amount of energy produced from biogas in the world (electricity production capacity) increased from 9.3 GW in 2010 to 17.7 GW in 2018. According to the IEA (2018) report, biogas production today is approximately 35 Mtoe. 3.5 Mtoe of the biogas production amount is converted into biomethane (Mtoe=11.63 TWh) [4].

As can be understood from the reports, the world attaches great importance to renewable energy sources. In addition, in 2015, in the Paris Agreement at COP21, it was decided to reduce greenhouse gas emissions and keep global warming below 1.5 degrees Celsius compared to pre-industrial levels. This decision increases the importance of renewable energy sources [5].

In this report, Biogas and Biomethane, one of the renewable energy sources whose importance is increasing rapidly, will be discussed. Biogas is the first product of an anaerobic digestion plant. It consists primarily of methane and can be used to generate heat or electricity. Biogas generally contains 45% - 85% methane (CH_4) and 25% - 50% carbon dioxide (CO_2). After biogas is purified (explained in detail in section 4) from other compounds such as nitrogen dioxide (CO_2), oxygen dioxide (O_2), hydrogen sulfide (H_2S) or water vapour (H_2O), it turns into biomethane, which consists almost entirely of methane, between 95% - 99%. As mentioned above, the main difference between biogas and biomethane is related to the amount of methane it contains. The main purpose of the current study is to emphasize that biogas provides an important solution for decarbonization and that its usage areas can be expanded by purifying it as biomethane.

2. BIOGAS AND BIOMETHANE

Biogas is formed by the biodegradation of organic wastes in an oxygen-free environment. Potential feedstocks to produce biogas are biological waste materials, agricultural residues from some plants, grains and crops, animal manure, algae biomass, food waste, municipal waste, fruit and vegetable waste, and raw materials such as cellulose-containing substrates (Fig. 3) [6].

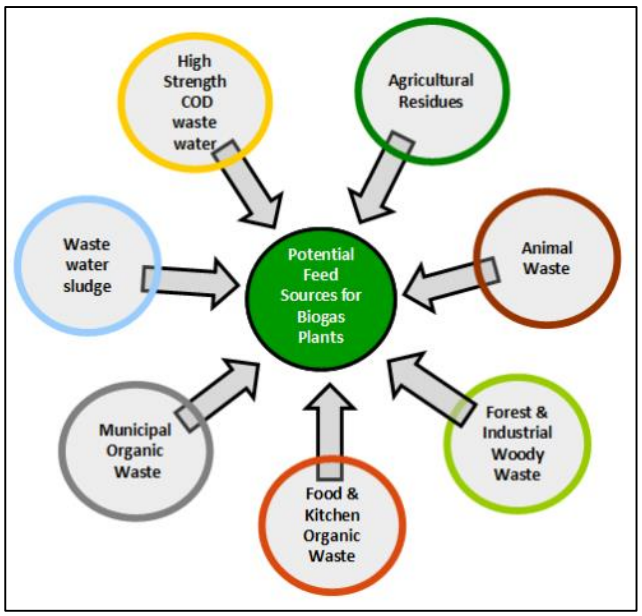

Fig. 3. Biogas raw materials [6]

The feedstock types actually used for biogas production in the worldwide are shown in Fig. 4. According to the IEA's report (2018), biogas currently production is about 35 Mtoe (Mtoe=11,63 TWh). Europe takes the first place in biogas production and the most frequently used feedstocks are Crops, Animal manure and municipal waste [4].

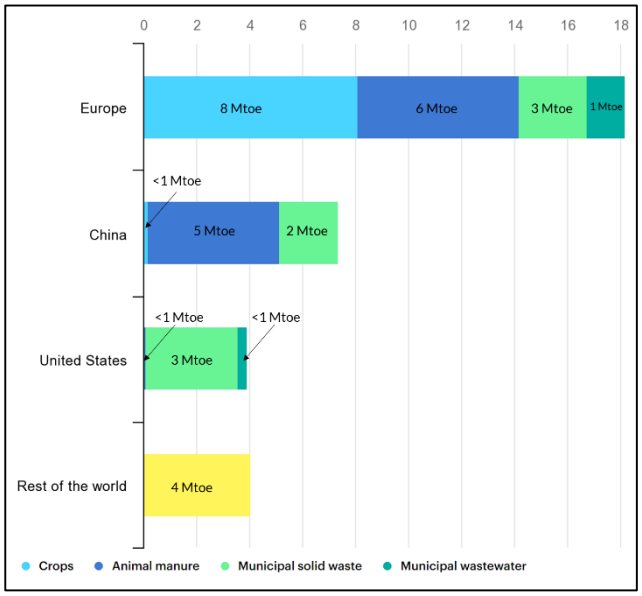

Fig. 4. Biogas production by region and by feedstock type, 2018 [4]

The substances in the biogas may differ according to the raw material used during anaerobic digestion. The main components of biogas are 55-70% methane and 30-40% carbon dioxide. In addition, biogas contains pollutants such as moisture (H2O), siloxanes, VOC (volatile organic compounds), NH3, O2, N2, and CO. The ratio of these ingredients may vary depending on the type of raw material. For example, while the ratio of H2S and NH3 is high in biogas produced from farm waste, siloxanes are high in biogas produced from sewage waste [7,8]. The lower heat value of methane gas (LHVmethane) is 49.93 kJ/kg. The biogas lower heat value can be calculated according to this equation 1, [9]. The LHV value of biogas with 70% methane content can be calculated as 34.95 kJ/kg.

$$LHV_{biogas}=LHV_{methane}\ x\%CH_4 \quad (1)$$

Biomethane can be obtained by applying various purification and upgrading techniques to Biogas. After these processes, Biomethane containing 95-97% methane can be obtained [8, 10]. Fig. 5 shows the usage areas of biogas and Biomethane. While biogas generally can be used for heating and electricity generation without enrichment, for vehicles and natural gas pipelines have to be use Biomethane.

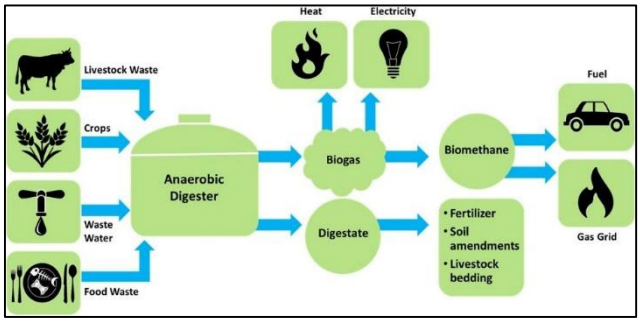

Fig. 5. Biogas and Biomethane usage areas [11]

3. FORMATION OF BIOGAS

Anaerobic digestion consists of three main processes (Fig. 6). These are Hydrolysis, Acidification and methanogenic processes. These three processes occur simultaneously in the digestion reactor. But these biochemical processes develop in conjunction with each other. Because the substrate of one process is the food of another process. Methane is produced in large quantities in the last phase. The first process of anaerobic digestion is hydrolysis. In this process, carbohydrates, fats, and proteins are converted into long-chain sugars, fatty acids, and amino acids. The second process, the acidification phase, can be examined in two separate groups as acidogenesis and acetogenesis. Acidogenesis bacteria convert the long sugar chains, amino acids and fatty acids formed in the hydrolysis process into alcohols, CO2, H2, VFA (Volatile Fatty Acid), Propionic, acetic and butyric acids. Acetogenesis bacteria convert acetogenesis products to acetates, CO2 and H2. In the last process, methanogenesis, methanogenic bacteria produce 70% of methane from acetate and the rest from H2- CO2 conversion. The most sensitive process is methanogenesis because methanogenic bacteria are very sensitive to parameters such as temperature, pH value and feeding rate. In this way, biogas is produced, all these processes take place at the same time during biogas production, so process monitoring should be done very well in the facilities [12, 13, 14].

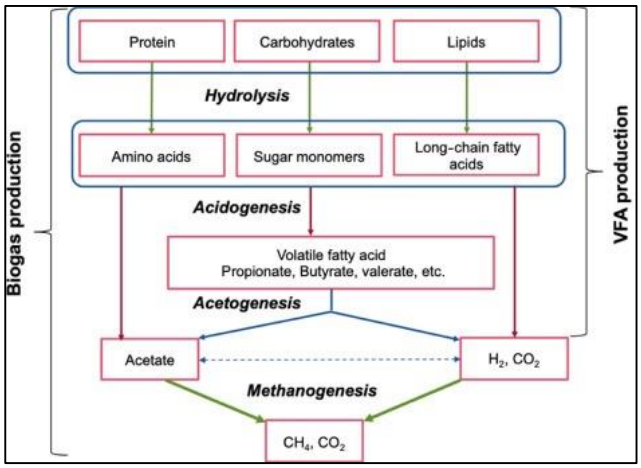

Fig. 6. Formation of Biogas [12]

4. Biogas Purification and Upgrading Methods to Convert to Biomethane

There are basically two ways to produce Biomethane, upgrading biogas and Biomass gasification [15]. Biomass gasification is a process applied to produce Biomethane from dry woody biomass. It consists of stages such as drying, pyrolysis and gasification. There are two equal gasification management. High temperature gasification is done above 1300 degrees Celsius, while low temperature gasification is not done at 800 - 1000 degrees Celsius. Low-temperature gasification is more efficient [16, 17]. Upgrading biogas is the process of removing carbon dioxide and other pollutants from biogas containing around 60% methane and bringing the methane ratio to 95% and above [18]. Currently, 3.5 Mtoe (Mtoe=11.63 TWh) Biomethane is produced worldwide. 90% of this Biomethane produced was obtained by upgrading Biogas [4] (Fig. 7).

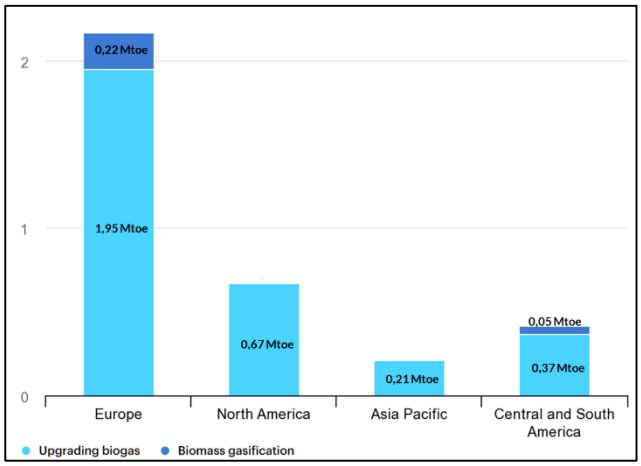

Fig. 7. Biomethane production that is upgraded in selected regions, 2018 [4]

Before biogas can be used, it must be cleaned to protect equipment such as engines, storage tanks and pipelines. We can divide this cleaning process into two main groups as purification and upgrading. Purification is done to remove various pollutants such as Sulphur, while upgrading is done to increase methane content. After upgrading, the biogas converts to Biomethane. Since Biomethane is rich in methane content, it is a gas that can be used in natural gas pipeline [19].

According to the IEA Bioenergy Technology Collaboration Program - Upgrading Plant List 2019 report, there are 673 upgrading plants that produce biomethane by increasing the methane concentration of the biogas to 96% by using various upgrading methods (Fig. 8). Germany ranks first in the world in terms of the number of plants that produce biomethane by upgrading biogas [20].

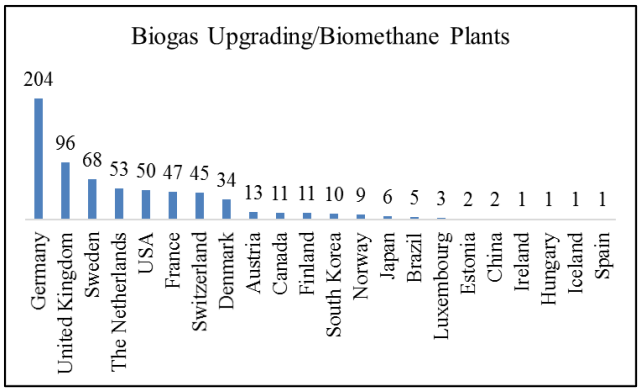

Fig. 8. Biogas Upgrading/Biomethane Plants

Of the 673 plants cited in the report, the upgrading methods 601 used to produce biomethane were cited. Considering these 601 facilities, it is seen that the most used upgrading methods to produce biomethane are water scrubbing (32%), membrane separation (30%), chemical/amine scrubbing (18%), pressure swing adsorption (PSA, 14%), organic physical scrubbing (3%) and cryogenic upgrading (2%), (Fig. 9). Most of the biomethane produced by different upgrading methods is used in natural gas grid. In addition, 11% of the biomethane produced is used as vehicle fuel (Fig. 10), [20].

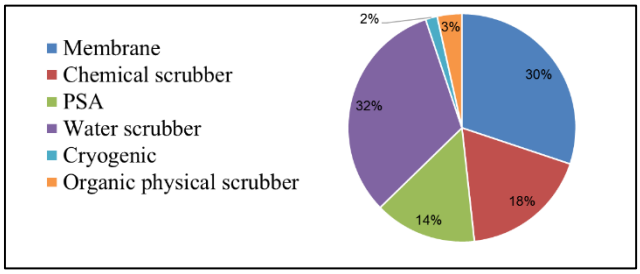

Fig. 9. Upgrading methods used in the world

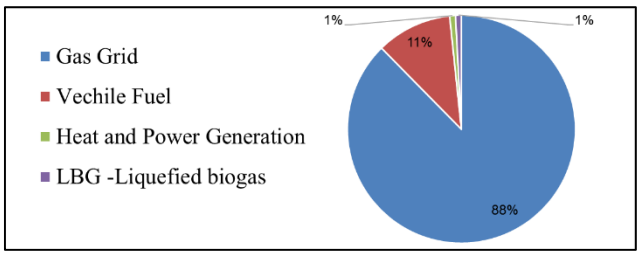

Fig. 10. Utilizations of Biomethane

4.1. Biogas Purification

4.1.1 Desulphurization (Removal of H_2S)

H2S is a very harmful and toxic gas for human health. May cause damage to the blood, nervous and respiratory systems. It is colorless and has a rotten egg odor. It is explosive when reacted with oxygen. When burned, it produces corrosive and environmentally harmful emissions [21]. According to EN 16723-1:2016 and EN16723-2:2017 standards, a maximum of 20 and 5 mg/m3 of sulfur is allowed in the biogas content, respectively. Techniques such as microaeration, adsorption, absorption and biofiltration are used to purify H2S.

I. Microaeration

The purification of H2S is an effective and simple method in the production of biogas by anaerobic digestion. In this method, it is aimed to oxidize sulfur and turn it into elemental base by giving oxygen to the digester in a controlled manner. Elemental sulfur can then be taken from the digester along with the sludge [22].

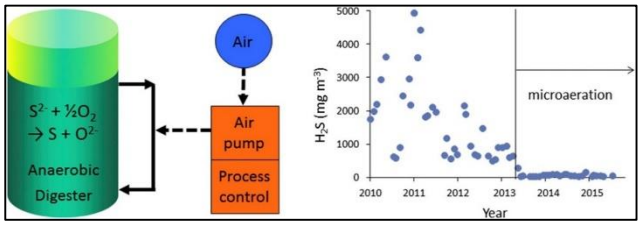

Fig. 11. Microaeration, 2018 [22]

II. Adsorption Method for Removal H2S

It is the collection of one or more substances on a surface to form a film layer and bonding with van der Waals forces. It can occur at gas/solid, liquid/solid, or immiscible liquid/liquid interfaces. The presence of any substance on a liquid or solid surface in a higher concentration than the main phase is called adsorption. The substance whose concentration increases on the liquid or solid surface is called adsorbate, and the substance that adsorbs is called adsorbent [23]. Activated carbon and sodium hydroxide washing are the methods used for adsorption [18]. Fig. 12 shows the application of microaeration and adsorption methods together.

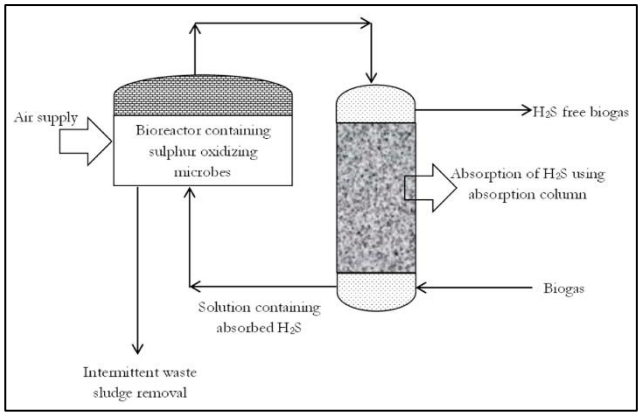

Fig. 12. Application of microaeration and adsorption methods together [24]

III. Absorption Method for Removal H_2S

Removal of H_2S with this method is based on the direct washing of biogas with water or its interaction with suitable organic solvents. H_2S is absorbed by water and converted to elemental sulfur. This method is also called the water scrubbing method [24].

IV. Bio filters

The biofilter consists of filtered microorganisms in the form of a film. Mixtures of substances such as soil, peat and manure form the content of the biofilter. By biofiltration, H_2S in biogas is converted into oxygen and biomass, carbon dioxide, metabolic by-products and sulfur monoxide with the help of microbes in the biofilter [25].

It is very important to remove H_2S from Biogas. However, other pollutants that must be removed from biogas include halogens, oxygen, nitrogen and siloxanes.

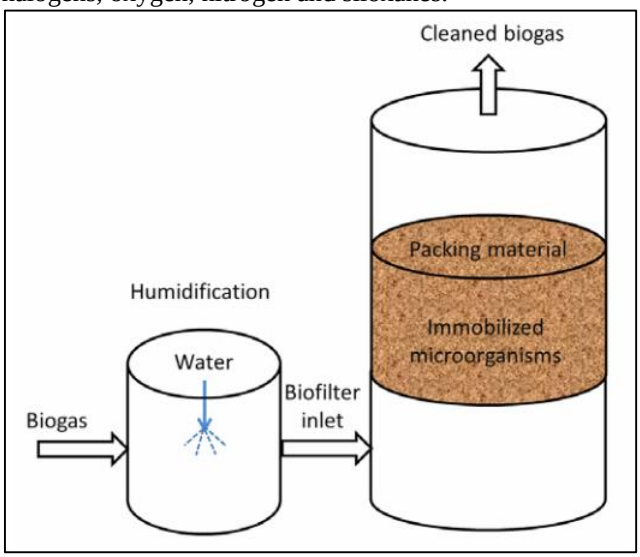

Fig. 13. Representation of a biofilter [26]

4.1.2 Water Removal

The removal of water is important in terms of preventing corrosion at the gas usage points. The water removal method can be considered in two ways as physical and chemical drying. The physical drying method is based on the logic of cooling and condensation. Condensed water droplets are collected and removed. It can be used in cyclone separators by making use of centrifugal force. In addition, the condensed water from the taps in the biogas pipes can be collected and removed. Chemically drying is done by adsorption and absorption methods. Silica, activated carbon, aluminum oxide or magnesium oxide can be used for drying in the absorption method. In the absorption method, water is removed by using triethylene glycol and hygroscopic salts [8]. Biogas purification methods are shown in Table 2 comparatively.

Table 2. Comparison of biogas purification methods [19]

Method	H_2S removal efficiency	Approximate annual operating cost (€/ [1000 Nm^3/h])	Advantages	Disadvantages
In-situ microaeration	90 – 99 %	20 300	• No additional costs for separate unit • No addition	• Elemental sulphur can be oxidized to sulphates which limits CH_4 content •Suphuric acid can form causing corrosion in the digester
Impregnated activated carbon	95 – 99 %	% (overall adsorption cost) 60 000	• 40 – 60 times more efficient than activated carbon • Can remove multiple contaminants (H_2S, siloxanes, water)	• Decreases ignition temperature of carbon which can cause it to self-ignite • Difficult to regenerate
Iron oxide	99.98 %		• Highly effective and efficient method	• High operation costs • Highly chemical intensive
In-situ chemical precipitation (iron salts)	N.A	70 000	• Easy to monitor, handle and implement	• Difficult to control degree of H_2S removal • Can impede formation of CH_4
Bio scrubber	98%	130 000	• Can be used for biogas with up to 30 000 mg/m^3 H_2S • Highly efficient with little clogging issue	• High operation costs • Difficult to achieve efficiencies >98 % • Can wash off slow growing microorganisms
Biofilter	90 – 99 %	560 000	• Low energy and equipment requirements • No additional chemicals	• Accumulation of biomass on surface • Large carbon footprint
Bio-trickling filter	100 – 200 ppm	100 000	• No CH_4 depletion • No additional chemicals • Methane enrichment (conversion of CO_2 to CH_4)	• High amount of air bubbles in the biogas

4.2. Biogas Upgrading

4.2.1. Water Scrubbing

This method takes advantage of the solubility difference of methane and carbon dioxide in water. According to Henry's law, the solubility of carbon dioxide in water at 25 degrees Celsius is 0.034 M/atm, while the solubility of methane is 0.0013 M/atm. In other words, carbon dioxide is much more water-soluble than methane. Since this solubility difference will be better at low temperature and high pressure, this environment should be tried to be provided in the water scrubbing method. In this method, biogas is compressed around 6 bars after H2S removal. While the biogas is supplied to the absorption tank from the bottom side, the water is sprayed from the top side. Thus, while carbon dioxide dissolves in water, methane can be taken from the top of the tank. The methane from the top of the tank can be compressed into gas line pressure with a methane ratio of around 98% after drying and purification from Volatile Organic Compounds. During washing, about 5% methane and carbon dioxide can be dissolved in water. For this reason, this water is taken into a flash tank with 2-4 bar pressure. In this flash tank, methane is separated and circulated. The water saturated with the remaining carbon dioxide is taken into a desorption tank. Here, carbon dioxide is separated from the water and the water is sent back to reuse. About 3% of methane may be lost in the result of this method [27-29].

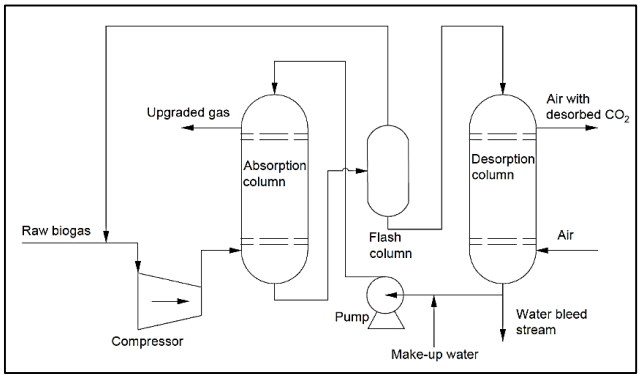

Fig. 14. Water Scrubbing [30]

4.2.2. Organic Physical Scrubbing

Organic physical scrubbing method is very similar to water scrubbing method. Organic solvents such as polyethylene glycol are used in this method. Because carbon dioxide is more soluble in these solvents than water. In this method, the flash tank used in the water scrubbing method is not used. Commercial liquids with names such as Selexol and Gensorb are used in biogas upgrading plants [18, 29].

4.2.3. Chemical/Amine Scrubbing

The amine scrubbing method is similar to the water scrubbing method in terms of operation. However, in this method, organic amines such as diethanolamine, diglycolamine, monoethanolamine and ethyldiethanolamine are used as solvents instead of water. These amines absorb more carbon dioxide than water and can work efficiently even at atmospheric pressure. Therefore, in this method, the biogas may not be compressed before scrubbing [27, 29].

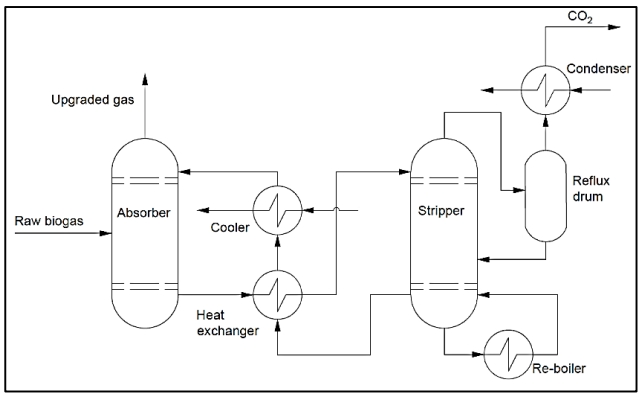

Fig. 15. Chemical/Amine Scrubbing [30]

4.2.4. Pressure Swing Adsorption (PSA)

In this method, adsorbing materials such as silica gels, activated carbon and zeolites are used at high pressure. When the adsorbing material becomes saturated in a tank, the raw gas is sequentially taken to another tank where the adsorber is regenerated, and the pressure is sequentially reduced. In this way, carbon dioxide is removal from the biogas [18, 31, 32].

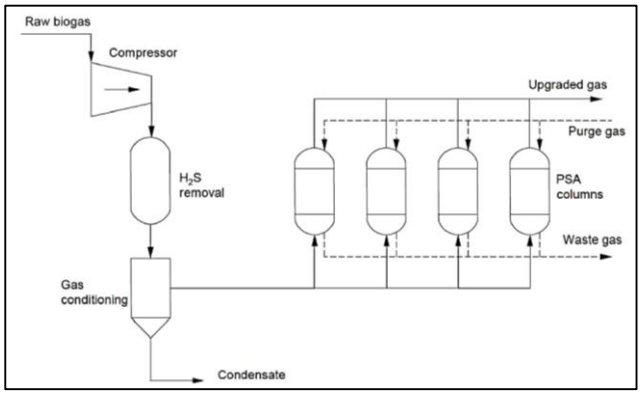

Fig. 16. Pressure Swing Adsorption [29]

4.2.5. Membrane Separation

In this method, different chemical structures are separated along a membrane according to their velocity. Before the raw biogas enters the membrane, the water and H2S in it are removed. Carbon dioxide separation is made in the membrane to a large extent. Unlike other upgrading methods, higher pressure is used in the membrane method. The pressure used is at the level of 9-19 bars [29].

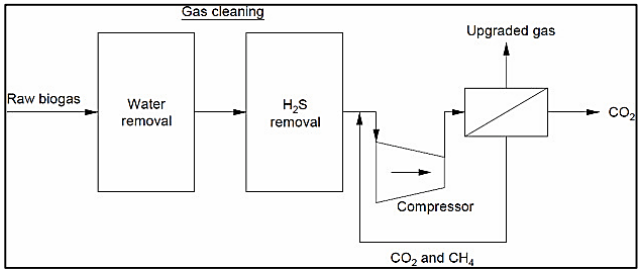

Fig. 17. The Membrane Separation [29]

4.2.6. Cryogenic Upgrading

Cryogenic upgrading is the separation process by utilizing different liquefaction temperatures of the components in the biogas. There are two different application methods. The first is based on a gradual reduction in temperature, keeping the pressure constant at 10 bars. First, the biogas is cooled to -25 degrees Celsius. At this temperature, water, H2S and siloxanes are separated. Afterwards, it is cooled to -55 degrees Celsius and carbon dioxide decomposition begins. By reaching -85 degrees, almost all of the carbon dioxide is decomposed [33]. The second method is again based on the liquefaction of gases at different pressures and temperatures. With this method, in order to remove carbon dioxide from the biogas, the gas is cooled down to -75, -85 degrees Celsius and compressed to a pressure of 80, 110 bar at the same time. Since this process is done gradually, carbon dioxide and methane can be easily separated from each other because they have different liquefaction conditions. Biomethane containing 99% pure methane can be produced by cryogenic upgrading method. Methane loss during upgrading is less than other methods, but requires more equipment [33-35].

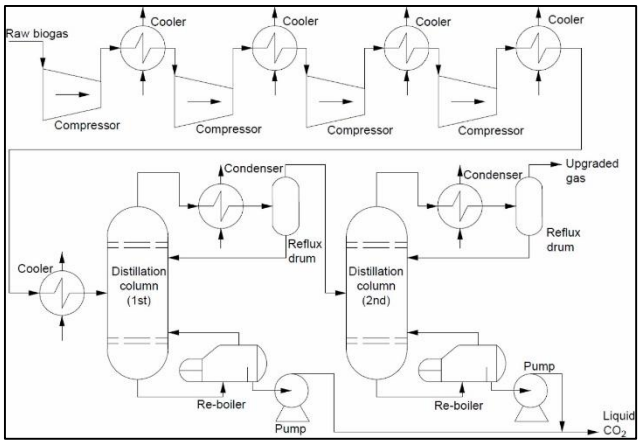

Fig. 18. Cryogenic Upgrading [29]

Table 3 shows the parameters of biogas upgrading methods comparatively. This table also indicates the requirements, efficiency and operating conditions of the upgrading methods.

Table 3. Comparison of biogas upgrading methods [18, 19]

Parameters	PSA	Water Scrubbing	Organic Physical Scrubbing	Chemical/ Amine Scrubbing	Membrane Separation	Cryogenic Upgrading
Pre-cleaning /H_2S removal	Yes	No	No	Yes	Possible	No
Working pressure (bar)	4 - 7	4 - 7	4 - 7	No pressure	9 - 19	80 - 110
Methane loss	<3%	<2%	<4%	<0.5%	<5%	<0.1%
Heat requirement (°C)	No	No	55 - 80	160		(-75) / (-80)
Methane content in upgraded gas	96 - 98%	95 - 98%	93 - 98%	99%	90 - 99%	99%
Electricity consumption (kWh/Nm^3)	0.25	<0.25	0.24 - 0.33	<0.15	0.18- 0.35	0.18 - 0.25

5. CONCLUSION

In this study, the change in world energy consumption, the place of renewable energy in world annual energy consumption and biogas and biomethane, which are increasingly important renewable energy sources, were examined.

1- While the world's annual energy consumption was 587.43 EJ in 2019 (before the Covid 19 pandemic), it increased by 5.48% and reached 619.63 EJ in 2023.

2- The amount of renewable energy resources in the world's annual energy consumption increased from 31.7 EJ in 2019 to 50.6 EJ in 2023, an increase of 59.4%.

3- The electricity generation capacity from biogas, which is among the renewable energy sources, was increased from 9.3 GW in 2010 to 17.7 GW in 2018.

4- Approximately 35 Mtoe of Biogas was produced in the world in 2018. Some of this amount was upgraded to 3.5 Mtoe of biomethane (1 Mtoe = 11.63 Twh).

5- Biogas is mostly produced in Europe. Following Europe, China and the USA come respectively. Germany has the most facilities in the world that upgrade and convert biogas into biomethane.

6- The methods used in the world to upgrade biogas to biomethane are water scrubber, membrane, chemical scrubber, PSA, organic physical scrubber and cryogenic, respectively.

7- Biogas and biomethane production, which are among the renewable energy sources, are promising for the future according to published international reports.

REFERENCES

[1] BP Statistical Review of World Energy2022 | 71st edition, https://www.bp.com/content/dam/bp/business-sites/en/global/corporate/pdfs/energy-economics/statistical-review/bp-stats-review-2022-full-report.pdf, [accessed 30 April 2025]

[2] Energy Institute Statistical Review of World Energy 2024, 73. Edition | 73st edition, https://www.energyinst.org/statistical-review/resources-and-data-downloads [accessed 30 April 2025]

[3] U.S. Energy Information Administration (EIA), International Energy Outlook 2019, https://www.eia.gov/todayinenergy/detail.php?id=41433 , [accessed 30 April 2025]

[4] IEA – International Energy Agency, Outlook for biogas and Prospects for organic growth, World Energy Outlook Special Report https://www.iea.org/reports/outlook-for-biogas-and-biomethane-prospects-for-organic-growth/an-introduction-to-biogas-and-biomethane , [accessed 30 April 2025]

[5] United Nations Framework Convention on Climate Change (UNFCCC). The Paris Agreement, https://unfccc.int/process-and-meetings/the-paris-agreement/the-paris-agreement , [accessed 30 April 2025]

[6] Minde, G., Magdum, S., & Kalyanraman, V. (2013). Biogas as a sustainable alternative for current energy need of India. Journal of Sustainable Energy & Environment, 4, 121-132.

[7] Malode, S. J., Prabhu, K. K., Mascarenhas, R. J., Shetti, N. P., & Aminabhavi, T. M. (2021). Recent advances and viability in biofuel production. Energy Conversion and Management: X, 10, 100070. https://doi.org/10.1016/j.ecmx.2020.100070

[8] Ryckebosch, E., Drouillon, M., & Vervaeren, H. (2011). Techniques for transformation of biogas to biomethane. Biomass and bioenergy, 35(5), 1633-1645. https://doi.org/10.1016/j.biombioe.2011.02.033

[9] Braga, L. B., Silveira, J. L., Da Silva, M. E., Tuna, C. E., Machin, E. B., & Pedroso, D. T. (2013). Hydrogen production by biogas steam reforming: a technical, economic and ecological analysis. Renewable and Sustainable Energy Reviews, 28, 166-173. https://doi.org/10.1016/j.rser.2013.07.060

[10] Beil, M., & Beyrich, W. (2013). Biogas upgrading to biomethane. In The biogas handbook (pp. 342-377). woodhead publishing. https://doi.org/10.1533/9780857097415.3.342

[11] Environmental and Energy Study Institute https://www.eesi.org/papers/view/fact-sheet-biogasconverting-waste-to-energy [accessed 11 January 2023]

[12] Kendir Çakmak, E. C. E., Atasoy, M., Owusu-Agyeman, I., Khatami, K., & Cetecioglu, Z. (2021). 19. Circular city concept for future biorefineries. https://doi.org/10.1016/B978-0-323-90178-9.00009-3

[13] Atelge, M. R., Krisa, D., Kumar, G., Eskicioglu, C., Nguyen, D. D., Chang, S. W., & Unalan, S. (2020). Biogas production from organic waste: recent progress and perspectives. Waste and Biomass Valorization, 11(3), 1019-1040. https://doi.org/10.1007/s12649-018-00546-0

[14] Categorization of European Biogas Technologies, https://www.europeanbiogas.eu/wp-content/uploads/2021/11/BioGas_AD_Final.pdf [accessed 30 April 2025]

[15] World Energy Outlook 2019 https://iea.blob.core.windows.net/assets/98909c1b-aabc-4797-9926-35307b418cdb/WEO2019-free.pdf [accessed 30 April 2025]

[16] Åhman, M. (2010). Biomethane in the transport sector—An appraisal of the forgotten option. Energy Policy, 38(1), 208-217. https://doi.org/10.1016/j.enpol.2009.09.007

[17] Safarian, S., Unnþórsson, R., & Richter, C. (2019). A review of biomass gasification modelling. Renewable and Sustainable Energy Reviews, 110, 378-391. https://doi.org/10.1016/j.rser.2019.05.003

[18] Petersson, A., & Wellinger, A. (2009). Biogas upgrading technologies–developments and innovations. IEA bioenergy, 20, 1-19.

[19] Mwacharo, F., Bhandar, S., Othman, A., & Rautio, A. R. (2020). Biogas drying and purification methods. https://urn.fi/URN:ISBN:978-952-7173-55-8

[20] The IEA Bioenergy Technology Collaboration Program - Upgrading Plant List 2019 Report, https://task37.ieabioenergy.com/plant-lists/ [accessed 30 April 2025]

[21] Atelge, M. R., Senol, H., Djaafri, M., Hansu, T. A., Krisa, D., Atabani, A., ... & Kıvrak, H. D. (2021). A Critical Overview of the state-of-the-art methods for biogas purification and utilization processes. Sustainability, 13(20), 11515. https://doi.org/10.3390/su132011515

[22] Jeníček, P., Horejš, J., Pokorná-Krayzelová, L., Bindzar, J., & Bartáček, J. (2017). Simple biogas desulfurization by microaeration–Full scale experience. Anaerobe, 46, 41-45. https://doi.org/10.1016/j.anaerobe.2017.01.002

[23] Králik, M. (2014). Adsorption, chemisorption, and catalysis. Chemical Papers, 68(12), 1625-1638. https://doi.org/10.2478/s11696-014-0624-9

[24] Okoro, O. V., & Sun, Z. (2019). Desulphurisation of biogas: a systematic qualitative and economic-based quantitative review of alternative strategies. ChemEngineering, 3(3), 76. https://doi.org/10.3390/chemengineering3030076

[25] Devinny, J., Deshusses, M., & Webster, T. 1998. Biofiltration For Air Pollution Control. New York , London: CRC Press, 22–318.

[26] Eric Dumont. H2S removal from biogas using bioreactors: a review. International Journal of Energy and Environment, 2015, 6 (5), pp.479-498. HAL Id: hal-01945143 https://hal.archives-ouvertes.fr/hal-01945143

[27] Ardolino, F., Cardamone, G. F., Parrillo, F., & Arena, U. (2021). Biogas-to-biomethane upgrading: A comparative review and assessment in a life cycle perspective. Renewable and Sustainable Energy Reviews, 139, 110588. https://doi.org/10.1016/j.rser.2020.110588

[28] Bauer, F., Hulteberg, C., Persson, T., & Tamm, D. (2013). Biogas upgrading-Review of commercial technologies; Biogasuppgradering-Granskning av kommersiella tekniker.

[29] Lim, Y. F., Chan, Y. J., Abakr, Y. A., Sethu, V., Selvarajoo, A., Singh, A., ... & Gareth, M. (2021). Review of biowastes to energy in Malaysia: Current technology, scalability and socioeconomic analysis. Cleaner Engineering and Technology, 4, 100257. https://doi.org/10.1016/j.clet.2021.100257

[30] Hoyer, K., Hulteberg, C., Svensson, M., Jernberg, J., & Nörregård, Ö. (2016). Biogas upgrading-technical review.

[31] Gomes, V. G., & Yee, K. W. (2002). Pressure swing adsorption for carbon dioxide sequestration from exhaust gases. Separation and purification technology, 28(2), 161-171. https://doi.org/10.1016/S1383-5866(02)00064-3

[32] Siqueira, R. M., Freitas, G. R., Peixoto, H. R., Do Nascimento, J. F., Musse, A. P. S., Torres, A. E., ... & Bastos-Neto, M. (2017). Carbon dioxide capture by pressure swing adsorption. Energy Procedia, 114, 2182-2192. https://doi.org/10.1016/j.egypro.2017.03.1355

[33] Baena-Moreno, F. M., Rodríguez-Galán, M., Vega, F., Vilches, L. F., Navarrete, B., & Zhang, Z. (2019). Biogas upgrading by cryogenic techniques. Environmental Chemistry Letters, 17(3), 1251-1261. https://doi.org/10.1007/s10311-019-00872-2

[34] Chen, X. Y., Vinh-Thang, H., Ramirez, A. A., Rodrigue, D., & Kaliaguine, S. (2015). Membrane gas separation technologies for biogas upgrading. Rsc Advances, 5(31), 24399-24448. https://doi.org/10.1039/C5RA00666J

[35] Yousef, A. M., El-Maghlany, W. M., Eldrainy, Y. A., & Attia, A. (2018). New approach for biogas purification using cryogenic separation and distillation process for CO2 capture. Energy, 156, 328-351. https://doi.org/10.1016/j.energy.2018.05.106

Energy, Environment and Storage

Journal Homepage: www.enenstrg.com

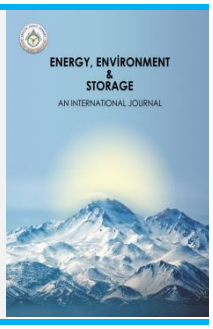

Solar-Powered Stirling Engines Integrated with HVAC Systems for Sustainable Building Applications: A Review

Zabihullah Bakhshi[1,2*], Mohammad Azim Rasuli [3]

[1]*Kabul University, Engineering Faculty, Mechanical Engineering Department, Kabul, Afghanistan.*

[2] *Erciyes University, Graduate School of Natural and Applied Science, Kayseri, Turkey.*

[3] *Okinawa Institute of science and Technology, Japan.*

Abstract. Globally, buildings consume nearly 40% of total energy, with heating, ventilation, and air conditioning (HVAC) systems contributing a significant share. As urbanization accelerates and energy insecurity intensifies, integrating renewable energy technologies into building systems has become essential for achieving sustainability, energy independence, and carbon neutrality. Among these technologies, Stirling engines coupled with concentrated solar thermal collectors demonstrate high efficiency, fuel flexibility, and the capacity for tri-generation, enabling the combined supply of electricity, heating, and cooling. This review synthesizes global research on solar-powered Stirling engines integrated with HVAC systems, emphasizing their relevance for sustainable building applications. The discussion covers four main domains: (i) solar-powered HVAC technologies for reducing building energy demand, (ii) Stirling engines in combined heat and power (CHP) and combined cooling, heating, and power (CCHP) applications, (iii) advances in modelling, simulation, and experimental development of dish/Stirling systems, and (iv) multi-energy applications and optimization strategies. Special attention is given to solar-rich yet underexplored regions such as Afghanistan, where high HVAC demand and frequent electricity shortages coincide with abundant solar potential. The review identifies research gaps, including the need for localized climate based studies, long term operational data, and system level integration strategies. Overall, findings suggest that Solar Stirling HVAC systems offer a viable pathway for sustainable buildings in high-solar regions, supporting both environmental goals and energy security.

Keywords: Solar energy, Stirling engine, HVAC systems, CFD Simulation.

Article History: 29, August 2025. Revised 22, September 2025. Accepted:29 September 2025; Availableonline: 30 September 2025
Doi: https://doi.org/10.52924/RVSR5576

1. INTRODUCTION

The building sector remains one of the most critical barriers to achieving global sustainability goals due to its high energy demand. Reports from the International Energy Agency (IEA) indicate that buildings account for nearly 40% of worldwide energy consumption and about one-third of greenhouse gas emissions (IEA) Within this sector, heating, ventilation, and air conditioning (HVAC) systems contribute significantly to energy use due to increasing urbanization, lifestyle changes, and the need for indoor comfort across varying climates. Reducing HVAC related energy consumption through renewable energy integration has therefore become a critical priority for both developed and developing countries.

In developing regions such as Afghanistan, the challenge is particularly acute. Kabul experiences extreme seasonal temperature variations with hot summers and cold winters resulting in substantial demand for both heating and cooling. At the same time, more than 70% of the country's electricity is imported from neighboring states such as Uzbekistan, Tajikistan, and Turkmenistan [1], yet the supply remains insufficient to meet demand. This reliance on imports makes Afghanistan highly vulnerable to disruptions and rising costs. In contrast, the country benefits from over 300 sunny days annually and high direct normal irradiance (DNI) levels [5], making it one of the most promising regions for solar energy exploitation in Central Asia. Harnessing this solar potential is essential to reduce dependency on imports, enhance energy independence, and support sustainable urban development. Stirling engines provide a promising route for integrating solar energy into building energy systems. Originally developed in the 19th century, Stirling engines are external combustion engines that convert heat into mechanical work with high theoretical efficiency, often exceeding that of internal combustion engines [6]. When coupled with parabolic dish collectors, Stirling engines can achieve solar-to-electric efficiencies of 25–32% [18],

* zabih.bakhshi56@mail.com

while their ability to operate in tri-generation mode allows simultaneous supply of electricity, heating, and cooling [7]. This makes them particularly suitable for HVAC applications in buildings. Compared to PV panels or internal combustion technologies, dish/Stirling systems typically deliver higher thermodynamic efficiency, require less maintenance, and produce no direct emissions [4,17].

In recent years, research on solar–Stirling–HVAC integration has expanded, covering areas such as system modeling, exergy analysis, design optimization, and hybrid configurations [9,12,19]. However, most studies have been conducted in Europe, the Middle East, or East Asia, with limited focus on Central and South Asia. For Afghanistan, despite its exceptional solar resources and urgent energy challenges, specific research remains scarce [1,5]. This review addresses this gap by synthesizing global advances in solar-powered Stirling engines and HVAC integration while highlighting their potential for Kabul's unique climatic conditions.

2. Solar-Powered HVAC Systems in Buildings

Heating, ventilation, and air conditioning (HVAC) systems are among the most energy-intensive components of buildings, often accounting for more than 50% of total energy consumption in hot–cold climates [2]. With urban loads climbing, coupling HVAC with solar resources is widely explored to reduce fossil fuel use, lower emissions, and improve building sustainability. Solar-assisted HVAC generally falls into three groups: (i) solar-thermal heating, (ii) solar-driven cooling, and (iii) combined heating/cooling hybrids [2,3].

2.1 Solar Heating Systems

Solar thermal energy has long been employed for domestic hot water (DHW) and space heating. In Afghanistan, Rahmany and Patmal [1] demonstrated that solar heating systems in Kabul can reduce greenhouse gas emissions while improving indoor comfort during winter. Fabrizio et al. [2] reviewed integrated solar thermal solutions for nearly zero-energy buildings (nZEB) in Europe, highlighting their role in meeting energy performance standards. These findings confirm that in regions with high solar irradiance, solar heating can substantially reduce reliance on fossil-based electricity.

2.2 Solar Cooling Systems

Cooling demand in buildings is rapidly increasing due to urban heat island effects and lifestyle changes. Solar driven cooling systems, particularly absorption and adsorption chillers, provide environmentally friendly alternatives to conventional vapor compression systems. Farzan [3], for example, conducted a TRNSYS based simulation of a solar powered absorption cooling system for an office building in Kerman, Iran. The results showed significant reductions in electricity consumption, demonstrating that solar cooling can effectively address peak electricity demand in sunny climates. Similarly, Allouhi et al. [4] emphasized that solar cooling is especially advantageous in regions where cooling demand coincides with peak solar availability.

2.3 Hybrid Solar Heating and Cooling Systems

Hybrid systems that combine solar heating and cooling allow year round utilization of solar energy. Karimi et al. [5] assessed solar heating and cooling strategies for Afghanistan and found that building orientation and passive design strongly influence efficiency. Fabrizio et al. [2] also highlighted that combining solar heating/cooling with optimized building envelopes is crucial for achieving nearly zero-energy performance.

2.4 Advantages and Limitations

The literature indicates that solar assisted HVAC systems can reduce building energy demand by 30–60%, depending on technology type (solar heating, solar cooling, or hybrid), location, and building design [2–5]. These systems also contribute to carbon mitigation and improved indoor comfort. However, challenges remain:

- Intermittency of solar resources limits system reliability without backup or storage,
- High initial investment costs hinder adoption in developing countries.
- System complexity requires advanced control strategies

2.5 Relevance for Afghanistan

Afghanistan presents strong opportunities for solar HVAC deployment because of high solar potential and seasonal demand for both heating and cooling. However, studies remain limited. The few available works [1,5] emphasize solar heating but lack detailed techno-economic assessments of year round HVAC integration. This underscores the need for simulation based studies that use high resolution hourly climate data to evaluate performance, reliability, and economic feasibility a gap directly addressed by the ongoing thesis research associated with this review.

3. Stirling Engines in CHP and CCHP Applications

The Stirling engine, invented in the early 19th century, is an external combustion engine operating on the Stirling thermodynamic cycle. Its ability to utilize diverse heat sources including biomass, natural gas, geothermal, and concentrated solar thermal energy makes it highly versatile for combined heat and power (CHP) and combined cooling, heating, and power (CCHP) applications. Compared to conventional internal combustion engines, Stirling engines offer several advantages, including high theoretical efficiency, low noise, long service life, and zero direct emissions when powered by renewable heat.

3.1 Stirling Engines in Combined Heat and Power (CHP)

Early applications of Stirling engines focused primarily on CHP, where waste heat is recovered for space or water heating. Moghadam et al. [6] developed an energy–exergy–economic (3E) methodology for optimal sizing of solar dish Stirling micro-CHP systems across different climates. Their results confirmed that Stirling-based CHP systems can achieve high overall efficiencies, especially in solar rich regions.

3.2 Stirling Engines in Combined Cooling, Heating, and Power (CCHP)

More recent research expanded to CCHP, where recovered thermal energy also drives absorption or adsorption chillers to provide cooling. Cheng and Huang [7] designed and simulated a Stirling-based tri-generation system that achieved an overall efficiency of 91%. Importantly, this figure refers to the combined utilization of electricity, heating, and cooling outputs, not just solar-to-electric efficiency. This distinction explains why system-level efficiency values are higher than the 25–32% solar-to-electric efficiencies typically reported for dish/Stirling systems [18].

3.3 Hybrid Stirling Systems

Hybridization strategies have been proposed to improve performance and reduce payback time. Sheykhi et al. [19] proposed a hybrid system combining a Stirling engine with an internal combustion engine, achieving a 12% increase in overall efficiency compared to stand-alone Stirling configurations. Such hybrid systems reduce economic risk by ensuring reliable operation during periods of low solar availability.

3.4 Advantages of Stirling Based CCHP Systems

Stirling engines present several advantages for CHP and CCHP:

- High efficiency across a wide range of operating temperatures.
- Fuel and heat-source flexibility (solar, biomass, hybrid).
- Scalability, from residential micro-CHP to district-scale tri-generation.
- Low maintenance and long service life due to external combustion.

They also provide important environmental benefits (see Sec. 5.3).

3.5 Limitations and Challenges

Despite these benefits, challenges hinder large-scale commercialization:

- High capital costs of solar concentrators and Stirling engines.
- Solar intermittency, requiring hybridization or storage solutions.
- Limited market penetration, as most studies remain at the simulation or pilot-project level.
- Ongoing technical challenges related to working fluid selection and regenerator optimization.

3.6 Relevance for Building Applications

For buildings, Stirling engines in CHP or CCHP systems can address simultaneous heating, cooling, and electricity demands (tri-generation). When integrated with HVAC, these engines serve as decentralized energy hubs, enhancing reliability and reducing dependence on imported electricity. For Afghanistan where grid supply is unreliable and HVAC loads are significant Stirling-based CCHP systems could transform building energy management when powered by the country's abundant solar thermal resources.

4. Solar Dish/Stirling Systems: Modelling, Simulation, and Experiments

Dish/Stirling systems are considered the most efficient solar thermal power technology, converting concentrated solar radiation into mechanical work via the Stirling engine. The modularity of dish/Stirling units makes them particularly suitable for decentralized building scale applications, where electricity, heating, and cooling can all be derived from a single solar collector.

4.1 Performance Characteristics

Hafez et al. [18] reviewed the state of dish/Stirling technology and reported solar-to-electric efficiencies of 25–32% under optimal conditions. These values are among the highest of any solar power conversion technology. However, overall performance depends strongly on solar irradiance, optical accuracy of the dish, and thermal losses at the receiver.

4.2 Simulation and Modelling Approaches

Numerical simulations are widely used to analyze and optimize dish/Stirling systems. Sandoval et al. [12] modeled a solar-powered Stirling engine using MATLAB/Simulink, demonstrating how regenerator effectiveness strongly influences thermal efficiency. Karimi et al. [5] carried out a techno-economic analysis of solar-powered HVAC systems in Afghanistan, showing that optimized collector orientation and insulation can reduce system costs while increasing output stability.

4.3 Experimental Studies

Experimental research has validated simulation results. For instance, Hossain et al. [17] tested a parabolic dish–Stirling prototype in Bangladesh and confirmed that thermal efficiency exceeded 30% under peak irradiance. In North Africa, Allouhi et al. [4] demonstrated that integrating dish/Stirling systems into hybrid micro-grids can reduce dependency on diesel by more than 40%.

4.4 System-Level Applications

Studies consistently report that solar-assisted HVAC systems integrated with dish/Stirling engines can reduce building energy demand by 30–60% [2–5]. As discussed in Sec. 2.4, these savings depend on the type of HVAC integration (heating only, cooling only, or hybrid) and on climatic conditions.

4.5 Relevance for Kabul, Afghanistan

Kabul presents favourable conditions for dish/Stirling deployment due to its high DNI (6–7 kWh/m²/day) and over 300 sunny days annually [5]. At the same time, the city's dual heating and cooling demand highlights the importance of year round system applicability. Simulation studies suggest that Stirling-based HVAC systems could substantially reduce import dependency, but localized performance validation is still lacking. Therefore, future work should focus on site-specific simulations using Kabul's climatic data to quantify seasonal reliability and cost-effectiveness.

5. Applications in Sustainable Buildings and Multi-Energy Systems

Stirling engines can be configured for diverse energy services beyond electricity generation. Their ability to harness waste heat makes them ideal for multi-energy applications, particularly in the context of sustainable buildings.

5.1 Combined Heat and Power (CHP) Applications

In CHP mode, Stirling engines generate electricity while simultaneously recovering waste heat for space heating or domestic hot water. Moghadam et al. [6] applied an energy–exergy–economic optimization approach to solar-powered micro-CHP systems and demonstrated that Stirling engines could provide competitive performance compared to conventional CHP technologies. Their findings suggest that Stirling-based CHP is especially attractive in climates with high winter heating demand.

5.2 Tri-Generation (Electricity, Heating, and Cooling)

CCHP, or tri-generation, extends the CHP concept by using waste heat to drive absorption or adsorption chillers, enabling cooling alongside heating and electricity. Cheng and Huang [7] reported a Stirling-based tri-generation system achieving an overall efficiency of 91%, when electricity, heating, and cooling were all utilized. This high system-level efficiency highlights the potential of tri-generation for buildings, although it is not directly comparable to the 25–32% solar-to-electric efficiency typically reported for dish/Stirling systems [18].

5.3 Environmental Benefits

The environmental benefits of Stirling-based multi-energy systems are substantial. When powered by solar heat, these systems operate with zero direct emissions, eliminating CO_2 , NO_x, and particulate matter. They also displace multiple fossil-based technologies, which reduces the overall carbon footprint of buildings. Studies in regions with high solar potential, such as North Africa and South Asia, report significant reductions in greenhouse gas emissions when dish/Stirling units are used in building applications [4,17]. These findings confirm that Stirling-HVAC integration supports net-zero energy building (nZEB) targets while improving urban air quality.

5.4 Economic Considerations

Economic analyses show that while Stirling engines have higher upfront costs than conventional HVAC and power systems, their multi-energy functionality improves cost effectiveness. For example, Sheykhi and Mehregan [9] demonstrated that hybrid Solar-Stirling systems reduce payback periods by ensuring continuous operation under variable solar conditions. Similarly, Karimi et al. [5] highlighted that system level design optimization in Afghanistan can significantly lower costs by maximizing year-round utilization.

5.5 Implications for Building Applications

For buildings, multi-energy Stirling systems offer unique advantages by addressing simultaneous demand for electricity, heating, and cooling. Their modular nature allows scaling from single family houses to district level applications. Importantly, as discussed in Sec. 5.3, their environmental benefits strengthen their role in sustainable building transitions. For Afghanistan, where both heating and cooling demands are significant, tri-generation systems present a particularly suitable pathway toward low carbon, resilient building energy solutions.

6. Hybridization and Optimization Strategies

To overcome the limitations of solar intermittency and high capital costs, researchers have explored hybridization and optimization strategies for Stirling-based energy systems. These strategies combine Stirling engines with other energy sources or apply advanced modeling methods to improve efficiency, cost-effectiveness, and reliability.

6.1 Hybrid Solar Fossil Configurations

Sheykhi et al. [19] proposed a hybrid system integrating a Stirling engine with an internal combustion engine, achieving a 12% increase in overall efficiency compared to stand alone Stirling engines. The hybrid approach ensures continuous operation during cloudy periods or at night, while also reducing the economic risks associated with solar only systems. Although fossil fuel backup reduces the environmental benefits, hybridization remains an important transitional pathway in regions with unreliable solar availability.

6.2 Hybrid Solar Storage Systems

Energy storage integration is another important strategy. Hossain et al. [17] demonstrated that thermal storage combined with dish/Stirling engines can significantly smooth output fluctuations, thereby improving system stability. Similarly, Allouhi et al. [4] highlighted that hybridization with storage in North Africa reduced reliance on diesel by more than 40%, while maintaining high reliability.

6.3 Multi-Objective Optimization

Multi-objective optimization methods have been widely applied to Stirling systems. Sheykhi and Mehregan [9] developed a multi-criteria framework that optimized system performance by balancing energy efficiency, exergy losses, and economic payback. Their results indicated that system level trade-offs, rather than single parameter optimization, provide more realistic pathways for deployment.

6.4 Relevance to Kabul, Afghanistan

For Kabul, hybridization and optimization are particularly relevant. On one hand, hybrid Stirling fossil systems can guarantee reliability during winter or prolonged cloudy periods. On the other hand, hybrid Stirling storage configurations are more aligned with Afghanistan's long term sustainability goals. The 12% efficiency gain from hybrid solar fossil systems [19] must therefore be viewed as transitional, while future designs should prioritize renewable only or storage supported systems. Optimization frameworks similar to those presented by Sheykhi and Mehregan [9] could be adapted to Kabul's climate to identify cost-effective and reliable system configurations.

Table 2: Solar potential and Stirling system performance (Afghanistan and other regions)

Region	Key References	Solar Potential (DNI)	Reported Efficiency	Environmental/Economic Findings
Afghanistan	Rahmany & Patmal (2021); Karimi et al. (2024)	6–7 kWh/m²/day DNI; >300 sunny days	30–60% HVAC demand reduction	CO_2 reduction, reduced import dependency
Morocco	Allouhi et al. (2022)	5–6 kWh/m²/day DNI	25–30% electric efficiency	4E analysis shows strong sustainability
Bangladesh	Hossain et al. (2023)	4.5–5 kWh/m²/day DNI	24–28% electric efficiency	Prototype successful for off-grid
Brazil	Sandoval et al. (2019)	5–5.5 kWh/m²/day DNI	≈25% electric efficiency	Validated in Natal (case study)

7. Research Gaps

Despite extensive global research, several critical gaps remain in the study of solar-powered Stirling engines integrated with HVAC systems. Addressing these gaps is necessary for wider adoption, especially in developing countries such as Afghanistan.

7.1 Limited Long Term Operational Data

Most existing studies are based on simulations or small scale prototypes [6,12,17]. Long term operational data on reliability, maintenance, and seasonal performance are scarce, making it difficult to validate models or predict lifecycle performance. Pilot projects in diverse climates, including Central and South Asia, are urgently needed.

7.2 Inconsistent Metrics and Comparisons

Reported performance metrics vary widely. For instance, tri-generation systems often cite overall efficiency above 90% [7], while dish/Stirling systems typically report solar-to-electric efficiencies of 25–32% [18]. Hybrid systems report additional gains of 10–15% [19]. Without clear distinctions, these numbers appear contradictory. Future work must standardize metrics (electric efficiency, thermal efficiency, overall utilization) to ensure fair comparisons.

7.3 Lack of Climate-Specific Studies for Afghanistan

Afghanistan receives over 300 sunny days per year, with direct normal irradiance (DNI) averaging 6–7 kWh/m²/day [5]. Yet, only a handful of studies [1,5] have explored solar heating, and virtually none have modelled Stirling-based tri-generation for year-round HVAC. Kabul's dual heating and cooling demands make it an ideal case for such studies, but simulation-based evaluations using high resolution hourly climate data are missing.

7.4 Economic and Policy Dimensions

The economics of Stirling-HVAC integration remain underexplored in Afghanistan. Regional studies in Iran and Morocco suggest that the levelized cost of electricity (LCOE) for dish/Stirling systems ranges from 0.10–0.15 USD/kWh [4,17]. Although this is higher than Afghanistan's subsidized electricity imports, it becomes competitive when considering (i) the added value of on-site heating and cooling, (ii) reduced dependence on imported electricity (currently >70% [1]), and (iii) avoidance of diesel backup during outages. Future research should therefore combine energy–exergy modelling with techno-economic and policy analysis to quantify these trade-offs.

7.5 Integration with Storage and Hybrid Systems

Hybridization with fossil backup offers transitional reliability [19], but future systems for Afghanistan should prioritize renewable based hybrids (dish/Stirling + storage). Optimization methods such as those proposed by Sheykhi and Mehregan [9] could be adapted to Kabul's context, balancing energy efficiency, exergy performance, cost, and reliability.

8. Conclusion

This review synthesized global advances in solar-powered Stirling engines integrated with HVAC systems, with a focus on their potential role in sustainable building applications. Four main themes were covered: (1) solar-assisted HVAC technologies, (2) Stirling engines in CHP and CCHP systems, (3) modeling, simulation, and experimental developments of dish/Stirling units, and (4) hybridization and optimization strategies. Collectively, these studies highlight the technical promise of Stirling-based multi-energy systems in reducing building energy demand, mitigating emissions, and enhancing energy resilience.

For Afghanistan, where electricity imports account for more than 70% of supply [1] and HVAC loads dominate building demand, Stirling–HVAC integration presents a particularly relevant pathway. With more than 300 sunny days annually and high direct normal irradiance [5], Kabul and other Afghan cities represent prime locations for deploying such systems. However, localized studies remain limited, especially regarding techno-economic feasibility, seasonal reliability, and integration with storage.

The key contribution of this review lies in consolidating global findings, clarifying performance differences across system configurations, and contextualizing them for Afghanistan's unique climatic and infrastructural conditions. Rather than reporting new simulation or exergy analyses, this work identifies priority research gaps and directions for future studies. These include conducting detailed exergy and 4E analyses, developing simulation-based optimization frameworks, testing hybridization strategies (solar + storage), and linking technical results with policy and planning considerations.

Table 2: Summary of the reviewed studies.

Author/Year	System Type	Region	Method	Efficiency	Environmental/Economic Findings
Rahmany & Patmal (2021)	Solar heating for buildings	Afghanistan	Case study/Simulation	30–40% GHG reduction	CO_2 savings in Kabul
Fabrizio et al. (2014)	Integrated HVAC & DHW	Italy	Review/Simulation	20–30% energy saving	Supports NZEB goals
Farzan (2022)	Solar-powered absorption cooling	Iran	Simulation (TRNSYS)	COP ≈ 0.7–0.8	Feasible for office buildings
Allouhi et al. (2022)	Dish Stirling 4E analysis	Morocco	Simulation	25–30% elec. eff.	Reduced CO_2 emissions
Karimi et al. (2024)	Solar-assisted HVAC in Afghanistan	Afghanistan	Simulation	30–60% load reduction	Techno-economic potential
Moghadam et al. (2013)	Dish Stirling micro-CHP	Iran	Simulation	26–31% elec. eff.	Economic viability in some climates
Cheng & Huang (2021)	Stirling tri-generation	Taiwan	Simulation/Prototype	91% overall eff.	Multi-energy supply
Sheykhi & Mehregan (2024)	CCHP α-Stirling	Iran	Simulation	12–15% efficiency gain	Economic improvement
Hafez et al. (2016)	Parabolic dish Stirling design	Egypt	Simulation/Design	27–29% eff.	Thermal analysis
Sandoval et al. (2019)	Dish Stirling in Brazil	Brazil	Simulation	≈25% elec. eff.	Case study (Natal)
Hossain et al. (2023)	Dish Stirling prototype	Bangladesh	Experimental	24–28% elec. eff.	Good for off-grid
Chahartaghi & Sheykhi (2019)	CCHP with Stirling	Iran	Simulation	35–40% overall eff.	CO_2 reduction shown
Jabari et al. (2020)	Dish Stirling + desalination	Iran	Simulation	≈22–25% eff.	Water + power cogeneration
Shazly et al. (2014)	MATLAB Stirling design	Egypt	Simulation/Design	27% elec. eff.	System thermal modeling
Guarino et al. (2021)	Dish Stirling for tertiary sector	Italy	Simulation	≈25% eff.	Energy-saving potential
Gholamalizadeh & Chung (2017)	Collector design for dish-Stirling	Korea	Design study	-	Optimization of collector
Barreto & Canhoto (2016)	Dish Stirling modeling	Portugal	Simulation	≈28% eff.	Dish/Stirling feasibility
Castellanos et al. (2019)	Dish Stirling grid-connected	Brazil	Experimental	≈26% eff.	Grid integration validated
Sheykhi et al. (2025)	Hybrid ICE–Stirling CCHP	Iran	Simulation	≈12% hybrid gain	Improved system flexibility
Dang & Zhao (2016)	Stirling cryocooler	China	Experiment/CFD	Low-T COP improvement	Cryogenic extension of Stirling
Almajri et al. (2017)	Alpha-type Stirling CFD	UK	Simulation	-	Engine design insights
Zayed et al. (2021)	Dish Stirling parametric analysis	China	Simulation	≈25% eff.	Performance optimization

By bridging global research with Afghanistan's energy challenges, this review provides a foundation for future applied studies and contributes to the broader discussion on sustainable, resilient, and low-carbon building energy systems in solar-rich developing countries.

9. REFERENCES

[1] Rahmany, N. A., & Patmal, M. H. (2021). Impact of solar heating technology installation on reduction of greenhouse gas emissions in

Kabul city. International Journal of Innovative Research and Scientific Studies, 4(2), 70–79.

[2] Fabrizio, E., Seguro, F., & Filippi, M. (2014). Integrated HVAC and DHW production systems for Zero Energy Buildings. Renewable and Sustainable Energy Reviews, 40, 515–541.

[3] Farzan, H. (2022). Dynamic simulation of solar-powered heating and cooling system for an office building using TRNSYS: A case study in Kerman. Journal of Renewable Energy and Environment, 9(2), 27–36.

[4] Allouhi, H., Benzakour Amine, M., Saadani, R., Kousksou, T., Jamil, A., Rahmoune, M., Saidur, R., & Zafar, S. (2022). Solar Dish Stirling technology for sustainable power generation in Southern Morocco: 4-E analysis. Sustainable Energy Technologies and Assessments, 52, Article 102065.

[5] Karimi, M., Chikamoto, T., Lee, M., & Tanaka, T. (2024). Impact of Building Orientation on Energy Performance of Residential Buildings in Various Cities Across Afghanistan. Sustainability, 16(24), 11076.

[6] Moghadam, R. S., Sayyaadi, H., & Hosseinzade, H. (2013). Sizing a solar dish Stirling micro-CHP system for residential application in diverse climatic conditions based on 3E analysis. Energy Conversion and Management, 75, 348–365.

[7] Cheng, C.-H., & Huang, J.-S. (2021). Development of tri-generation system combining Stirling cooler and Stirling engine. International Journal of Energy Research, 45(15), 21006–21022.

[8] Chahartaghi, M., & Sheykhi, M. (2019). Energy, environmental and economic evaluations of a CCHP system driven by Stirling engine with helium and hydrogen as working gases. Energy, 174, 1251–1266.

[9] Sheykhi, M., & Mehregan, M. (2024). Comprehensive technical and economic study and optimization of a novel combined cooling heating and power system driven by a four cylinder α type Stirling engine. Applied Thermal Engineering, 236, 121869.

[10] Sheykhi, M., Mehregan, M., & Zhu, S. (2025). Simulation and performance optimization of a novel hybrid CCHP system based on the prime movers of internal combustion engine and Stirling engine. Applied Energy, 393, Article 126103.

[11] Shazly, J. H., Hafez, A. Z., El Shenawy, E. T., & Eteiba, M. B. (2014). Simulation, design and thermal analysis of a solar Stirling engine using MATLAB. Energy Conversion and Management, 79, 626–639.

[12] Sandoval, O. R., Vargas, J. V. C., & Ordonez, J. C. (2019). Modelling, simulation and thermal analysis of a solar dish/Stirling system: A case study in Natal, Brazil. Energy Conversion and Management, 181, 189–201.

[13] Castellanos, L. S. M, Noguera, A. L. G, Caballero, G. E. C, De Souza, A. L, Cobas, V. R. M, Lora, E. E. S, Venturini, O. J. (2019). Experimental analysis and numerical validation of the solar Dish/Stirling system connected to the electric grid. Renewable Energy.135, 259-265

[14] Gholamalizadeh, E., & Chung, J. D. (2017). Design of the Collector of a Solar Dish-Stirling System: A Case Study. IEEE Access, Article 2758354.

[15] Barreto, G., & Canhoto, P. (2016). Modelling of a Stirling engine with parabolic dish for thermal to electric conversion of solar energy. Energy Conversion and Management.

[16] Zayed, M. E., Zhao, J., Elsheikh, A. H., Zhao, Z., Zhong, S., & Kabeel, A. E. (2021). Comprehensive parametric analysis, design and performance assessment of a solar dish/Stirling system. Process Safety and Environmental Protection, 146, 276–291.

[17] Hossain, M. S., Rahat, M. A. I., Khan, M. S. H., Salehin, S., & Karim, M. R. (2023). Solar-driven Dish Stirling System for sustainable power generation in Bangladesh: A case study in Cox's Bazar. Heliyon, 9(e14322).

[18] Jabari, F., Nazari-heris, M., Mohammadi-ivatloo, B., Asadi, S., & Abapour, M. (2020). A solar dish Stirling engine combined humidification-dehumidification desalination cycle for cleaner production of cool, pure water, and power in hot and humid regions. Sustainable Energy Technologies and Assessments, 37, 100642.

[19] Guarino, S., Catrini, P., Buscemi, A., Lo Brano, V., & Piacentino, A. (2021). Assessing the Energy-Saving Potential of a Dish-Stirling Con-Centrator Integrated into Energy Plants in the Tertiary Sector. Energies, 14(1163).

[20] Almajri, A. K., Mahmoud, S., & Al-Dadah, R. (2017). Modelling and parametric study of an efficient Alpha type Stirling engine performance based on 3D CFD analysis. Energy Conversion and Management, 145, 93–106.

[21] Dang, H., & Zhao, Y. (2016). CFD modeling and experimental verification of a single-stage coaxial Stirling-type pulse tube cryocooler without either double-inlet or multi-bypass operating at 30–35 K using mixed stainless steel mesh regenerator matrices. Cryogenics, 78, 40–50.

[22] Hafez, A. Z., Soliman, A., El-Metwally, K., & El-Dafrawy, M. A. (2016). Solar parabolic dish Stirling engine system design, simulation, and thermal analysis. Energy Conversion and Management, 126, 60–75.

Energy, Environment and Storage

Journal Homepage: www.enenstrg.com

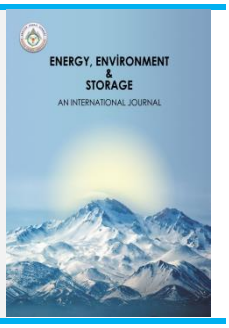

Olive Seed Based Biodiesel Production Process and Investigation of Combustion Properties of Fuel Blends With Standard Diesel And TiO_2 and Activated Carbon Nanoparticle Additives in Diesel Engines

Selman Taşdemir[1], Volkan Sabri Kül[2*], Mehmet Saritaş[3], Serhat Bilgin[4]

[1] *Erciyes University Department of Mechanical Engineering, Kayseri, Türkiye, ORCID: 0009-0008-5704-5679*

[2*] *Erciyes University, Graduate School of Natural and Applied Sciences, ORCID: 0000-0002-6412-6062*

[3] *Erciyes University, Department of Mechanical Engineering, Kayseri, Türkiye ORCID: 0000-0001-6576-689X*

[4] *Tokat Gaziosmanpasa University: Tokat, Türkiye ORCID: 0000-0002-6812-6641*

ABSTRACT. In this study, the production stages of biodiesel from olive stones and the equipment used in the production process are introduced. Furthermore, the engine performance and exhaust emissions of biodiesel blends obtained from olive stones (B20D80) and its nanoparticle-added derivatives in diesel engines were evaluated. Using test data provided by the PCS engine test system, experiments were conducted with pure diesel (D100), olive stones (BOS20D80), and various additives containing 50 ppm TiO_2 and 50 ppm activated carbon + 50 ppm TiO_2 . The experiments revealed improvements in the thermal efficiency of the nanoparticle-added pure diesel and BOS20D80 fuels, while relatively higher NO emissions were observed.

Keywords: *olive seeds, biodiesel, diesel engine, TiO_2 , activated carbon, nanoparticles.*

Article History: Received: 30 August 2025; Revised: 24 September 2025; Accepted:29 September 2025; Availableonline: 30 September 2025
Doi: https://doi.org/10.52924/QZPQ2586

1. INTRODUCTION

The ever-increasing demand for energy, the risk of depletion, and the environmental damage caused by fossil fuel resources have made it necessary to turn to alternative energy sources. Today, a large portion of global energy needs are met through fossil fuels, leading to serious problems in terms of environmental pollution, greenhouse gas emissions, and energy security. Furthermore, the limited reserves of these resources directly impact energy costs and increase foreign dependency in national economies.

In this context, biofuels are considered a significant alternative due to their sustainability, renewable nature, and low environmental impact. Biofuels can be obtained from vegetable or animal oils, agricultural waste, and other organic materials. Their compatibility with diesel engines, in particular, makes them suitable for use without requiring additional modifications to engine technology, making them even more attractive.

There are many studies in the literature regarding additives mixed into diesel fuel [1-20]. Sel, 2013 [4] investigated the effects of blending biodiesel and Eurodiesel fuels at different ratios on engine performance and exhaust emissions. As the biodiesel ratio increased, a decrease in engine power and an increase in specific fuel consumption were observed. Additionally, an increase in NOx emissions and a decrease in CO, HC, and soot emissions were observed. In the second stage, nano-hydro borazine additive was added to the fuel blends, and it was reported that this new fuel increased its viscosity but improved engine performance and reduced specific fuel consumption. However, an increase in CO_2 and NOx and a decrease in CO and soot emissions were observed. Hacıkadiroğlu, 2007 [5] tested blends of 100% diesel (D100), 90% diesel - 10% biodiesel (B10), 80% diesel - 20% biodiesel (B20), and 50% diesel - 50% biodiesel (B50) in a four-stroke, air-cooled, single-cylinder diesel engine. Engine speed, internal pressure, exhaust temperature, and emission values were systematically measured, and the consumption time of a specific volume of fuel was calculated. Experimental data revealed that biodiesel addition positively affects emission parameters. Kumar and Kaya, 2006 [6] produced biodiesel from crude and waste vegetable oils using the transesterification method, determining the optimum temperature, appropriate reactants, and purification methods to achieve high-quality biodiesel production. Basic physical properties of the resulting biodiesels, such as viscosity, density, cetane number, and flash point, were characterized. Raheman et al. (2022) [19] stated that the use of cerium oxide solid particulate additives in 20% biodiesel

*volkanskul@gmail.com

blended diesel fuel increased BTE by 7-13.3% compared to pure diesel fuel. Brake specific energy consumption decreased by 6.7-11.7%. Reductions in HC, CO and NOx emissions were reported by 19.4-55.6%, 6.5-52.8% and 23.2-41.5%, respectively. Vellaiyan et al. (2019) [20] used 100 ppm Titanium oxide (TiO2) solid particulate additive in diesel fuel with the addition of 10% water. They reported reductions in NOx, HC, CO and soot emissions by 21%, 40.1%, 21%, 40.1% and 10.7%, respectively, compared to fuel without TiO2 additive. Örs, 2016 [7] investigated the performance and emission effects of biodiesel-butanol blends on a direct-injection diesel engine. Butanol ratios of 5%, 10%, and 15% were used in blends. With 15% butanol addition, significant reductions in NOx and CO emissions were achieved, but an increase in HC emissions was observed. An approximately 10% improvement in specific fuel consumption was also reported. Aydoğan, 2008 [9] produced biodiesel at a laboratory scale using oils from various sources and tested them under different engine speeds and full-load conditions by blending them with diesel in specific ratios. Engine performance was also evaluated, along with NOx, CO, SO_2 , and soot emissions. Research was also conducted on methods for reducing NOx emissions in compression-ignition engines. Nişancı, 2007 [9] conducted engine tests by blending biodiesels obtained from different plants (soybean, sunflower, and canola) at various ratios. The mixtures were tested in direct-injection diesel engines, and emissions and performance parameters were analyzed. Kaya, 2010 [10] investigated the effect of injection pressure on engine performance using biodiesel-diesel fuel blends. In experiments conducted with canola-derived biodiesel, CO_2 and NOx increased as the biodiesel ratio increased, while CO, HC, and soot emissions decreased. Specific fuel consumption increased and efficiency decreased at different injection pressures. Ilgazlı, 2010 [11] evaluated the effects of different biodiesel ratios (B20, B50, and B100) on engine performance and emissions in a four-stroke diesel engine with variable compression ratios. During the experiments, engine power, emissions data, and in-cylinder pressure changes were measured. Peker, 2009 [12] produced biodiesel from non-food grade waste olive oil and obtained a product with 97.6% ester content. The density of the product was measured as 878.6 kg/m³, viscosity as 4.82 mm²/s, flash point as 122°C, and water content as 156 mg/kg.

This study aims to produce biofuels from olive seeds, a widely produced resource in Turkey and a high potential waste stream. Olive seeds are a lignocellulosic agricultural waste with a high energy content. This characteristic makes it both an economically valuable biomass source and, if left unused, creates environmental waste. In the study, olive stones were dried, ground into powder, and then oil was obtained through solvent extraction. Acetone was used as the solvent in the extraction process, and parameters such as temperature and time were controlled throughout the experimental process.

The resulting biofuel was subjected to performance tests on a diesel engine test system in the university's engine test laboratory. The tests were conducted under constant torque and speed conditions, and comparatively evaluated not only olive stone biofuel but also safflower oil, waste oil, their 20% blends, and versions containing 50% titanium dioxide and activated carbon. During the tests, parameters such as engine oil temperature, exhaust temperature, inlet and outlet water temperatures, intake air temperature, and fuel temperature were recorded, and performance analyses were conducted for each fuel type.

The environmental impacts of fossil fuel use have highlighted biofuel alternatives for diesel engines. Biodiesels (especially from non-food sources) reduce CO/HC/smoke in most studies, but exhibit complex effects on BTE/BSFC and NOx due to calorific value and fluidity. Metal oxide nanoparticle additives (AlO_3 , TiO_2 , etc.) can reduce BSFC and CO/HC by improving atomization and combustion through oxygen transport and catalytic oxidation in the fuel; however, NOx generally tends to increase [1-3]. This study evaluates olive stone-derived B20 blends (B20D80) and its field-derived TiO_2 /activated carbon-added derivatives against a D100 reference using real-world engine test data.

These comprehensive analyses evaluated the technical applicability, combustion efficiency, and thermal behavior of olive stone-based biofuel in diesel engines. In addition, in the light of the data obtained, the potential of biofuels as an alternative to traditional fossil fuels was examined and their contribution to environmental sustainability was discussed.

2. MATERIALS AND METHODS

2.1 Test Fuels

2.1.1 Diesel

The diesel fuel used in the experiments was commercially available diesel. It was obtained from a local gas station, and its characteristics are presented in **Table 1**.

Table 1. Diesel [13]

Properties	Diesel
Density	820-845 kg/m3
Stoichiometric ratio	14,92 (app.)
Flash point	55 °C
ignition Temperature	Auto-186–230 °C
Higher Heating Value	45.6 MJ/kg
Low heat Value	42.7 MJ/kg
Cetane Number	51
Viscosity	2.0- 4.5 mm^2 /s

2.1.2 Biodiesel

I. General properties of biodiesel and Standards

To determine the suitability of the produced biodiesel as a fuel, its compliance with the European Union's TS EN 14214 standard and the American ASTM D6751 standard must be assessed. These standards define the fundamental physical and chemical properties of biodiesel that directly affect engine performance, safety, and environmental impacts. The literature reports that the vast majority of biodiesel samples derived from olive stones meet the limit values set by these standards for key parameters such as density, viscosity, flash point, cetane number, acid value, and ester content. This suggests that olive stone-based biodiesel could be a suitable and sustainable alternative fuel for diesel engines.

Table 2. General properties of biodiesel obtained from olive seeds

Properties	Typical Value Range
Density (15°C)	860–880 kg/m³ [13]
Viscosity (40°C)	4,2–5,0 mm²/s [6, 9]
Cetane Number	51–56 [14]
Flash Point	120–130 °C [4]
Cloud Point	-2 ila 0 °C [13]
Pour Point	-15 ila -18 °C
Heating value	39.96 Mj/kg [15]

II. Biodiesel production equipment and production stages from olive seeds

Olive Stone

In this study, olive stones, agricultural waste obtained from the olive processing industry, were used as the primary raw material. The stones, procured from local producers, were air-dried under ambient conditions and then dried in a constant-temperature industrial oven to reduce moisture content. This brought the stones into a physical form and low moisture content suitable for pyrolysis, solvent extraction, and transesterification processes.

Fig.1 Olive Seeds

Drying Process

The olive pits were first pretreated using a natural shade drying method, then dried in a constant-temperature industrial oven at 105°C for approximately 24 hours. This process reduced the moisture content of the biomass to below 10%, eliminating moisture that could reduce reaction efficiency in subsequent chemical processes (especially solvent extraction and pyrolysis).

Raw Material Preparation

The dried stones were homogenized using grinders to a particle size of approximately 1–2 mm. This process was performed to increase both solvent extraction efficiency and pyrolysis reaction efficiency by increasing surface area. The resulting powdered samples were stored in airtight containers at room temperature before starting the reactions.

Methanol (CH_3 OH)

High-purity methanol (99%) was chosen as the alcohol component in the transesterification reaction. Methanol served as the primary reactant, enabling the conversion of triglyceride-like fats to methyl esters. Methanol's short-chain, polar structure facilitates the high efficiency of the reaction and facilitates the separation of the methyl ester and glycerin phases.

Sodium Hydroxide (NaOH)

Sodium hydroxide (NaOH), used as a base catalyst to form sodium methoxide solution, played an active role in initiating the transesterification reaction. A homogeneous catalyst solution was prepared by mixing it with high-purity methanol at a predetermined ratio before the reaction. The use of this solution accelerates the conversion of oil to methyl ester and helps maintain chemical stability in the reaction medium. Furthermore, NaOH contributed to maintaining chemical stability in the solution throughout the reaction, increased esterification efficiency, and facilitated the effective separation of the glycerin and biodiesel phases. NaOH, preferred due to its low cost, widespread availability, and high catalytic activity, was used as the base catalyst in biodiesel production in this study in accordance with standards.

Acetone (CH_3 $COCH_3$)

In the post-transesterification product purification phase, acetone was used as a solvent to remove methanol, soap residues, and other byproducts remaining in the reaction mixture. Acetone's low boiling point (56°C) allowed for rapid and energy-efficient evaporation. This facilitated easy separation of the solvent from the biodiesel phase, increased fuel purity, and resulted in a product more compliant with TS EN 14214. Evaporation and separation were carried out using a laboratory-grade HAHN SHIN HS-2005V-N vacuum evaporator. This device enabled controlled solvent removal and prevented degradation of the biodiesel composition. Consequently, this step plays a critical role in improving the fuel properties of biodiesel and reducing negative emissions that may occur during combustion.

Density Measuring Device – Krüss Optronic (Germany)

This device was used to determine the density values of biodiesel samples with high precision. This measurement provided a detailed characterization of the fuel's physical properties and played a critical role in assessing its compliance with international fuel standards such as TS EN 14214 and ASTM D6751. Density is one of the key parameters affecting the combustion characteristics, spray behavior, and energy content of biodiesel. Therefore, density measurement is an important assessment step in the quality control process of the resulting biofuel.

Fig. 2 Density Measuring Device – Krüss Optronic (Germany)

The Cloud and Pour Point Device – Normalab NTE-450

was used to determine the low-temperature performance of produced biodiesel samples. Measurements using this device determined the cloud point (Cloud Point) and pour point (Pour Point) temperatures of biodiesel. These two parameters determine the fuel's ability to maintain fluidity at low temperatures and are critical in preventing problems such as freezing, clogging, and interrupted fuel flow in engine systems, especially in winter conditions. The obtained values contributed to the evaluation of biodiesel's suitability for use in cold climates.

Fig. 3 Normalab NTE-450

The Cold Filter Plugging Point Device – Normalab NTL-450

was used to determine the permeability of a biodiesel sample through the filter surface at low temperatures. This test evaluated whether the fuel could flow into the engine system without clogging the filters in cold weather conditions. The CFPP value is a key parameter that directly affects the fuel's fluidity limit and system safety in diesel engines, especially during winter. The test results were considered a key criterion in evaluating the performance of biodiesel for its usability in cold climates.

Fig. 4 Normalab NTL-450

Fuel-Acetone Separator – HAHN SHIN HS-2005V-N

After transesterification and subsequent solvent purification, evaporation was used to remove residual acetone from the biofuel mixture. This process effectively separated the volatile solvent phase from the biofuel, resulting in a biodiesel with higher purity and stable components. The evaporation process is based on the principle of removing acetone, which has a low boiling point, from the environment under controlled temperatures. The resulting fuel, obtained through this method, better complies with TS EN 14214 and ASTM D6751 standards in terms of both chemical purity and performance.

Fig. 5 Fuel-Acetone Separator

Heated Magnetic Stirrer – DLAB MS-H340-S4

A heated magnetic stirrer was used during the transesterification process to maintain a constant temperature and achieve a homogeneous solution. This device facilitated both thermal equilibrium of the reaction medium and effective mixing of the chemical components, contributing to the controlled and efficient reaction. Continuous stirring prevented phase separation and optimized methyl ester formation.

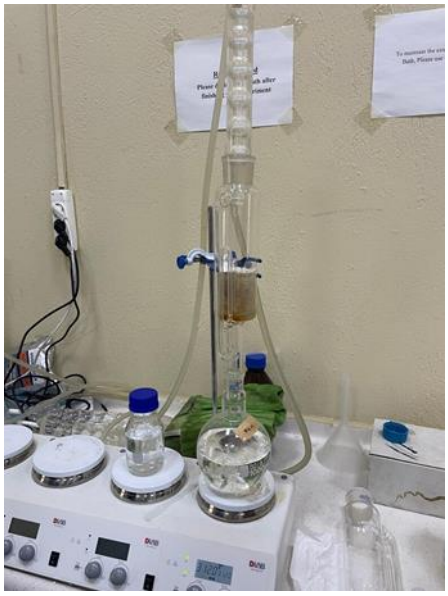

Fig. 6 Heated Magnetic Stirrer – DLAB MS-H340-S4

Mechanical Stirrer – JSR Brand

A heated magnetic stirrer was used effectively to homogenize highly viscous reaction mixtures. The device maintained the integrity and stability of the reaction solution by ensuring a continuous and even distribution of the components within the solution. This increased transesterification efficiency and positively impacted product quality.

Fig. 7 Mechanical Stirrer

Industrial Oven

Pre-drying of olive pits was carried out in a laboratory-type controlled-temperature oven. The oven operated at a temperature between 105–110°C to remove free and bound moisture from the pits. This drying process was considered a critical preparatory step in the oil extraction process because it directly impacts the efficiency of the pyrolysis process.

Fig. 8 Industrial Oven

Cooling Device – Thomson PMT TLC60

A cooling bath was used for samples requiring rapid cooling following the reaction process, particularly during the precipitation of the biodiesel phase and the separation of solvents. By providing a temperature-controlled environment, the device supported post-reaction product stabilization and increased the efficiency of phase separation.

Fig. 9 Cooling Device – Thomson PMT TLC60

III. Biodiesel production Stages

Drying of Olive Stones

The olive stones used as raw materials in this study were first stored in natural conditions to reduce free moisture content. Then, they were dried in an industrial oven at 105°C for 24 hours. This pre-drying process was performed to increase reaction efficiency in both the pyrolysis and solvent extraction oil extraction stages and to prevent the formation of undesirable byproducts.

Grinding and Cartridge Filling Process

Once the dried olive stones were processed in a suitable mechanical grinder to break them into small pieces to make them more digestible. The resulting ground stones were placed in specially designed cartridges, prepared for solvent extraction. These cartridges were designed to ensure effective solvent contact and maximize oil solubility. The cartridge design is shown in **Figure 10**.

Fig.10 Cartridge Filling

Oil Extraction with Acetone in a Reflux System

The prepared cartridges were placed in a laboratory-type reflux system for the oil extraction process. Acetone (CH_3 $COCH_3$) was added to the cartridges as a solvent, and the system was positioned on a DLAB brand magnetic stirrer heater. The reflux process was initiated, allowing the solvent to continuously evaporate and condense, bringing it into contact with the raw material. After approximately 6–7 cycles, the majority of the oils in the olive pits were converted into acetone. This process was repeated multiple times, resulting in a total volume of 1 liter of acetone-oil mixture. The applied extraction system is shown in **Figure 11.**

Fig.11 Reflux System

Separation of Acetone from Oil

The acetone-oil mixture obtained through the reflux process was transferred to a HAHN SHIN HS-2005V-N model separation device for solvent removal. Acetone's low boiling point (56°C) was utilized to remove it by evaporation. Thus, the solvent phase was completely removed, yielding approximately 1 liter of pure olive kernel oil. The purification process is presented in **Figure 5**.

Transesterification Reaction

Methanol (250 mL) at a volumetric ratio of 25% by volume and sodium hydroxide (NaOH) at a weight of 1% by weight of the oil were added to purified olive kernel oil. This mixture was stirred for 1 hour at 60°C using a JSR brand mechanical stirrer and a DLAB MS-H340-S4 model magnetic stirrer with heating. The transesterification process resulted in the formation of two distinct phases—biodiesel (upper phase) and glycerin (lower phase). This process is shown in **Figure 7**.

Precipitation Process

Following the transesterification process, the resulting mixture was left at room temperature for 72 hours (3 days) to allow phase separation to occur naturally. During this time, due to the density difference, glycerin accumulated in the lower phase and biodiesel in the upper phase. The glycerin collected in the lower phase was carefully removed, leaving only the upper biodiesel phase ready for purification.

Fig.12 Sedimentation Process (in the separatory funnel)

Washing Biodiesel with Pure Water

The biodiesel obtained after transesterification was washed with pure water to remove any remaining soap, methanol, and other residue. The washing process was carried out by adding an equal volume of pure water to the biodiesel phase, and the mixture was gently agitated to achieve homogeneity. Then, due to the density difference, the water layer that accumulated in the lower phase was carefully removed. This process was repeated multiple times to minimize impurities in the biodiesel and improve the fuel's usability.

Fig.13 Washing Biodiesel with Pure Water

In the present study, the workflow schematically shown in Figure A was followed. A six-cylinder compression ignition engine was used in the experiments. 50 mg and 100 mg TiO2 were added for every 1000 g of diesel fuel. Titanium dioxide (TiO2) with a particle size of 21 nm was used as nanoparticle. The mixtures were mixed with a mechanical stirrer at 1000 RPM for one hour. The fuels were coded as D for diesel, D_50ppm + 50 ppm TiO2 for diesel, and D_100ppm + 100 ppm TiO2 for diesel. Neodymium magnets were placed around the diesel fuel line to create a magnetic field of 1 tesla. In the experiments conducted with a magnetic field, the label "Magnetic" was added to the fuel codes to indicate the type of experiment. These three fuel types were tested in a compression ignition engine with and without a magnetic field. The experimental results are discussed in Section 3. A balance with a sensitivity of 0.5 g was used for fuel consumption measurement. Exhaust emissions were measured using a Bosch BEA 60 analyzer. Recording of engine performance data was facilitated by the PCS engine performance measurement system.

2.1.3 Nanoparticles

TiO_2 and activated carbon were used as nanoparticles in the experiments. Their properties are given in **Table 3 and 4**.

Table 3. TiO_2 specifications

Properties	TiO_2	Activated Carbon
Boiling point	1600 °C (1013 hPa)	-
Particle size	21 nanometer	-
Density	4,500 kg/cm3 (25 °C)	820-845 kg/m3
Molar mass	233.38 g/mol	-
Melting Point	1560 °C	-

Table 4. Activated Carbon (AC) specifications [16]

Properties	AC
Specific surface area (m2/g)	962.5
Porous volume (cm3/g)	0.312
Carbon (%)	52.49
Oxygen (%)	31.3
Potassium (%)	0.432
Si (%)	1.739
Ash content (%)	4.8
Iodine number (mg/g)	815.525

2.2 Preparation of fuel mixtures

Fuel samples (D100, B20D80, B20D80-Safflower, B20D80-Waste Oil, B20D80-Olive Stone, and versions with additives) were prepared in volumetric quantities and subjected to standard filtration to remove impurities before testing. They were mixed in a magnetic stirrer until homogeneous. After the nanoparticles were added to the liquid fuels, they were mixed for a sufficient time.

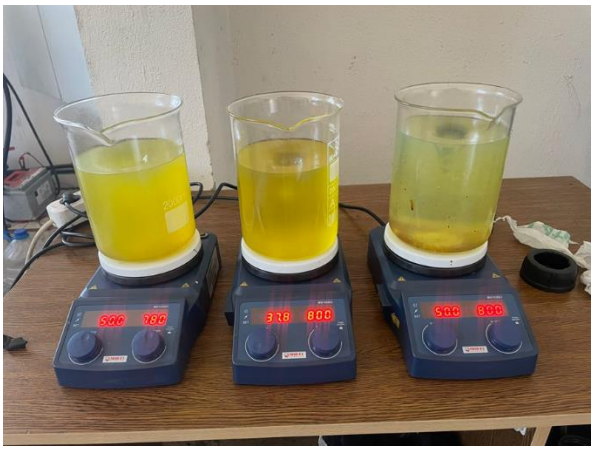

Fig.14 Preparation of fuel mixtures

After adding the nanoparticles, the mixture was mixed at 800 rpm for 30 minutes. To avoid sedimentation and ensure homogeneous use of the mixture, the fuel was used immediately after mixing.

Table 5. Fuel mixtures

Fuel Type	
D100	Pure Diesel
D100_50T	Pure Diesel + 50 ppm TiO2
D100_50T_50AC	Pure Diesel + 50 ppm TiO2+50 ppm Activated Carbon
BOS20D80	%20Oil Seeds Biodiesel+%80 Diesel
BOS20D80_50T	%20Oil Seeds Biodiesel+%80 Diesel + 50ppm TiO2
BWO20D80	%20Wate Oil Biodiesel+%80 Diesel
BWO20D80_50T_50AC	%20Wate Oil Biodiesel+%80 Diesel+ 50 ppm TiO2+50 ppm Activated Carbon

2.3 Engine Test System Setup

The engine system used in the tests was a multi-cylinder, turbocharged, electronically controlled diesel engine, connected to a dynamometer to control load and speed.

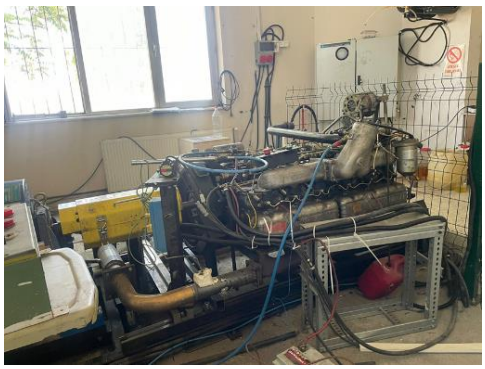

Fig.15 The Test Engine

Table 6. The Test Engine Properties

Bore and Stroke	133 mm, 140 mm
Number of cylinders	6
Displaced volume	11,670 cc
Compression ratio	16.5
Injection timing	16 'BTDC

2.3 **Performance Data**

Load and Speed Adjustment; For each test fuel, the engine was operated at constant speeds under low, medium, and full load. This allowed the fuel performance to be evaluated under both partial and full combustion conditions. Brake Thermal Efficiency; The mechanical power generated by the engine was calculated by dividing it by the chemical energy provided by the fuel. This calculation was based on instantaneous fuel flow, calorific value, and output power parameters. Brake Specific Fuel Consumption; The amount of fuel delivered to the engine was continuously recorded using a fuel consumption meter. Specific fuel consumption (g/kWh) was calculated by dividing the obtained values by the unit power produced.

2.4 Exhaust Gas Temperature Measurement

Fig.16 Bosch BEA Exhaust Analyzer

For each test point, instantaneous temperature values were recorded using temperature sensors at the exhaust outlet. This data was evaluated to analyze combustion efficiency and engine load levels. Exhaust Emission Analysis: Emission levels were determined using a gas analyzer attached to the exhaust outlet. Data from each test were analyzed to compare environmental performance between different fuels.

3. RESULTS AND DISCUSSION

3.1 Engine Performance

In internal combustion engines, brake thermal efficiency (BTE) is the ratio of the brake power generated to the chemical energy of the fuel. This value (BTE) is an indicator of how much of the fuel's chemical energy is used usefully [17].

$$\eta_{th} = \frac{P_b}{\dot{m}_f \times LHV} \quad (1)$$

P_b: braking power,
$\dot{m}_f$: fuel mass flow rate,
LHV: the lower heating value of the fuel [17]

In this study, the D100_50T fuel was observed to have the highest thermal efficiency (BTE). The second-highest thermal efficiency was observed for the BOS20D80_50T fuel. Consequently, the addition of TiO2 nanoparticles to both the D100 and BOS20D80 fuels was found to increase thermal efficiency. In contrast, the addition of nanoparticles to the BWO20D80 fuel did not significantly improve thermal efficiency**.**

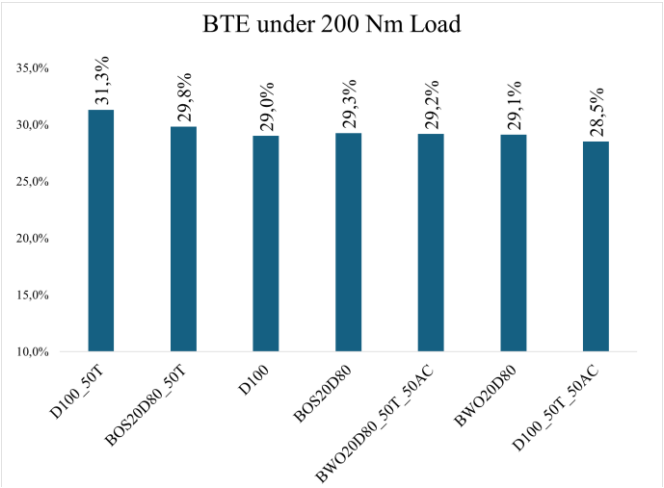

Fig.17 Brake Thermal Efficiency – under 200 Nm Load

The NO emission rates obtained in the experiments are given in Figure 18. The NO emission value of BOS20D80 fuel was dramatically higher than that of the other fuels. The addition of nanoparticles to D100 fuel caused an increase in NO emissions.

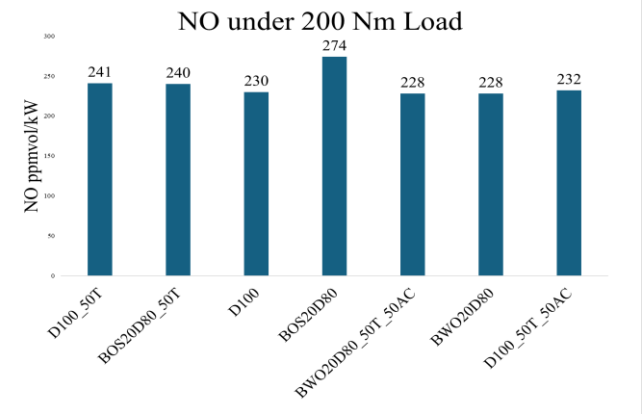

Fig.18 NO emission – under 200 Nm Load (Torque)

4.CONCLUSION& SUGGESTIONS

In this study, biodiesel was produced from olive pits. Experiments were also conducted using diesel, biodiesel (produced from olive pit oil and waste oil), TiO2, and activated carbon nanoparticles. The main results obtained from the experiments are presented below.

1- The addition of TiO2 nanoparticles to both the D100 and BOS20D80 fuels was found to increase thermal efficiency.

2- The addition of nanoparticles to D100 fuel caused an increase in NO emissions.

3- The use of agricultural wastes such as olive pits in biodiesel production should be encouraged for both economic and environmental sustainability.

4- While TiO_2 and activated carbon additives improve combustion quality in certain biodiesel types, optimization based on blend characteristics is recommended.

5- Engine tests should be expanded to include long-term performance and emissions measurements.

6- CFPP and pour point tests should be repeated in different environments to further examine fuel behavior in cold weather conditions.

7- In the future, the effects of biofuels should be investigated more thoroughly using advanced characterization methods such as particulate emissions, engine sludge formation, and combustion analysis.

REFERENCES

[1] Kumar, S. S., Rajan, K., Mohanavel, V., Ravichandran, M., Rajendran, P., Rashedi, A., ... & Afzal, A. (2021). Combustion, performance, and emission behaviors of biodiesel fueled diesel engine with the impact of alumina nanoparticle as an additive. Sustainability, 13(21), 12103.

[2] Jaikumar, S., Srinivas, V., & Meher, R. S. (2021). Combustion characteristics of direct injection diesel engine fueled with dispersant-mixed Al2O3 nanoparticle-added biodiesel blend. International Journal of Thermophysics, 42(6), 91.

[3] Rangabashiam, D., V, J., S, G., M, N., & Rameshbabu, A. (2023). Emission, performance, and combustion study on nanoparticle-biodiesel fueled diesel engine. Energy Sources, Part A: Recovery, Utilization, and Environmental Effects, 45(3), 8396-8407.

[4] Sel, M. (2013). Nano katkı maddeli biyodizel yakıtlarının emisyon ve performans analizi. Yüksek Lisans Tezi,

[5] Hacıkadiroğlu, S. (2007). Dizel-biyodizel karışımlarının motor performansı ve emisyonlara etkisi. Yüksek Lisans Tezi,

[6] Kaya, A. (2006). Ham ve atık bitkisel yağlardan biyodizel üretimi ve karakterizasyonu. Yüksek Lisans Tezi,

[7] Örs, M. (2016). Bütanol katkılı biyodizelin emisyonlara ve performansa etkisi. Yüksek Lisans Tezi,

[8] Aydoğan, M. (2008). Bitkisel yağlardan biyodizel üretimi ve motor performansına etkisi. Yüksek Lisans Tezi,

[9] Nişancı, F. (2007). Bitkisel yağlardan elde edilen biyodizellerin motor performansına etkileri. Yüksek Lisans Tezi,

[10] Kaya, Y. (2010). Kanola yağından elde edilen biyodizelin motor performansına etkisi. Yüksek Lisans Tezi,

[11] Ilgazlı, A. (2010). Biyodizel yakıtlarının motor performansına ve emisyonlara etkisi üzerine deneysel bir çalışma. Yüksek Lisans Tezi

[12] Peker, K. (2009). Atık zeytinyağından biyodizel üretimi ve karakterizasyonu. Yüksek Lisans Tezi,

[13] Kül, V. S., Akansu, S. O., & Çınar, G. (2024). Experimental investigation of the effects of aqueous ammonia and water mixtures on the efficiency and emissions of a compression ignition engine. Process Safety and Environmental Protection, 191, 1495-1503. https://doi.org/10.1016/j.psep.2024.09.051

[14] Demirbas, A. (2009). Production of biodiesel from algae oils. Energy Sources, Part A: Recovery, Utilization, and Environmental Effects, 31(2), 163–168. https://doi.org/10.1080/15567030701739245

[15] Kül, V. S., Akansu, S. O., Sarıtaş, M., Sinkala, H., & Ünalan, S. (2025). Investigation of the effect of utilisation of nano boron, diesel and biodiesel fuels with together hydrogen in a compression ignition engine on combustion characteristics. International Journal of Thermofluids, 101232. https://doi.org/10.1016/j.ijft.2025.101232

[16] Ossman, M. E., Fatah, M. A., & Taha, N. A. (2014). Fe (III) removal by activated carbon produced from Egyptian rice straw by chemical activation. Desalination and Water Treatment, 52(16-18), 3159-3168. https://doi.org/10.1080/19443994.2013.796895

[17] Kül, V. S., & Sarıtaş, M. (2025). Investigation of the Effect of Stearic Acid Addition to Diesel on Combustion in a Compression Ignition Engine Energy, Environment and Storage. https://doi.org/10.52924/ZDOJ8219

[18] Sarıtaş, M., & Kul, V. (2024). Effects of Magnetic Fields and Nanoparticle Additives on Diesel Engine Emissions and Performance: A Comprehensive Experimental Analysis. Energy, Environment and Storage

Journal, 4(03). https://doi.org/10.52924/ZYRI4684

[19]Kumar, N., Raheman, H. 2022. "Production, characterization and utilization of second generation biodiesel blend in diesel engine using water and nanoparticles as additives" Fuel, 308, 122063. https://doi.org/10.1016/j.fuel.2021.122063

[20] Vellaiyan, S., Subbiah, A., Chockalingam, P. 2020. "Effect of titanium dioxide nanoparticle as an additive on the exhaust characteristics of diesel-water emulsion fuel blends" Petroleum Science and Technology, 38(3), 194-202. https://doi.org/10.1080/10916466.2019.1702677

Energy, Environment and Storage (2025) 05-03: 113-127

Energy, Environment and Storage

Journal Homepage: www.enenstrg.com

Tailoring Activated Carbon Surfaces: A Comparative Study of Nitric and Chlorosulfonic Acid Modifications

Betul Aykut-Senel[1], Cihan Ozgur [2], Sehnaz Sule Kaplan-Bekaroglu[1], Nuray Ates[3]

[1]*Suleyman Demirel University, Engineering Faculty, Department of Environmental Engineering, 0000-0003-3674-5525, 0000-0003-0917-7219*

[2]*Isparta University of Applied Sciences, Sutculer Prof. Dr. Hasan Gurbuz Vocational High School, 0000-0001-6085-1585*

[3]*Erciyes University, Engineering Faculty, Department of Environmental Engineering, 0000-0002-8923-4852*

ABSTRACT. Surface modification approaches can improve the adsorbent's physicochemical characteristics, which are crucial to the adsorption process's effectiveness. In this study, the effects of chemical modification on the structural and chemical properties of four different powdered activated carbon (AC) samples were investigated. Surface modifications were performed using nitric acid and chlorosulfonic acid. The modified adsorbents were comprehensively characterized by Brunauer–Emmett–Teller (BET) surface area analysis, Scanning Electron Microscopy (SEM), Fourier Transform Infrared Spectroscopy (FTIR), and Dynamic Light Scattering (DLS). Additionally, the Boehm titration method was employed to evaluate the surface acidity and functional group composition. According to the research results, nitric acid modification led to a smoother and more uniform surface morphology, along with a more consistent pore size distribution, compared to chlorosulfonic acid treatment. Nitric acid introduced functional groups such as –OH, –COOH, and C=C=C, while chlorosulfonic acid resulted in the incorporation of sulfonic groups (S=O and SO_3 H). Among the modified samples, AC4S exhibited the highest surface area (868.48 m^2/g) and pore volume (0.88 cm^3/g). The largest average particle size (1419.44 nm) was observed in the AC1S sample. While double modification increased particle size distribution, it negatively affected surface area and pore volume. Overall, the findings indicate that both nitric acid and chlorosulfonic acid modifications are effective in tailoring the chemical and structural features of activated carbon, offering promising potential for adsorption-based applications.

Keywords: Activated carbon, adsorption, characterization, chemical modification, chlorosulfonic acid, nitric acid.

Article History: Received: 10.August 2025 Revised: 04 September 2025; Accepted: 10 September 2025; Availableonline: 10 September 2025
Doi: https://doi.org/10.52924/SUTR5652

1. INTRODUCTION

Restoring ecosystem balance and ensuring a more sustainable future need study on the removal of micropollutants from water at low concentrations (µg/l-ng/l), such as pesticides, drugs, and personal care products. Conventional treatment methods are not efficient enough to remove these pollutants from water [1]. Adsorption is one of the most promising advanced treatment technologies, especially for the removal of micropollutants, due to its high removal capacity, ease of application and no toxic by-products [2]. The biggest disadvantage of the adsorption process is the need for regeneration [4]. At this point, this problem can be eliminated by using commercial powdered activated carbon (PAC) in the adsorption process.

Adsorption performance is generally evaluated according to the capacity and selectivity of adsorbents and considering this situation, adsorbent selection is an important factor in pollutant removal [3]. In the interest of environmental sustainability, high-performance materials like activated carbon are now needed for the adsorption of persistent organic and inorganic chemicals from water sources. In general, activated carbon (AC) is an amorphous type of carbon that can be produced from various carbon sources employing one of the two fundamental activation techniques chemical or physical. [5-7]. The material has several uses in a variety of sectors due to its high surface area, porosity, advanced internal pore structure with micro, meso, and macro pores, and a large number of functional groups on its surface [8].

The addition of different functional groups and/or structural modifications to ACs improves their characteristics by increasing their selectivity and capacity

*betulsenel@sdu.edu.tr

for adsorption of contaminants. In particular, recent studies on modifying adsorbents to increase their capacity present an innovative adsorption approach to the literature. Numerous methods have been examined in the literature, including chemical, biological, and physical change [9-13]. It is well known that these modified ACs enhance the adsorbent structure and boost the adsorption capacity [14-16].

Differences in the modification procedure and the type of modifying agent used have a direct impact on how the AC adsorbs pollutants and how it works [17]. Therefore, choosing the right modification technique is very important on the physicochemical structure of the AC. The specific surface area of the adsorbent can be increased, surface functional groups, pore structures and particle size distributions can be changed by AC modification. In particular, chemical modification techniques that use organic acids, hydrogen peroxide, and inorganic acids (such as hydrochloric, sulfuric, and nitric acids) are successful in boosting the quantity of surface functional groups [13, 18, 19].

Modification of AC with nitric acid resulted in the formation of functional groups with a high amount of accessible oxygen on the adsorbent surface in the studies conducted by Gökçe and Aktaş [20] and Valentin-Reyes et al. [21]. Following modification, Li et al. [22] found that groups like lactone and carboxyl enhanced the number of oxygen-containing groups on the AC's surface while also making the surface more hydrophilic. Wolak and Orzechowska-Zięba [13] claimed in their study that when polar adsorbates are adsorbed, the presence of oxygen groups on the carbon surface is evident. In many studies using nitric acid as oxidizer, it was observed that the modification had a positive effect on the micropore and mesopore volume, increasing the adsorption capacity of pollutants [23-25]. Liu et al. [26] observed that the adsorption capacity of Cr (VI) increased from 7.61 mg/g to 13.74 mg/g as a result of AC modification with nitric acid. In another study, the increase in adsorption capacity from 24.86 mg/g with the original AC to 54.74 mg/g as a result of modification with nitric acid is an important result [27].

Recently, it has been thought that sulfonic acid modification, another technique that may raise surface acidity, has a lot of promise [28]. Alvear-Daza et al. [29] reported that very strong acid sites were formed as a result of the effective incorporation of SO_3H compound into the structure by chlorosulfonic acid modification. When Goswami and Phukan [30] used sulfonic acid modification to remove dyes (RhB and Orange G), they found that the adsorption capacity rose from 318.5 mg/g to 757.6 mg/g.

Characterization of the adsorbent's properties is necessary to assess the effectiveness of the adsorption process and get a better understanding of it [31].

Various methods have been developed to characterize structural and physicochemical properties such as pore volumes, surface area, thermal stability, hydrophilicity, surface chemistry, functional groups of surfaces, pH, elemental analysis, water vapor adsorption, nitrogen adsorption, moisture content [32]. Scanning electron microscopy (SEM), Transmission electron microscopy (TEM), N_2 adsorption/desorption isotherm, Fourier transform infrared spectroscopy (FTIR), X-Ray photoelectron spectroscopy (XPS), Boehm titration, Potentiometric titration, Zero charge point are some of the commonly used characterization techniques for adsorbents [33, 34].

In this paper, commercial powdered activated carbons, which are preferred for obtaining adsorption modified adsorbents, were modified with nitric acid and chlorosulfonic acid. In the literature searches, no recent study comparing the modification of commercial powdered AC with nitric acid and sulfonic acid was found. The effect of double modification (steam+nitric acid, steam+sulfonic acid, chemical treatment+nitric acid, chemical treatment+sulfonic acid) was also investigated in this study. The effect of modification on adsorbent structures was elucidated by SEM, Brunauer, Emmet and Teller (BET), FTIR and dynamic light scattering (DLS) analysis. At the same time, the changes in surface chemistry were investigated by pH_{PZC} and surface acidic and basic groups experiments.

2. MATERIALS AND METHODS

2.1 Materials and chemicals

In the modification studies, four commercial powder ACs were used: Norit CA1 (Cat. No. 97876), Norit SX F Cat (Cat. No. 901933), AC Puriss (Cat. No. 31616), and Norit SX ULTRA (Cat. No. 53663). Chemical modification was done to Norit CA1, and steam modification was done to Norit SX ULTRA. The two additional ACs are original, untreated activated carbons that were acquired from Sigma-Aldrich. The general characteristics of the ACs are presented in Table 1. The concentrated nitric acid (specific gravity 1.43 g/m^3, 65% purity) used for modification was of high purity and was supplied by Merck. Purchased from Sigma-Aldrich were hydrochloric acid (specific gravity 1.19 g/m3, 37% purity) and chlorosulfonic acid ($ClSO_3H$), with a specific gravity of 1.48 g/m3, 99% purity.

Table 1. Properties of commercial adsorbents used in modification experiments

Adsorbents	Surface Area (m^2/g)	Pore size	Density (g/ml)
Norit CA1	1400	Macro/Meso	0.9
Norit SX ULTRA	1200	Micro/Meso	0.743
Norit SX F Cat	750	Micro/Meso	1.8 – 2.1
AC Puriss	300	Micro/Meso	1.8 –2.1

2.1.1 Nitric acid modification of activated carbons

In the nitric acid modification of PACs, the method of Guha et al. [35] was modified and applied. Prior to modification, the adsorbents were cleaned with deionized and distilled water and dried at 105 ^oC in an oven.

Five steps were used to modify the dried activated carbons. Summary of the five-step modification process:

1. HCl Pre-treatment: The activated carbon is treated with 2.5 M HCl at 120 °C for 18 hours to remove impurities.

2. Boiling in Water: The sample is boiled in pure water at the same temperature for 8 hours to further purify it.

3. Nitric Acid Modification: The AC is treated with 7 M HNO_3 at 120 °C for 16 hours to introduce functional groups that can enhance adsorption.

4. Washing: The modified AC is washed with distilled and deionized water until a constant pH of ~5-6 is achieved.

5. Drying: Ultimately, a vacuum oven is used to dry the AC at 60-70 °C for about 48 hours until a constant weight is reached, indicating complete drying.

The 40% weight loss during washing is significant, as it reflects the removal of soluble impurities and possibly some of the carbon structure. The resulting modified activated carbons are labeled as ACN (*Table 2*).

2.1.2 Chlorosulfonic acid modification of activated carbons

The technique used by Goswami and Phukan [30] in their study was adapted and used to modify activated carbons using sulfonic acid. It was carried out in 5 step. Each step of the method is clearly summarized below.

1. Preparation of Activated Carbon:

Washing: Water that was deionized and distilled was used to wash the activated carbons.

Drying: 105 °C in an oven to dry.

2. Dichloromethane Treatment:

Weighing: 30 grams of activated carbon were weighed.

Solution Preparation: 900 mL of dichloromethane ($CH_2\ Cl_2$) was added.

Ultrasonic Bath: Stirred for 45 minutes.

Cooling: Cooled using ice molds.

3. Chlorosulfonic Acid Addition:

Dropwise Addition: 30 mL of chlorosulfonic acid was added dropwise over 30 minutes at room temperature.

Shaking: The mixture was agitated for an additional 3 hours to ensure complete dispersion of the acid.

4. Filtration and Washing:

Filtration: The final product was filtered.

Washing: Washed with ethanol and water.

5. Final Drying:

Drying: Dried at 80 °C until a constant weight was achieved.

Storage: The dried activated carbons were stored in a desiccator.

Final Product: The modified activated carbons were labeled as **ACS** (*Table 2*).

Table 2. Properties and codes of original and modified adsorbents

Adsorbents	Codes	Properties
Norit SX ULTRA	AC1	Original steam modification
Norit CA1	AC2	Original chemical modification
Norit SX F Cat	AC3	Original
AC Puriss	AC4	Original
Norit SX ULTRA	AC1N	Steam + Nitric acid modification
Norit CA1	AC2N	Chemical + Nitric acid modification
Norit SX ULTRA	AC1S	Steam + Sulfonic acid modification
Norit CA1	AC2S	Chemical + Sulfonic acid modification
Norit SX F Cat	AC3N	Nitric acid modification
Norit SX F Cat	AC3S	Sulfonic acid modification
AC Puriss	AC4N	Nitric acid modification
AC Puriss	AC4S	Sulfonic acid modification

2.2 Characterization techniques

2.2.1 pH_{PZC} analysis

The neutral charge point (pH_{PZC}, the pH value at which the total net surface charge is zero) and the ability to neutralize acids and bases are qualities that define the surface chemistry of adsorbents. The pH_{PZC} values of activated carbon samples were determined by pH equilibration method [36]. By adding 0.5 M HCl and/or 0.5 M NaOH, the pH values of the 0.1 M NaCI solution produced in distilled water were brought within the range of 2 and 12. From these solutions, 20 ml of samples were taken in 25 ml amber sample bottles and 100 mg of adsorbent was added to each. Adsorbent-free control samples were also made for every pH level. The prepared samples were shaken for 48 hours at 20±5 0C and 100 rpm. Following the mixing time, the samples were allowed to settle for an hour before their pH levels were determined. The pH_{PZC} value is the same pH value that does not change after 48 hours of contact. Nonetheless, in order to determine the pH_{PZC} value precisely, interpolation is typically necessary. The effect of acid modification on the adsorbent's net surface charge was ascertained by noting the pHpzc values of the original and modified activated carbons that remained consistent over a 48-hour period.

2.2.2 Total surface acidic and basic values of adsorbents

The Boehm technique (alkalimetric titration) was used, with some slight adjustments, to quantify the total surface acidic groups (NaOH adsorption) and total surface basic groups (HCl adsorption) [36]. 20 ml of 0.05 N NaOH or 0.05 N HCl solution was added to 25 ml bottles containing 200 mg of adsorbent each. Control samples without adsorbent were also prepared with the samples. For 48 hours at room temperature, the prepared samples were

agitated at 100 rpm. After the specified period of time, the samples were left for an hour to allow the adsorbents to settle before being filtered. Taking into account pH variations, ten milliliters of the filtered samples were used in the titration procedure. The final stage was titrating the solution with 0.05 N HCl using 0.05 N NaOH. The total number of surface basic groups was determined by comparing the quantity of NaOH absorbed by the control sample with the sample that included the adsorbent. To find the total number of acidic groups on the surface, 0.05 N HCl was used to titrate the sample that contained 0.05 N NaOH. The amount of total surface acidic groups was calculated by using the amount of HCl consumed for the sample containing adsorbent and the control sample.

2.2.3 Surface area measurement (BET) analysis

The Micromeritics Gemini VII Surface Area and Porosity Surface Analyser was used to measure the adsorbents' surface areas and total pore volumes. N_2 adsorption-desorption isotherms were used to determine the surface area of adsorbents. BET analyses were carried out at Erciyes University Technology Research and Application Centre.

2.2.4 Scanning electron microscope (SEM) analysis

SEM analyses of the original and modified adsorbents were carried out at Erciyes University Nanotechnology Research Centre. Using a Zeiss Evo LS10 scanning electron microscope (SEM), the surface morphology of the adsorbents was reviewed.

2.2.5 Fourier transform infrared spectrometry (FTIR-ATR) analysis

FTIR analyses provide information at the molecular level about new functional groups added to the surface or changes on the surface as a result of surface modification processes. FTIR analyses of the original and modified adsorbents were measured in the wavelength range of 400-4000 cm^{-1} by Perkin Elmer 400 Ft-IR/FT-FIR device at Erciyes University Technology Research and Application Centre.

2.2.6 Particle size distribution analysis

The dynamic light scattering (DLS) technique was used to determine the particle size distribution of the original and modified activated carbons. A Malvern NanoZS90 device with a 633 nm laser was used to perform DLS measurements at room temperature. A scattering angle of 173° was used to acquire the data.

Dimensional analyses were performed at Erciyes University Nanotechnology Research Centre on a retainer basis.

3. RESULTS AND DISCUSSIONS

3.1 SEM Analyses

SEM analysis is a method for figuring out the physical characteristics and surface morphology of the materials being studied. The adsorbents modified by nitric acid and sulfonic acid are shown in Figure 1 as SEM images with a size of 2 µm and a magnification scale of 500 KX. Upon examining the AC1 and AC2 adsorbents prior to modification, they exhibit a very wide particle size distribution, containing very small, activated carbon granules within their structure. Post nitric acid modification, both adsorbents (AC1N, AC2N) appear more homogeneous in terms of size. During the nitric acid modification, repeated washing of activated carbon with acid and pure water results in the removal of the smaller activated carbon particles.

Consequently, as evidenced by the SEM images of AC1N and AC2N adsorbents, larger and cleaner activated carbon granules remain. This characteristic is attributed to the modification process's cleansing impact. A similar observation was reported by Ge et al. [37], who noted that the surface of the modified adsorbent was cleaner and the surrounding pores smoother. Additionally, literature reports indicate that post nitric acid modification, activated carbon forms a smoother, more uniform, and narrow-pored structure, supported by a reduction in BET surface area [25, 38, 39].The SEM images of AC1N and AC2N adsorbents also corroborate the low surface area obtained from BET analysis results. Moreover, a number of investigations in the literature have documented that the physical shape of activated carbon may be considerably impacted by nitric acid treatment [40-42].

Upon examining the SEM images of the AC3N and AC4N adsorbents, it is observed that a clean and smooth structure similar to that of other adsorbents has formed. Lu et al. [14] noted that the surface morphology of adsorbents activated with coconut exhibited a clean and eroded appearance due to the oxidation by nitric acid. Unlike the other adsorbents, the AC3 and AC4 adsorbents showed a significant increase in surface area as a result of nitric acid modification. This is attributed to the fact that AC3 and AC4 are original (untreated) adsorbents, while AC1 and AC2 are pre-treated adsorbents. It was concluded that the modification of untreated adsorbents with nitric acid positively impacts the surface area. According to Su et al. [25], mass transfer during adsorption was facilitated by the creation of new pores following nitric acid modification, which expanded the contact area.

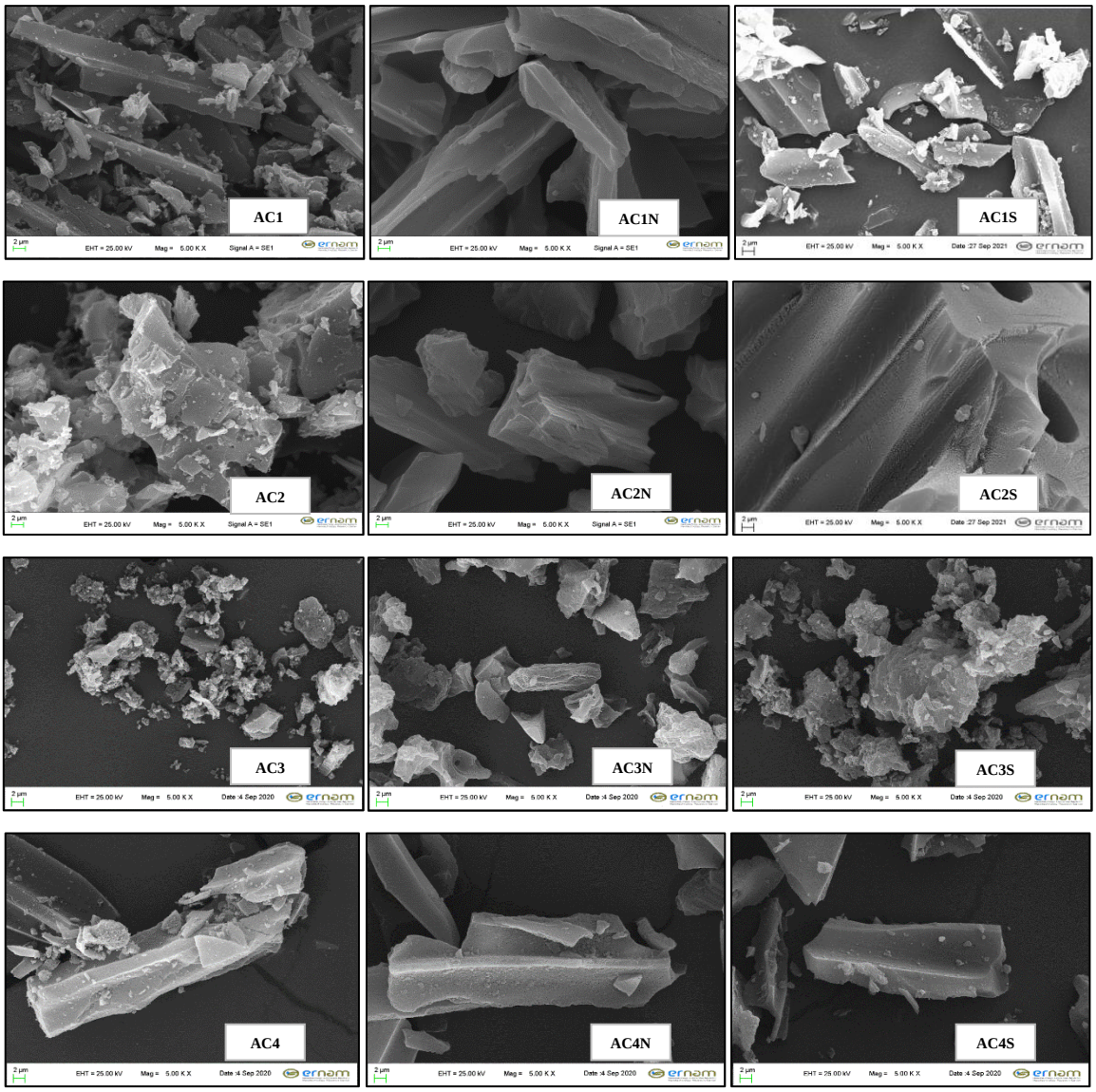

Figure 1. SEM images of original and modified ACs (2 µm mag: 500 KX)

3.2 FTIR Analyses

Figure 2 shows the FTIR spectra of the original and modified AC1 and AC2 adsorbents. In the FTIR spectrum of the AC1 adsorbent, bands observed at 2987.3 cm^{-1} and 2899.6 cm^{-1} are attributed to the aliphatic υ(C-H) stretching in the –CH– bond found in the aromatic methoxyl group and the side chains of methyl and methylene groups [43]. Both symmetric and asymmetric C-H vibrations are linked to bands seen roughly between 2950 and 2800 cm^{-1}, suggesting the existence of aliphatic compounds [44]. The band in the range of 1800-1300 cm^{-1} is characteristic of highly conjugated C=O stretching and C-O structures [45]. The peak at 1407.2 cm^{-1} is attributed to the C=O stretching vibration of carboxylic acid or ketone. The presence of peaks at 1080 and 1300 cm^{-1} in the AC1 spectrum can be associated with the C-O stretching vibrations of carboxylic acids, phenols, alcohols, or esters [30]. The FTIR spectra for AC1 reveal that the modification with HNO3 resulted in significant chemical changes in the structure of AC1N, with the disappearance of many bands. There are just two large peaks in the modified AC1N spectrum, and these may be linked to the allen (C=C=C) group. Another band around 2100 cm^{-1}, which is relatively broad, is also attributed to the allen (C=C=C) group [46-47].

In the FTIR spectrum of the AC2 carbon, the peaks at 2986.9 cm^{-1} and 1987.6 cm^{-1} disappeared after nitric acid modification. The 2099.2 cm^{-1} band in the AC2 sample slightly increased after modification, forming the 2111.5 cm^{-1} band. This relatively broad peak around 2100 cm^{-1} is attributed to the allen (C=C=C) group [46-Figure 3 presents the FTIR spectra of original and modified AC3 and AC4 activated carbons. The original AC3 carbon structure includes bands at 2314, 2103, 2000, and 585.44 cm^{-1}. Nitric acid modification caused the bands at 2103 and 2314 cm^{-1} to widen, and peaks at 2355 and 2116 cm^{-1} to emerge. The 585.4 cm^{-1} band decreased after nitric acid modification, with a peak observed at 576.8 cm^{-1}. Upon examining the FTIR spectrum of AC4 and nitric acid-modified AC4N carbon, it was observed that the band at 3793 cm^{-1} disappeared after nitric acid modification, replaced by a peak at 3564 cm^{-1}. Peaks in the range of approximately 3700-3500 cm^{-1} are attributed to –OH groups [30].

The broad and strong band observed between 3655-3000 cm^{-1} after both modifications is attributed to the stretching vibration of ν(O-H) from adsorbed water or functional groups on the surface [43]. The sulfonic acid modification of the original AC3 carbon resulted in a peak at 1058.4 cm^{-1} corresponding to the S=O structure in AC3S carbon. Similarly, Huang et al. [54] associated peaks between 1030-1100 cm^{-1} with sulfonic structures. Following sulfonic acid modification, the band at 3793 cm^{-1} in the spectra of AC4 carbon vanished, and this was replaced by a band at 3560.3 cm^{-1} in the spectrum of AC4S carbon. Additionally, a new band at 1993.6 cm^{-1} was observed in AC4S, indicating functionalization of the adsorbent surface with S=O and SO3H groups. In a similar vein Kamari et al. [55] associated peaks with the S=O groups and SO3H group OH stretching absorption roughly between 1649 and 2900 cm^{-1}. Double-bonded C=O groups are responsible for the peaks in the AC4S carbon spectrum that are seen between 2100 and 2400 cm^{-1} [41]. At some point the findings show that, depending on the properties of the targeted contaminants, activated carbon functionalized with sulfonic acid can be employed in adsorption investigations with good results.

47]. The presence of carboxyl groups produced by nitric acid is shown by the signal in the AC2N sample at 1707 cm^{-1} [8]. Similarly, Schepetkin et al. [48] observed a strong absorbance in the 1650-1720 cm^{-1} band, which they attributed to –COOH group vibrations. Another study associated the peak at 1729 cm^{-1} with the specific peak of the C=O bond stretching vibrations in the carboxylic acid functional group [49]. Shim et al. [50] reported an increase in adsorption bands in the 1750-1400 cm^{-1} range for carboxylic acid and quinone groups when comparing the spectra of activated carbon fibers modified with HNO3 to general spectra.

The bands observed between 1500-1600 cm^{-1} in both spectra of AC2N and AC2S originate from C=C stretching vibrations in the aromatic rings of quinone and keto-enol [51]. According to the FTIR data, oxidation with HNO_3 produces a number of surface functional groups, including quinone, carboxyl, and carbonyl. Following activated carbon activation, certain functional groups persisted while others were destroyed or new functional groups were created, according to an analysis of the FTIR spectrum. This observation aligns with the literature, confirming the presence of observed functional groups for AC2N in our experiments [52]. New peaks appeared at 3791 cm^{-1} and 3483 cm^{-1} in AC1S carbon, and at 3289.8 cm^{-1} in AC2S carbon. These peaks around 3300 cm^{-1} correspond to the –OH group [53]. New peaks observed at 611.24 cm^{-1} and 530.62 cm^{-1} in AC2S adsorbent are attributed to S-O stretching vibrations [30].

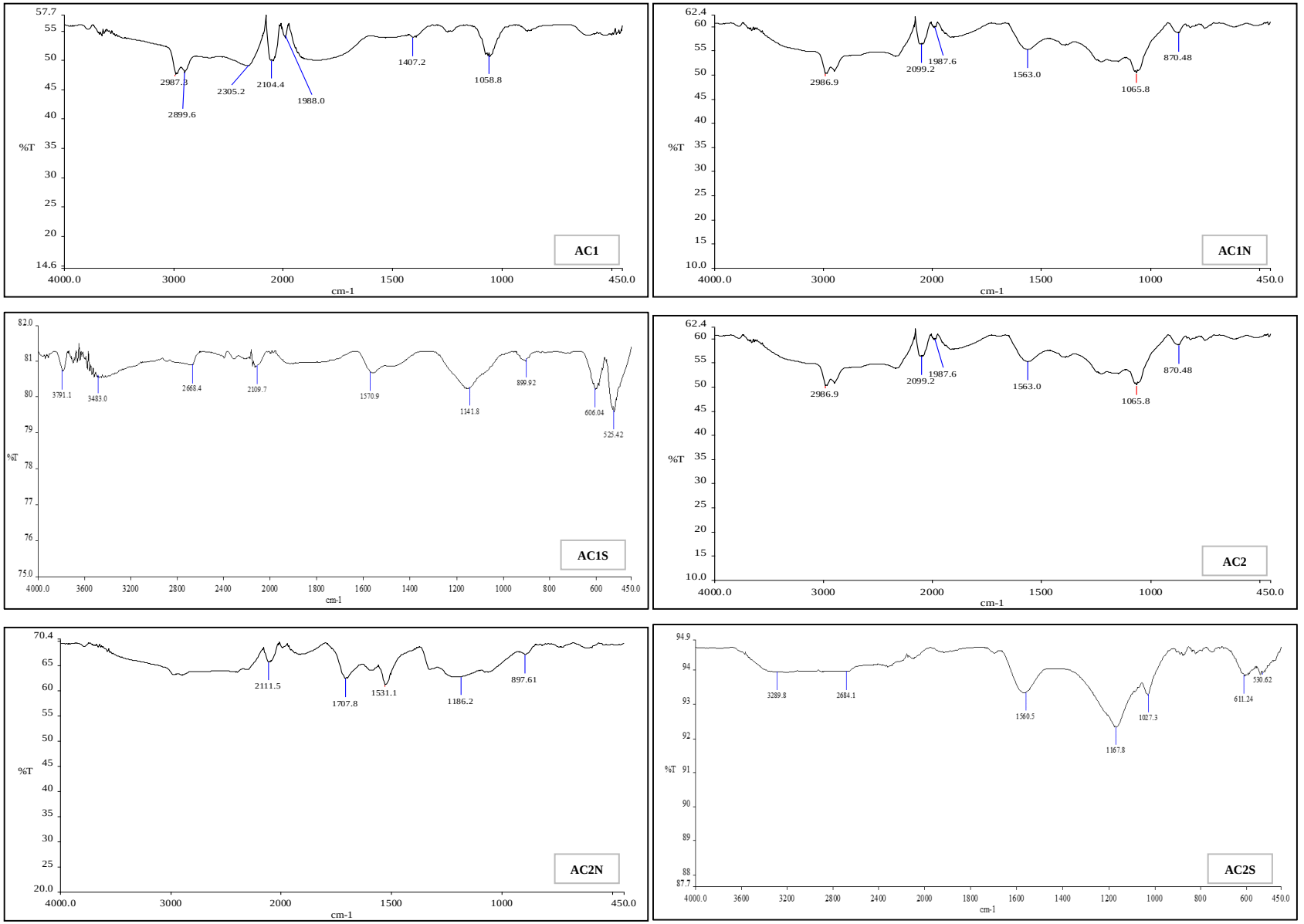

Figure 2. FTIR spectra of original and modified AC1 and AC2 activated carbons

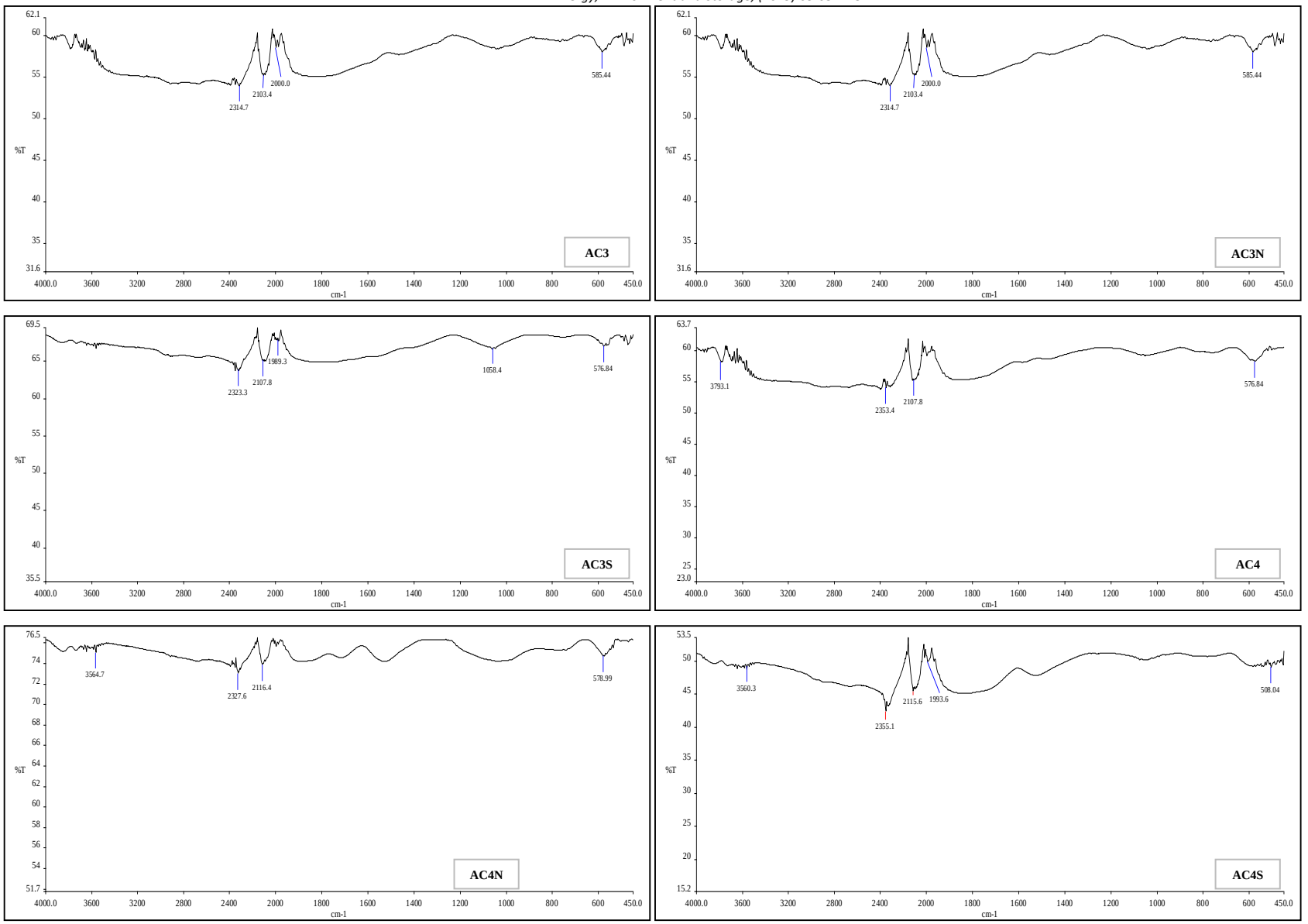

Figure 3. FTIR spectra of original and modified AC3 and AC4 activated carbons

3.3 BET Surface Area, Pore Volume, and Pore Size Analysis Results

N_2 adsorption-desorption isotherms were used to explain how modifications affected surface area and pore characteristics. The pore structure properties obtained from these isotherms are provided in Table 3. Table 2 makes it abundantly obvious how the structural properties of the activated carbon samples were affected by nitric acid and sulfonic acid modifications. Each modification agent can cause significant and distinct changes in the adsorbent structure, underscoring the importance of understanding the behavior of each agent (nitric and sulfonic acid). BET analysis based on nitrogen gas adsorption at 77 K revealed changes in surface area and porosity measurements as a result of both modifications. Nitric acid modification caused to a decrease of 39% and 76% in surface areas of AC1 and AC2 adsorbents, respectively. There are two potential implications that many researchers attribute to this observation: The first is the partial breakdown of microporous walls [10, 56, 57], and the second is the obstruction of pore entrances as a result of the development of oxygen functional groups [58]. Conversely, other studies interpret the increase in surface area after nitric acid treatment as dissolution of ash and opening of some blocked pores in activated carbon ShamsiJazeyi and Kaghazchi [49], which was observed as a 30% increase only in AC3N adsorbent. In contrast, after sulfonic acid modification, AC3 showed a slight decrease in surface area, whereas AC4 exhibited a significant increase from 273.56 m²/g to 868.48 m²/g.

Table 3. Pore structure characterization of original and modified activated carbon samples

Adsorbent	BET Surface Area (m^2g^{-1})	Total Pore volume (cm^3g^{-1})	Pore Diameter (nm)
AC1	1200	0.95	3.16
AC2	1161	1.12	3.85
AC3	656.6	0.78	4.74
AC4	274	0.22	3.24
AC1N	732	0.52	2.85
AC2N	273.56	0.22	3.24
AC3N	855.05	0.85	3.98
AC4N	822,48	0.76	3.71
AC1S	929.93	0.61	2.62
AC2S	500.59	0.48	3.81
AC3S	635.61	0.78	4.91
AC4S	868.48	0.88	4.18

SBET: Surface area calculated using the Brunauer-Emmett-Teller (BET) theory, Pore diameter: adsorption average pore width (BET 4V/A)

Total pore volume is another significant characterization outcome. Nitric acid modification resulted in a trend of pore loss in all adsorbents except AC3N and AC4N. The decrease in pore volume, similar to the decrease in surface area, has been attributed to the blocking of pores by oxygen functional groups due to chemical modification [59]. Yu et al. [60] investigated changes in carbon structure after oxidation with HNO3 at different temperatures. They reported significant destruction of pore structure in commercially modified activated carbon samples compared to other AC samples, which they associated with the strong oxidative power of concentrated HNO_3 at 120°C. In our study, the modification with HNO_3 was also conducted at 120°C, aligning our results with findings in the literature. The decreasing trend in nitric acid modification was followed by an increasing trend in sulfonic acid modification. The overall pore volume of AC4 in the AC4S sample rose significantly, from 0.22 cm³/g to 0.88 cm³/g. Due to sulfonic acid modification, the adsorbents AC1S and AC2S saw a reduction in total pore volume. Specifically, the reduction from 1.12 cm³/g to 0.48 cm³/g in AC2S is notable, indicating that repeated sulfonic acid modification may lead to structural degradation, resulting in a decrease in surface area and pore volume.

Pore diameters can improve the removal capacity for pollutants that notably target pore sizes, and they are a greater driver of activated carbon performance than total surface area alone [61]. Typically, activated carbons have three pore classifications: macropores larger than 50 nm, mesopores ranging from 2 to 50 nm, and micropores smaller than 2 nm. Both original and modified adsorbents in this study exhibit mesoporous structures ranging from 2 to 5 nm. Following nitric acid modification, the pore sizes in all samples decreased. During nitric acid modification, some mesopores were blocked, leading to a reduction in mesopore volume as shown in Table 3. Numerous research investigations have documented that the addition of HNO_3 to activated carbon decreases its BET surface area, pore volume, and pore [20, 43, 62]. In contrast, sulfonic acid modification increased pore sizes. For instance, the original AC4 adsorbent had a pore width of 3.24 nm, which increased to 4.18 nm after modification. These results indicate that nitric acid and sulfonic acid modifications alter the surface properties of activated carbons, affecting pore sizes in particular.

3.4 pH_{PZC}, Surface Acidity and Basicity

Surface acidity or basicity is an important criterion defining the surface chemistry of activated carbon adsorbents. Carboxyl, lactone, phenolic hydroxyl, quinone, and carboxylic anhydride groups are common oxygen-containing functional groups found on the surface. It has been noted that the higher the oxygen content, the more acidic the surface [20]. Surface basicity, on the other hand, is associated with oxygen-free Lewis sites at the edges of carbon layers, carbonyls, pyrone, and chromene-type structures [37]. The pHPZC findings and Boehm titration total acidic-basic groups are displayed in Table 4. Titration results indicate an increase in the total acidity of the activated carbon surface after nitric acid and sulfonic acid modifications. Particularly, an increase in total acid groups (meq/g) was observed for AC2 and AC4 adsorbents after nitric acid modification.

Gokce and Aktas [20] noted that higher initial concentrations of HNO_3 lead to increased formation of carboxylic groups on the surface, promoting the likelihood of carboxylic and phenolic groups co-locating and supporting lactonic group formation. However, at high concentrations, some basic surface functional groups can be removed from the structure. These changes are typical outcomes of oxidative modifications observed frequently in previous studies [50, 63], where oxidative effects of HNO3 during modification result in reductions of basic surface functional groups as well.

Table 4. Data obtained from the Boehm method and zero point of charge

Adsorbent	pH_{PZC}	Total Acidic Groups		Total Basic Groups	
		(meq/g)	(meq/m^2)	(meq/g)	(meq/m^2)
AC1	8.11	3.6	0.003	3.33	0.003
AC2	2.53	4.0	0.003	3.03	0.003
AC3	7.8	3.5	0.005	3.80	0.006
AC4	7.09	3.8	0.014	3.90	0.014
AC1N	2.08	4.1	0.006	3.00	0.004
AC2N	2.01	4.9	0.018	2.90	0.011
AC3N	2.88	3.950	0.005	3.725	0.004
AC4N	2.92	4.775	0.006	3.675	0.004
AC1S	4.98	3.05	0.0033	4.50	0.0048
AC2S	2.90	3.35	0.0067	4.30	0.0085
AC3S	2.9	3.950	0.006	3.650	0.006
AC4S	2.95	3.900	0.004	3.725	0.004

The number of basic sites generally decreases as a result of HNO3 modification. This can be attributed to nitric acid's ability to neutralize or even eliminate basic sites [64]. In the case of sulfonic acid modification, as observed in Table 4, there is a slight increase in total acid groups while a decrease in basic groups occurs. The most notable decrease was measured in AC4 adsorbent, where it decreased from 0.014 meq/m² to 0.004 meq/m² in AC4S adsorbent. The adsorption capacity of contaminants in aqueous solutions is influenced by the pH at which the surface of the adsorbent becomes positively or negatively charged, as shown by measurements of pH_{PZC} [65]. The pH equilibrium technique was used to determine the adsorbents' pH_{PZC} values [36]. All modified carbons were observed to have lower PZC values compared to the original carbon samples. This indicates that acidic properties are dominant as a result of the modification process and that there are more weak acidic functional groups compared to others.

The adsorbent with the least change in pHPZC value is AC2, which decreased from 2.53 to 2.01 after modification to AC2N. On the other hand, despite a slight decrease in pHpzc value after modification for AC2, a significant increase in total acidic groups was observed. This phenomenon is associated with the strong oxidative effect of nitric acid modification. For AC3, AC4, and AC1 samples modified with sulfonic acid, a decreasing trend in pHpzc values was observed. However, for AC2, sulfonic acid modification resulted in a small increase in pHpzc value from 2.53 to 2.90. Similarly, in a dye adsorption study by Goswami and Phukan [30], the pHpzc values were reported as 5.18 for activated carbon (MTLAC) and 2.4 for sulfonic acid-modified activated carbon (MTLAC-SA).

3.5 DLS Analyses

Based on the DLS histograms, the changes in particle size distributions of original and modified adsorbents were determined using the weight average calculation method. Particle size analysis graphs of original and modified AC1 and AC2 adsorbents are presented in Figure 4. The x-axis in the graphs represents the particle size diameter in nm, and the y-axis indicates the percentage of particles by number. Upon examining the DLS histogram of AC1 sample, it is observed to have a wide particle distribution ranging from 190.1 nm to 1718 nm. According to the weight average calculation method, the majority of AC1 carbon is sized at 377.52 nm. After nitric acid modification, the particle size distribution of AC1N adsorbent reduced, with an average size of 241.23 nm. The AC1S sample has an average particle size distribution calculated as 1419.44 nm. This suggests that the modification significantly increased particle size for AC1S carbon. Similarly, the average size distribution of AC2 adsorbent is 685.37 nm, whereas after nitric acid modification, AC2N adsorbent showed a significant decrease with an average size distribution of 259.66 nm. However, as compared to AC1S, the average particle size distribution of the AC2S adsorbent decreased after sulfonic acid alteration, measuring 428.42 nm.

Particle size analysis graphs of original and modified AC3 and AC4 adsorbents are presented in Figure 5. The average particle size distributions of AC3 and AC4 adsorbents are calculated as 939.94 nm and 313.32 nm, respectively. These results demonstrate that nitric acid modification led to a reduction in the average particle size distribution of both adsorbents. The values for AC3N and AC4N were found to be 279.04 and 252.81 nm, respectively. The originally calculated particle size distribution for AC3 at 939.94 nm increased to 992.81 nm in AC3S sample due to the effect of sulfonic acid modification. Additionally, approximately 70% of AC3S particle sizes fall within the range of 825-1106 nm. AC4S sample also showed a similar increase of 34%, calculated as 417.64 nm. Sulfonic acid modification had a positive influence on particle size distribution, whereas nitric acid modification often had a negative effect.

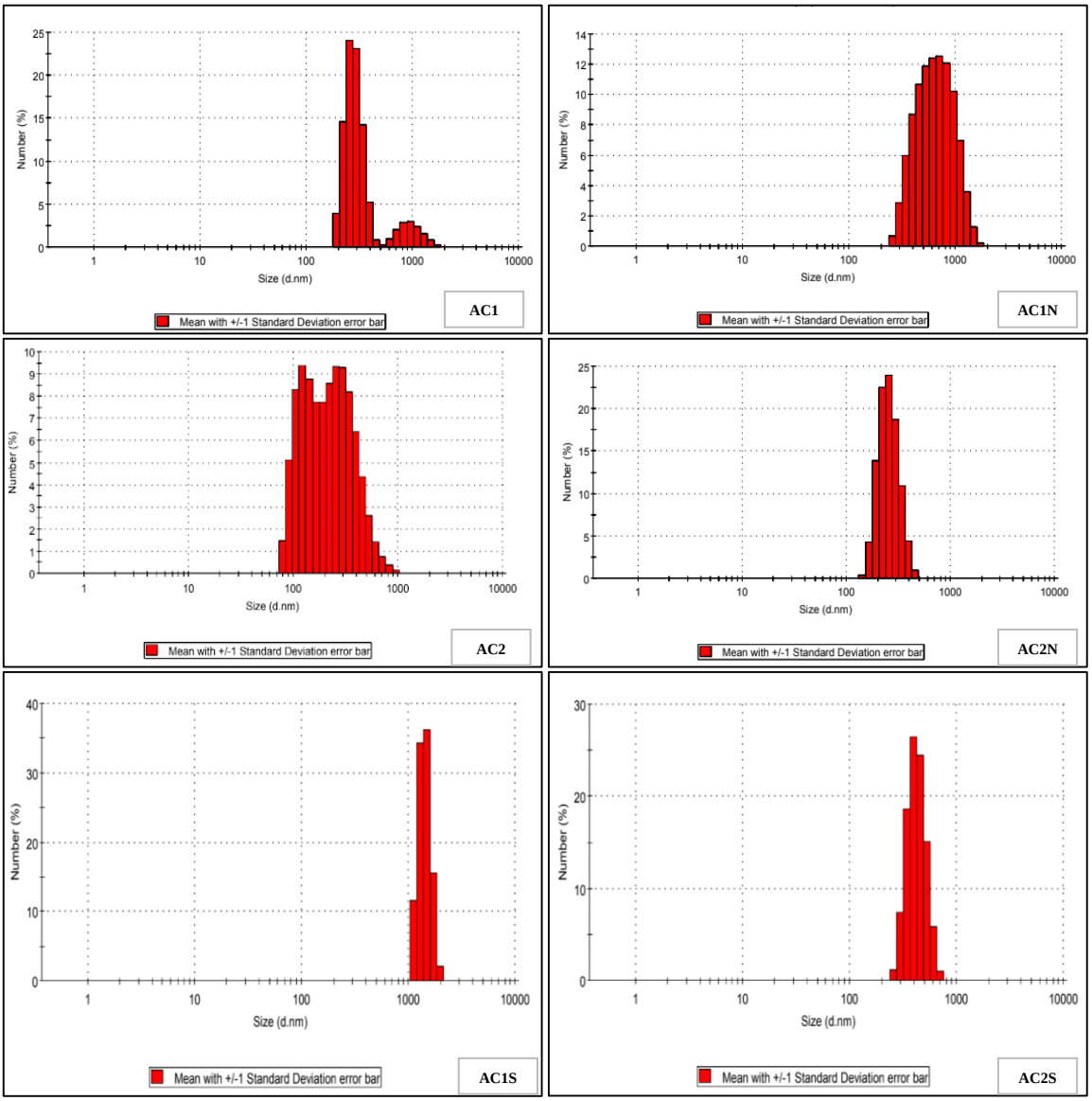

Figure 4. Particle Size Analysis Graphs of Original and Modified AC1 and AC2 Activated Carbons

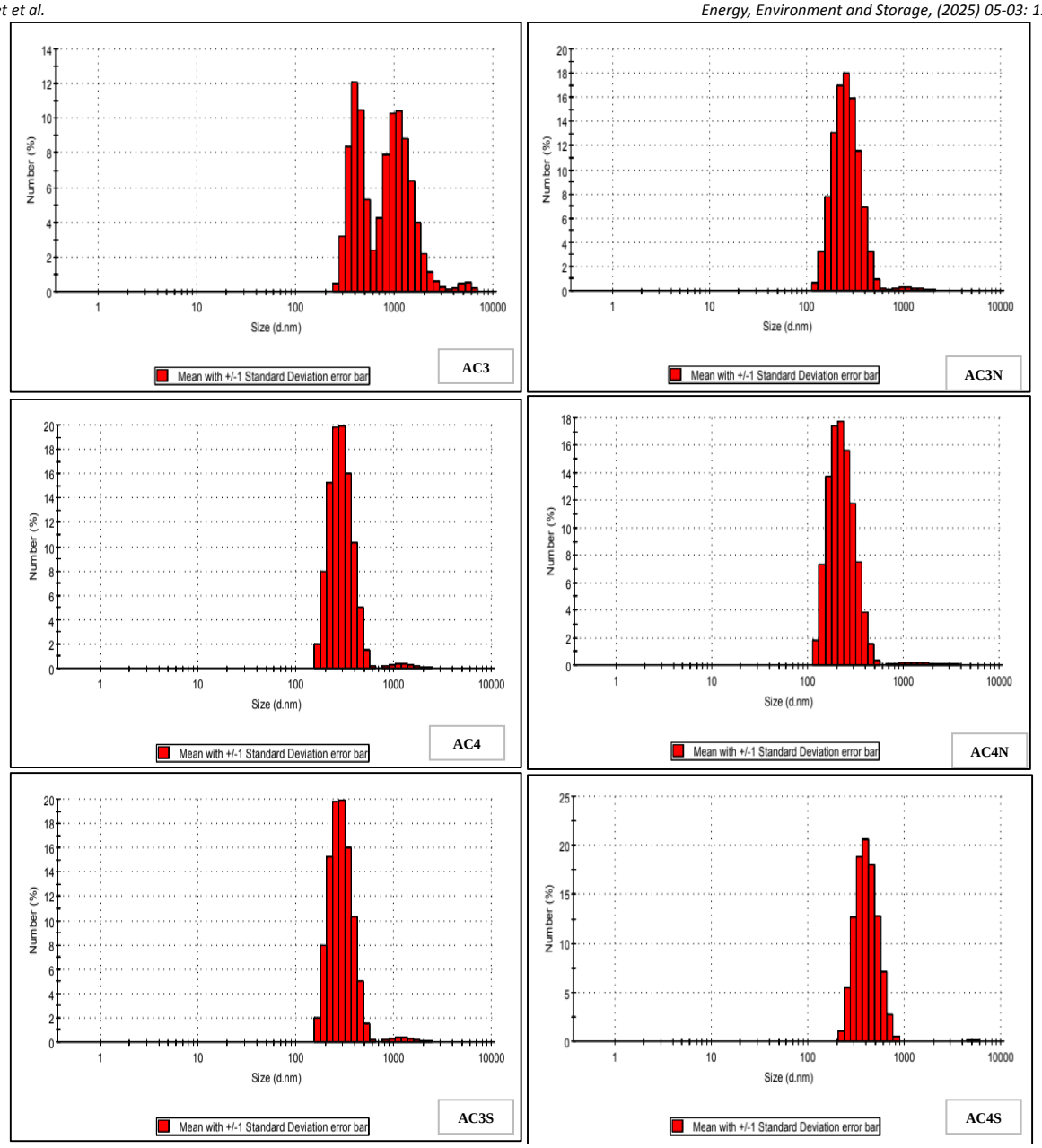

Figure 5. Particle Size Analysis Graphs of Original and Modified AC3 and AC4 Activated Carbons

4. CONCLUSIONS

In the Altinapa Dam Watershed, Activated carbons specific surface area and active sites, two crucial characteristics that significantly impact its adsorption capacity, may be adjusted through the use of chemical modification techniques. The current investigation evaluated and conducted characterization assessments on commercial powdered AC, nitric acid, chlorosulfonic acid, and double chemical modification. The key points are summarized below:

- Scanning Electron Microscopy (SEM) analysis demonstrated that nitric acid modification resulted in a smoother, cleaner, and more uniform surface morphology, whereas chlorosulfonic acid treatment did not induce significant morphological alterations.
- Fourier-transform infrared spectroscopy (FTIR) revealed the formation of oxygen-containing functional groups such as carboxyl, carbonyl, and quinone upon nitric acid modification. A new peak at 1993.6 cm^{-1} observed in the AC4S sample confirmed the presence of sulfonic groups (S=O and SO_3 H), indicating successful sulfonation via chlorosulfonic acid.
- A substantial increase in surface area was achieved with nitric acid treatment, with the highest enhancement (200%) observed in AC4N. A comparable increase was also noted in AC4S, indicating the effectiveness of both acid treatments in enhancing porosity.
- Double acid modification had a detrimental effect on the porous structure, causing surface area reductions of 39% and 76% in AC1 and AC2, respectively. This decrease is attributed to micropore wall degradation or pore blockage due to the formation of surface oxygenated groups.
- All acid-modified samples exhibited a decrease in pH_{PZC} values, reflecting an increase in surface acidity. Surface acid group concentrations increased up to 0.97 meq/g following nitric acid treatment.
- Chlorosulfonic acid modification significantly broadened the particle size distribution, potentially affecting the adsorptive behavior.
- Overall, the findings suggest that nitric acid and chlorosulfonic acid surface modifications are effective techniques for enhancing the physicochemical properties of activated carbon. When choosing a modification method for adsorption applications, the unique properties of the target pollutants should be taken into consideration.

Acknowledgments

This study was supported by the Scientific and Technological Research Council of Turkey (Project No: 118Y402).

REFERENCES

[1] T. Rasheed, K. Rizwan, M. Bilal, F. Sher and H. M. Iqbal. Tailored functional materials as robust candidates to mitigate pesticides in aqueous matrices—a review. Chemosphere, 282, 131056, 2021.

[2] M. Ponnuchamy, A. Kapoor, P. Senthil Kumar, D. V. N. Vo, A. Balakrishnan, M. Mariam Jacob and P. Sivaraman. Sustainable adsorbents for the removal of pesticides from water: a review. Environmental Chemistry Letters, 19, 2425–2463, 2021.

[3] V. B. Lunardi, F. E. Soetaredjo, K. Foe, J. N. Putro, I. G. Wenten, W. Irawaty, ... and S. Ismadji. Pesticide elimination through adsorption by metal-organic framework and their modified forms. Environmental Nanotechnology, Monitoring & Management, 17, 100638, 2022.

[4] I. A. Saleh, N. Zouari and M. A. Al-Ghouti. Removal of pesticides from water and wastewater: Chemical, physical and biological treatment approaches. Environmental Technology & Innovation, 19, 101026, 2020.

[5] T. M. Alslaibi, I. Abustan, M. A. Ahmad and A. A. Foul. A review: production of activated carbon from agricultural byproducts via conventional and microwave heating. Journal of Chemical Technology & Biotechnology, 88(7), 1183–1190, 2013.

[6] H. A. Ahsaine, Z. Anfar, M. Zbair, M. Ezahri and N. El Alem. Adsorptive removal of methylene blue and crystal violet onto micro-mesoporous Zr_3 O/activated carbon composite: a joint experimental and statistical modeling considerations. Journal of Chemistry, 2018, Article ID.

[7] Z. Anfar, H. A. Ait Ahsaine, M. Zbair, A. Amedlous, A. Ait El Fakir, A. Jada and N. El Alem. Recent trends on numerical investigations of response surface methodology for pollutants adsorption onto activated carbon materials: A review. Critical Reviews in Environmental Science and Technology, 50(10), 1043–1084, 2020.

[8] P. Chingombe, B. Saha and R. J. Wakeman. Surface modification and characterisation of a coal-based activated carbon. Carbon, 43(15), 3132–3143, 2005.

[9] M. S. Shafeeyan, W. M. A. W. Daud, A. Houshmand and A. Shamiri. A review on surface modification of activated carbon for carbon dioxide adsorption. Journal of Analytical and Applied Pyrolysis, 89(2), 143–151, 2010.

[10] J. Rivera-Utrilla, M. Sánchez-Polo, V. Gómez-Serrano, P. M. Álvarez, M. C. M. Alvim-Ferraz and J. M. Dias. Activated carbon modifications to enhance its water treatment applications: An overview. Journal of Hazardous Materials, 187(1–3), 1–23, 2011.

[11] X. Xu, B. Gao, X. Tan, M. Zhang and Q. Yue. Characterization and mechanisms of metal cations removal by a novel magnetic $MnFe_2$ O_4 /biochar composite. Bioresource Technology, 276, 247–253, 2019.

[12] M. Mariana, A. K. HPS, E. M. Mistar, E. B. Yahya, T. Alfatah, M. Danish and M. Amayreh. Recent advances in activated carbon modification techniques for enhanced heavy metal adsorption. Journal of Water Process Engineering, 43, 102221, 2021.

[13] E. Wolak and A. Orzechowska-Zięba. Change of the surface and structure of activated carbon as a result of HNO_3 modification. Adsorption, 30(2), 121–128, 2024.

[14] X. Lu, J. Jiang, K. Sun, X. Xie and Y. Hu. Surface modification, characterization and adsorptive properties of a coconut activated carbon. Applied Surface Science, 258(20), 8247–8252, 2012.

[15] Y. Wang, C. Lin, X. Liu, W. Ren, X. Huang, M. He and W. Ouyang. Efficient removal of acetochlor pesticide from water using magnetic activated carbon: Adsorption performance, mechanism, and regeneration exploration. Science of the Total Environment, 778, 146353, 2021.

[16] L. Azeez, S. A. Adebisi, A. L. Adejumo, H. K. Busari, H. K. Aremu, O. A. Olabode and O. Awolola. Adsorptive properties of rod-shaped silver nanoparticles-functionalized biogenic hydroxyapatite for remediating methylene blue and congo red. Inorganic Chemistry Communications, 142, 109655, 2022.

[17] C. J. Okorie, T. Ojeyemi, A. Egbemhenghe, M. Q. Ali, E. C. Emenike, K. O. Iwuozor and A. G. Adeniyi. Modification of activated carbon for enhanced treatment of per- and polyfluoroalkyl substances: A focused review. Remediation Journal, 34(2), e21777, 2024.

[18] A. N. A. El-Hendawy. Influence of HNO_3 oxidation on the structure and adsorptive properties of corncob-based activated carbon. Carbon, 41(4), 713–722, 2003.

[19] L. Tang, S. Zhang, L. Li and J. Chen. Preparation of modified activated carbon from corn stalk and adsorption mechanism study for nitrate removal. Ecotoxicology and Environmental Safety, 126, 10–17, 2016.

[20] Y. Gökçe and Z. Aktaş. Nitric acid modification of activated carbon produced from waste tea and adsorption of methylene blue and phenol. Applied Surface Science, 313, 352–359, 2014.

[21] J. Valentin-Reyes, R. B. García-Reyes, A. García-González, E. Soto-Regalado and F. Cerino-Córdova. Adsorption mechanisms of hexavalent chromium from aqueous solutions on modified activated carbons. Journal of Environmental Management, 236, 815–822, 2019.

[22] X. Li, J. Qiu, Y. Hu, X. Ren, L. He, N. Zhao, ... and X. Zhao. Characterization and comparison of walnut shells-based activated carbons and their adsorptive properties. Adsorption Science & Technology, 38(9–10), 450–463, 2020.

[23] C. Coelho, A. S. Oliveira, M. F. R. Pereira and O. C. Nunes. The influence of activated carbon surface properties on the adsorption of the herbicide molinate and the bio-regeneration of the adsorbent. Journal of Hazardous Materials, 138(2), 343–349, 2006.

[24] Q. Li, J. Sun, T. Ren, L. Guo, Z. Yang, Q. Yang and H. Chen. Adsorption mechanism of 2,4-dichlorophenoxyacetic acid onto nitric-acid-modified activated carbon fiber. Environmental Technology, 39(7), 895–906, 2018.

[25] P. Su, J. Zhang, J. Tang and C. Zhang. Preparation of nitric acid modified powder activated carbon to remove trace amount of Ni(II) in aqueous solution. Water Science and Technology, 80(1), 86–97, 2019.

[26] S. X. Liu, X. Chen, X. Y. Chen, Z. F. Liu and H. L. Wang. Activated carbon with excellent chromium (VI) adsorption performance prepared by acid–base surface modification. Journal of Hazardous Materials, 141(1), 315–319, 2007.

[27] W. S. Chen, Y. C. Chen and C. H. Lee. Modified activated carbon for copper ion removal from aqueous solution. Processes, 10(1), 150, 2022.

[28] C. Liang, Z. Li and G. Zeng. Recent advances in activated carbon modified for better hydrophobic organic contaminant adsorption: A review. Environmental Science & Technology, 44(21), 8267–8271, 2010.

[29] J. J. Alvear-Daza, G. A. Pasquale, J. A. Rengifo-Herrera, G. P. Romanelli and L. R. Pizzio. Mesoporous activated carbon from sunflower shells modified with sulfonic acid groups as solid acid catalyst for itaconic acid esterification. Catalysis Today, 372, 51–58, 2021.

[30] M. Goswami and P. Phukan. Enhanced adsorption of cationic dyes using sulfonic acid modified activated carbon. Journal of Environmental Chemical Engineering, 5(4), 3508–3517, 2017.

[31] N. Eibisch, R. Schroll, R. Fuß, R. Mikutta, M. Helfrich and H. Flessa. Pyrochars and hydrochars differently alter the sorption of the herbicide isoproturon in an agricultural soil. Chemosphere, 119, 155–162, 2015.

[32] M. W. Akhtar, N. M. Gabol, M. A. Memon, A. Shaikh, R. Shahbaz and M. Y. Khan. Synthesis and characterization of adsorbent biochar/$MnFe_2O_4$ composite from agricultural residue for wastewater treatment. ECS Journal of Solid State Science and Technology, 10(5), 057006, 2021.

[33] D. H. Nguyen, H. N. Tran, H. P. Chao and C. C. Lin. Preparation and characterization of activated carbon from banana peels and removal of heavy metal ions from aqueous solutions. Water Science and Technology, 76(9), 2369–2380, 2017.

[34] S. Bose, P. S. Kumar, G. Rangasamy, G. Prasannamedha and S. Kanmani. A review on the applicability of adsorption techniques for remediation of recalcitrant pesticides. Chemosphere, 313, 137481, 2023.

[35] A. Guha, W. J. Lu, T. A. Zawodzinski and D. A. Schiraldi. Surface-modified carbons as platinum catalyst support for PEM fuel cells. Carbon, 45, 1506–1517, 2007.

[36] S. A. Dastgheib, T. Karanfil and W. Cheng. Tailoring activated carbons for enhanced removal of natural organic matter from natural waters. Carbon, 42(3), 547–557, 2004.

[37] X. Ge, X. Ma, Z. Wu, X. Xiao and Y. Yan. Modification of coal-based activated carbon with nitric acid using microwave radiation for adsorption of phenanthrene and naphthalene. Research on Chemical Intermediates, 41, 7327–7347, 2015.

[38] N. Bader, S. Souissi-Najar and A. Ouederni. A controlled nitric acid oxidation of an olive stones-based activated carbon: effect of oxidation time. Lignocellulose Journal, 3(1), 22–36, 2014.

[39] H. T. Ma, V. T. T. Ho, N. B. Pham, L. G. Bach and D. T. Phan. The comparison of surface modification

methods of the heavy metals adsorption of activated carbon from rice husk. Applied Mechanics and Materials, 876, 91–96, 2018.

[40] M. F. R. Pereira, S. F. Soares, J. J. Órfão and J. L. Figueiredo. Adsorption of dyes on activated carbons: influence of surface chemical groups. Carbon, 41(4), 811–821, 2003.

[41] J. P. Chen and S. Wu. Acid/base-treated activated carbons: characterization of functional groups and metal adsorptive properties. Langmuir, 20(6), 2233–2242, 2004.

[42] S. Asaoka and T. Yamamoto. Characteristics of phosphate adsorption onto granulated coal ash in seawater. Marine Pollution Bulletin, 60(8), 1188–1192, 2010.

[43] İ. Demiral, C. Samdan and H. Demiral. Enrichment of the surface functional groups of activated carbon by modification method. Surfaces and Interfaces, 22, 100873, 2021.

[44] M. Z. Yavuzarslan. Nar kabuğundan elde edilen aktif karbon ile meyve suyundan pestisit adsorpsiyonu (Master's thesis, Fen Bilimleri Enstitüsü), 2019.

[45] G. Huang, J. X. Shi and T. A. Langrish. Removal of Cr (VI) from aqueous solution using activated carbon modified with nitric acid. Chemical Engineering Journal, 152(2–3), 434–439, 2009.

[46] A. Zahoor, M. Christy, Y. J. Hwang, Y. R. Lim, P. Kim and K. S. Nahm. Improved electrocatalytic activity of carbon materials by nitrogen doping. Applied Catalysis B: Environmental, 147, 633–641, 2014.

[47] M. S. Islam, B. C. Ang, S. Gharehkhani and A. B. M. Afifi. Adsorption capability of activated carbon synthesized from coconut shell. Carbon Letters, 20, 1–9, 2016.

[48] I. A. Schepetkin, A. I. Khlebnikov, S. Y. Ah, S. B. Woo, C. S. Jeong, O. N. Klubachuk and B. S. Kwon. Characterization and biological activities of humic substances from mumie. Journal of Agricultural and Food Chemistry, 51(18), 5245–5254, 2003.

[49] H. ShamsiJazeyi and T. Kaghazchi. Investigation of nitric acid treatment of activated carbon for enhanced aqueous mercury removal. Journal of Industrial and Engineering Chemistry, 16(5), 852–858, 2010.

[50] J. W. Shim, S. J. Park and S. K. Ryu. Effect of modification with HNO_3 and NaOH on metal adsorption by pitch-based activated carbon fibers. Carbon, 39(11), 1635–1642, 2001.

[51] X. Hu, H. Zhang and Z. Sun. Adsorption of low concentration ceftazidime from aqueous solutions using impregnated activated carbon promoted by iron, copper and aluminum. Applied Surface Science, 392, 332–341, 2017.

[52] Ç. Öter and Ö. S. Zorer. Adsorption behaviours of Th(IV) and U(VI) using nitric acid (HNO_3) modified activated carbon: equilibrium, thermodynamic and kinetic studies. International Journal of Environmental Analytical Chemistry, 101(14), 1950–1965, 2021.

[53] A. IkhtiarBakti and P. L. Gareso. Characterization of active carbon prepared from coconuts shells using FTIR, XRD and SEM techniques. Jurnal Ilmiah Pendidikan Fisika Al-Biruni, 7, 33–39, 2018.

[54] Q. Huang, A. S. Schafranski, M. J. Hazlett, Y. Xiao and J. M. Hill. Nitric acid functionalization of petroleum coke to access inherent sulfur. Catalysts, 10(2), 259, 2020.

[55] M. Kamari, S. Shafiee, F. Salimi and C. Karami. Comparison of modified boehmite nanoplatelets and nanowires for dye removal from aqueous solution. Desalination and Water Treatment, 161, 304–314, 2019.

[56] O. Adam, M. Bitschené, G. Torri, F. De Giorgi, P. M. Badot and G. Crini. Studies on adsorption of propiconazole on modified carbons. Separation and Purification Technology, 46(1–2), 11–18, 2005.

[57] S. Yao, J. Zhang, D. Shen, R. Xiao, S. Gu, M. Zhao and J. Liang. Removal of Pb (II) from water by the activated carbon modified by nitric acid under microwave heating. Journal of Colloid and Interface Science, 463, 118–127, 2016.

[58] A. Khelifi, M. C. Almazán-Almazán, M. Pérez-Mendoza, M. Domingo-García, F. J. López-Domingo, L. Temdrara and A. Addoun. Influence of nitric acid concentration on the characteristics of active carbons obtained from a mineral coal. Fuel Processing Technology, 91(10), 1338–1344, 2010.

[59] W. Huang, Y. Zhang, S. Bao, R. Cruz and S. Song. Desalination by capacitive deionization process using nitric acid-modified activated carbon as the electrodes. Desalination, 340, 67–72, 2014.

[60] Yu, C., Fan, X., Yu, L., Bandosz, T. J., Zhao, Z., & Qiu, J. (2013). Adsorptive removal of thiophenic compounds from oils by activated carbon modified with concentrated nitric acid. Energy & Fuels, 27(3), 1499-1505.

[61] E. Partlan. Superfine Powdered Activated Carbon (S-PAC) Coupled with Microfiltration for the Removal of Trace Organics in Drinking Water Treatment (Doctoral dissertation, Clemson University), 2017.

[62] X. Meng, Y. Wan, K. Feng, H. Kong and T. Liu. Preparation and characteristics of three sorbents from wood chips screening reject (WCSR) modified by nitric acid, phosphoric acid, or sodium hydroxide. BioResources, 14(1), 2216–2228, 2019.

[63] Z. Jiang, Y. Liu, X. Sun, F. Tian, F. Sun, C. Liang and C. Li. Activated carbons chemically modified by concentrated H_2 SO_4 for the adsorption of the pollutants from wastewater and the dibenzothiophene from fuel oils. Langmuir, 19(3), 731–736, 2003.

[64] A. E. Vasu. Surface modification of activated carbon for enhancement of nickel (II) adsorption. Journal of Chemistry, 5(4), 814–819, 2008.

[65] A. Dąbrowski, P. Podkościelny, Z. Hubicki and M. Barczak. Adsorption of phenolic compounds by activated carbon—a critical review. Chemosphere, 58(8), 1049–1070, 2005.

Energy, Environment and Storage

Journal Homepage: www.enenstrg.com

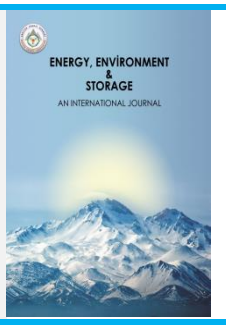

Investigation of the Experimental Performance of Different Savonius Wind Turbines in an Open Wind Tunnel

Burcu Hasaltın[1*], Sayra Bengü Yılmaz[2], Mahmut Burak Akkuş[3]

[1*]*Erciyes University, Department of Mechanical Engineering, Kayseri, Türkiye, ORCID: 0009-0005-4927-543X*

[2]*Erciyes University, Department of Mechanical Engineering, , Kayseri, Türkiye ,*

[3]*Erciyes University, Department of Mechanical Engineering, , Kayseri, Türkiye ORCID: 0000-0002-4561-7093*

Abstract. This study presents a comprehensive experimental investigation into the aerodynamic performance of six Savonius wind turbine blade profiles with distinct geometries, tested systematically in an open wind tunnel facility. The motivation behind this research stems from the need to optimize small-scale wind turbines for efficient operation under low-wind-speed conditions, which are commonly encountered in urban and decentralized energy applications. To achieve this, six different blade configurations—including classical semi-cylindrical, helical, and hybrid/optimized models—were designed, fabricated, and subjected to rigorous testing. Each prototype shared identical rotor dimensions in terms of diameter and blade height, ensuring that observed differences in performance could be attributed solely to blade geometry rather than scaling effects. The experimental campaign was conducted under controlled wind conditions, with a constant free-stream wind speed, allowing for repeatability and reliability of results. Key aerodynamic performance parameters, including torque generation, rotational speed, tip speed ratio, and power coefficient, were systematically measured and analyzed. The findings clearly demonstrate that blade geometry plays a critical role in determining the overall performance of Savonius turbines. The comparative results highlight the inherent trade-offs between achieving strong initial torque and maximizing aerodynamic efficiency. These insights are particularly valuable for guiding future design improvements aimed at small-scale renewable energy systems. By demonstrating the advantages of hybrid blade designs, this study contributes to the ongoing development of compact, efficient, and reliable wind energy solutions suitable for applications in low-wind-speed regions, such as urban rooftops, agricultural fields, and off-grid installations. Ultimately, this research provides not only an experimental benchmark for Savonius turbine geometries but also practical design guidance that can inform engineers and developers in the renewable energy sector. The results serve as a foundation for further optimization studies and future innovations in the design of vertical-axis wind turbines.

Keywords: Savonius Wind Turbine Rrenewable Energy, Aerodynamic Performance.

Article History: Received:10 September 2025; Revised: 22 September 2025; Accepted :03. October 2025 Availableonline: 03 October 2025
Doi: https://doi.org/10.52924/RENW7010

1. INTRODUCTION

The global demand for clean and sustainable energy is increasing rapidly due to climate change concerns and the depletion of fossil fuel resources. Wind energy, as a renewable and environmentally friendly option, plays a critical role in achieving carbon-neutral energy goals.
Wind energy has become one of the most prominent and rapidly growing renewable energy sources due to increasing energy demand and environmental concerns. Among the various wind turbine types, Savonius wind turbines are widely recognized for their simplicity,low-cost construction, and ability to operate at low wind speeds. These characteristics make them particularly suitable for small-scale and decentralized energy generation applications. There are very application and manuscript in literature [1-20].

The performance of a Savonius turbine is strongly influenced by blade geometry, including the shape, number of blades, and tip configuration. While the classical semi-cylindrical design is known for its high starting torque, modifications such as helical and spiral-tipped blades have been proposed to improve aerodynamic efficiency and rotational speed. Despite several studies on Savonius turbines, comparative experimental investigations of different blade geometries under controlled wind tunnel conditions remain limited.

*hasaltinburcu@gmail.com

This study aims to fill this gap by experimentally evaluating six different Savonius blade profiles in an open wind tunnel. The research focuses on key performance parameters including torque, rotational speed, and aerodynamic efficiency. This study provides a detailed experimental evaluation of six different Savonius turbine geometries under the same laboratory conditions, offering new insights into the optimization potential of blade configurations for efficient small-scale wind energy harvesting.

The results are expected to provide valuable insights for the design and optimization of small-scale wind energy systems, particularly in low-wind-speed regions, and to guide future developments in efficient and compact renewable energy solutions. Due to their ability to operate under low wind speeds, Savonius turbines are especially suitable for small-scale power generation in urban environments, agricultural irrigation, and decentralized off-grid applications.

2. MATERIALS AND METHODS

2.1 *Format*

The experimental study was conducted using six different Savonius wind turbine blade models, all having the same rotor diameter and blade length. The tests were performed in an open wind tunnel laboratory setup located at the Motor Laboratory of Erciyes University, Kayseri, Turkey. The wind tunnel used in this study is equipped with six fans, which can be operated manually to generate the desired wind flow. The fan motors were operated individually in sequence to prevent overloading and potential power interruptions. An emergency stop button was also available to ensure safety in case of unexpected situations.

Fig. 1. The Wind Tunnel Used in The Experiment-1

During the experiments, a wind speed of 5.7 m/s was maintained, and the ambient temperature was 24.0 °C. The wind speed was measured using an anemometer, and the torque generated by the turbine was recorded with a torque meter. The turbine models were placed on a vertical axis configuration, and all measurements were conducted under controlled conditions to ensure repeatability and accuracy.

This experimental setup allowed for a detailed evaluation of the aerodynamic performance of the different Savonius blade geometries under consistent laboratory conditions.

Fig. 2. The Wind Tunnel Used in The Experiment-2

2.2 Turbine Specifications and Operating Conditions

The Savonius wind turbine prototypes used in this study had a rotor diameter of 150 mm and a blade height of 200 mm. All six blade models shared these dimensions to ensure consistency in the comparative analysis. During the experiments, a wind speed of 5.7 m/s was maintained in the open wind tunnel.

Fig. 3. The Anemometer

Based on the observed operating conditions and typical tip speed ratios for Savonius turbines (approximately 0.4), the rotational speed of the turbine was estimated to be around 290 revolutions per minute (RPM). These specifications and conditions provided a controlled environment to accurately evaluate the aerodynamic performance of each blade geometry.

Test Section:

Dimensions: 0.5 m × 0.5 m cross-section, 2 m length .
The section houses the wind turbine models and instrumentation.
Fan System: Six variable-speed axial fans are installed at the inlet to generate controlled airflow.

Fans can be operated manually to adjust wind speed in the range of 2–10 m/s

Instrumentation Ports: Equipped with access points for voltage sensors, torque sensors, and anemometers.

Rotor Diameter: 150 mm
Blade Height: 200 mm

Number of Models Tested: 6 (Models 1–6, including classical, helical, and hybrid/optimized configurations)

Mounting System:

Turbines are mounted on a low-friction vertical shaft connected to a torque sensor.

Bearings are used to reduce mechanical losses and ensure free rotation.

Measurement Devices

Voltage Measurement: Digital voltmeter (accuracy ±0.01 V) connected to the rotor output.

Torque Measurement: Torque transducer (accuracy ±0.02 Nm) installed on the rotor shaft.

Data Acquisition: All sensors are connected to a DAQ system for continuous recording.

Experimental Procedure

Turbine model is mounted and aligned vertically.
Fans are operated to reach the desired wind speed.

Voltage and torque readings are recorded for 3–5 repetitions per condition.

Environmental parameters such as temperature and air density are noted for correction.

2.3 Experimental Savonius Wind Turbine Models

In this study, a total of six different Savonius wind turbine models were subjected to performance analysis in an open wind tunnel. The models were selected based on their distinct geometric features and blade designs. During the experiments, the models were designated as Model 1 through Model 6, and the aerodynamic behavior of each was examined. Model 1 and Model 2: These were produced with a classical half-cylinder blade design, representing the fundamental Savonius turbine geometry. Similarly, the double-step Savonius rotor proposed by Menet (2004) and the curtain arrangements investigated by Altan & Atilgan (2008) present different approaches to improving the efficiency of classical designs. [11,12]

Fig. 4. Model 1 - The experimental view of the classical, blade models in front of the wind turbine

Fig. 5. Model 2- The experimental view of the classical, blade models in front of the wind turbine

Model 3 and Model 4: These featured helical (screw-shaped) blade designs, expected to exhibit differences in torque and rotational speed compared to the classical models.

These findings are also consistent with the study conducted by Saha et al. (2008), which indicated that helical blades guide the flow more smoothly and improve load distribution. [10]

Fig. 6. Model 3 - The experimental view of the helical, models in front of the wind turbine.

Fig. 7. Model 4 - The experimental view of the helical, blade models in front of the wind turbine

Model 5 and Model 6: These were modified hybrid models, offering potential for optimization in terms of both torque and aerodynamic efficiency.

These results support the performance improvements achieved with new blade geometries by Kacprzak et al. (2013) and the aerodynamic enhancements identified in Darrieus–Savonius hybrid turbines by Islam et al. [9,13].

The experimental appearances of the models are presented. The dimensions of each model, blade widths, and placement details within the wind tunnel were tabulated to ensure the reproducibility of the experiments. The performance data obtained from these models are discussed in detail in the subsequent sections.

Fig. 8. Model 5 - The experimental view of the hybrid/optimized blade models in front of the wind turbine

Fig. 9. Model 6 - The experimental view of the hybrid/optimized blade models in front of the wind turbine

3. FIGURES AND TABLES

3.1 Figures and Tables

The experimental results for the six Savonius wind turbine models are presented in Figures and Tables. The

turbines were grouped as Model 1–2, Model 3–4, and Model 5–6 according to their blade geometry.

Table 1 Voltage and Torque Measurements for Savonius Wind Turbine Model 1 - Model 2

Cv	Model 1-Torque (Nm)	Model 2-Torque (Nm)
0,1	0,0075	0,0080
0,5	0,0073	0,0078
1	0,0069	0,0075
1,5	0,0063	0,0071
2	0,0057	0,0066
2,5	0,0049	0,0058
3	0,0040	0,0055
3,5	0,0032	0,0049
4	0,0024	0,0043
4,5	-	0,0038
5	-	0,0032
5,5	-	0,0025
6	-	0,0019

Each table provides key performance parameters, including torque (Nm), rotational speed (RPM and rad/s), tip speed ratio (TSR), and power coefficient (Cp) under a constant wind speed of 5.7 m/s.

Table 2 Voltage and Torque Measurements for Savonius Wind Turbine Model 3 – Model 4

Cv	Model 3-Torque (Nm)	Model 3-Torque (Nm)
0,1	0,0054	0,0050
0,5	0,0051	0,0047
1	0,0047	0,0046
1,5	0,0041	0,0043
2	0,0037	0,0039
2,5	0,0031	0,0036
3	0,0026	0,0032
3,5	0,0020	0,0028
4	-	0,0022

Figures illustrate the variation of torque, TSR, and Cp with respect to different blade models. These visualizations highlight the aerodynamic performance differences among the six blade geometries, providing insights into the efficiency and rotational characteristics of each configuration.

Table 3 Voltage and Torque Measurements for Savonius Wind Turbine Model 5 - Model 6

Cv	Model 5-Torque (Nm)	Model 6-Torque (Nm)
0,1	0,0058	0,0070
0,5	0,0054	0,0066
1	0,0049	0,0061
1,5	0,0045	0,0056
2	0,0040	0,0051
2,5	0,0034	0,0047
3	0,0039	0,0043
3,5	0,0022	0,0038
4		0,0034
4,5		0,0030
5		0,0026
5,5		0,0022

Table 1, Table 2, and Table 3 correspond to the experimental data of Model 1–2, Model 3–4, and Model 5–6, respectively, summarizing the measured parameters for easy comparison. The presented data serve as the basis for evaluating the aerodynamic efficiency and operational behavior of the different Savonius turbine designs.

4. EQUATION

In this study, the aerodynamic performance of Savonius wind turbines was evaluated using the following equations:

Tip Speed Ratio (TSR) – the ratio of the tangential speed of the rotor tip to the free-stream wind speed:,

$$\mathrm{TSR} = \frac{\omega R}{V} \quad (1)$$

Where:
ω = rotational speed of the rotor (rad/s)
R = rotor radius (m)

V = wind speed (m/s)

Rotor Rotational Speed (RPM) – conversion from angular velocity to revolutions per minute:

$$\mathrm{RPM} = \omega \cdot \frac{60}{2\pi} \quad (2)$$

Power Coefficient (Cp) – The power coefficient represents the efficiency of the wind turbine in converting the wind's kinetic energy into mechanical power:

$$C_p = \frac{P}{\frac{1}{2}\rho A V^3} \quad (3)$$

where:

ρ = air density [kg/m³],
A=D·H rotor frontal area [m²],
D = rotor diameter [m],
H = rotor height [m],
V = wind speed [m/s].

Torque Coefficient (CT) – The torque coefficient is a non-dimensional parameter representing the torque relative to the wind dynamic pressure and rotor area:

$$C_T = \frac{T}{\frac{1}{2}\rho A R V^2} \quad (4)$$

where all symbols are as defined above.

4.1 Correction Factors

Air Density, Sensor Calibration and Mechanical Loss Factor

The turbine output power is directly proportional to air density:

$$P_{\text{corrected}} = P_{\text{measured}} \cdot \frac{\rho_{\text{ref}}}{\rho_{\text{actual}}} \quad (5)$$

where:
ρ_{ref}: Reference air density (1.225 kg/m³)
ρ_{actual} : Actual air density during the experiment

$$V_{\text{corrected}} = K_s \cdot V_{\text{measured}} \quad (6)$$

K_s: Sensor Calibration Factor

$$T_{\text{corrected}} = \frac{T_{\text{measured}}}{K_m} \quad (7)$$

K_m : Mechanical loss factor
To correct for bearing and shaft friction in torque measurements.

5. RESULTS

In this study, the aerodynamic performances of six Savonius wind turbine models with different geometric designs were compared through open wind tunnel experiments. All models were tested under constant wind speed (5.7 m/s), fixed rotor diameter (150 mm), and blade height (200 mm) conditions. The experimental findings were evaluated based on torque–Cv (moment coefficient) curves.

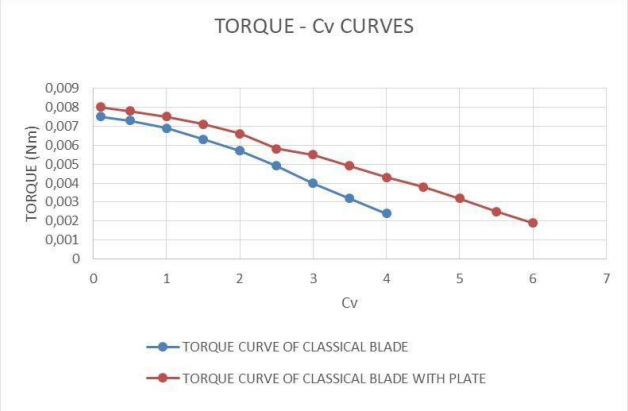

Fig. 10. Voltage Values and Torque Variations Model 1 and Model 2

In the graph comparing Model 1 and Model 2, it was observed that both designs produced similar torque at low Cv values, whereas Model 2 maintained higher torque values as Cv increased. This indicates that Model 2 managed flow separation more effectively and operated more efficiently under load. This trend is consistent with the pioneering study of Sheldahl and Klimas [1].

Fig. 11. Voltage Values and Torque Variation Model 3 and Model 4

Models 3 and 4 are turbines with helical (screw-shaped) blade geometries. The graphs show that both models exhibited similar behavior at low Cv values, whereas Model

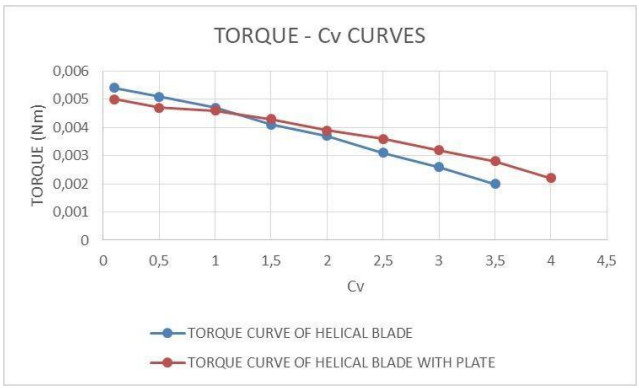

4 generated higher torque compared to Model 3 in the medium and high Cv regions. This result is supported by the fact that helical structures guide the flow more smoothly and improve load distribution on the blade surface.

The introduction of helical blade geometry in Models 3 and 4 resulted in smoother torque curves and reduced torque fluctuations. These outcomes agree with the results of Hosseini Rad et al. [4], who showed that helical Savonius turbines provide superior aerodynamic stability and improved performance over classical straight-blade designs. Similarly, Liu et al. [5] and Eftekhari et al. [8] confirmed that the helical configuration increases power output and efficiency due to better flow attachment along the blade surface.

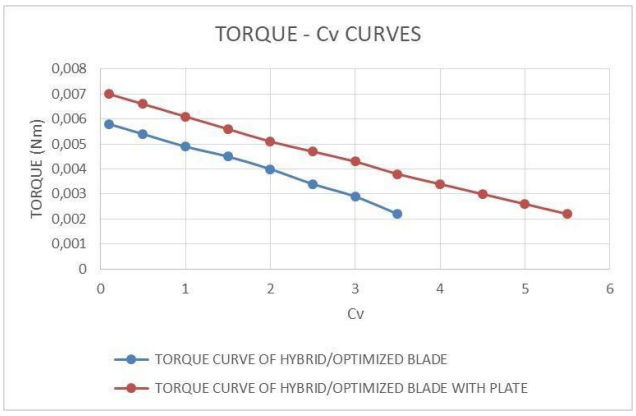

Fig. 12. Voltage Values and Torque Variations Model 5 and Model 6

Models 5 and 6 consist of hybrid designs. According to the obtained results, Model 6 provided higher torque values than Model 5 across all Cv ranges. This indicates that hybrid designs offer advantages in terms of aerodynamic efficiency compared to classical Savonius blades, and particularly that the design of Model 6 has optimization potential.

These findings align with the work of Ghafoorian et al. [3], who demonstrated that hybrid Darrieus–Savonius turbines benefit from combined self-starting capability and higher efficiency. In addition, the optimized hybrid blade geometries investigated by Ghosh et al. [6] and Bakırcı [7] reported similar improvements in torque performance and energy capture efficiency.

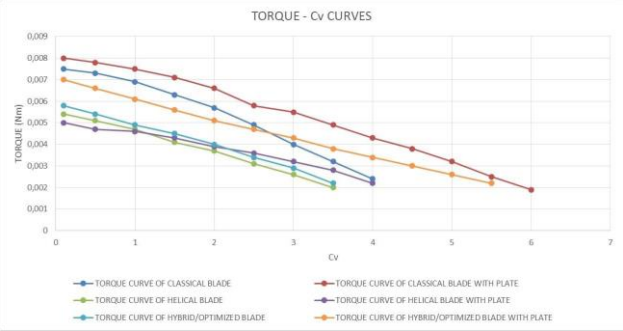

Fig. 13. Torque–Cv Curve Graph for All Tested Blade Models

Model 1 and Model 2: At the initial Cv ≈ 0, Model 1 produced approximately 0.0075 Nm of torque, while Model 2 generated 0.008 Nm. At Cv = 4, the torque of

Model 1 decreased to 0.0025 Nm, whereas Model 2 maintained a torque of 0.0045 Nm at the same point. This difference indicates that Model 2 can produce approximately 80% higher torque under high load conditions. [1,2]

Model 3 and Model 4: At the initial Cv ≈ 0, Model 3 produced 0.0055 Nm, and Model 4 generated 0.005 Nm of torque. At Cv = 3.5, the torque of Model 3 dropped to 0.002 Nm, while Model 4 maintained a torque of 0.0028 Nm. This demonstrates that Model 4 can generate approximately 40% higher torque than Model 3 at high Cv values. [3,4]

Model 5 and Model 6: At Cv = 0, Model 5 produced approximately 0.006 Nm, and Model 6 produced 0.007 Nm of torque. At Cv = 3, the torque of Model 5 was 0.0025 Nm, while Model 6 measured 0.0038 Nm. Under maximum load conditions, the torque values of Model 6 were found to be nearly 50% higher than those of Model 6 [5,6].

Summary of Comparative Findings:

Classical Designs (Models 1–2): Model 2 displayed higher and more stable torque than Model 1, emphasizing the impact of small geometric adjustments even within traditional designs.

Helical Designs (Models 3–4): Showed balanced performance, with Model 4 outperforming Model 3 under higher Cv values due to better flow control characteristics.

Hybrid/Optimized Designs (Models 5–6): Model 6 emerged as the most efficient among all tested models, maintaining superior torque output across all tested Cv values [7,8].

The increases in power coefficient (Cp) obtained by raising the aspect ratio reached higher levels compared to similar designs in the literature [20]. This indicates that our designs have improved aerodynamic efficiency and that the performance of Savonius turbines can be optimized.

The literature indicates that solar assisted HVAC systems can reduce building energy demand by 30–60%, depending on technology type (solar heating, solar cooling, or hybrid), location, and building design [2–5]. These systems also contribute to carbon mitigation and improved indoor comfort. However, challenges remain:

- Intermittency of solar resources limits system reliability without backup or storage,
- High initial investment costs hinder adoption in developing countries.
- System complexity requires advanced control strategies

2.5 Relevance for Afghanistan

Afghanistan presents strong opportunities for solar HVAC deployment because of high solar potential and seasonal demand for both heating and cooling. However, studies remain limited. The few available works [1,5] emphasize solar heating but lack detailed techno-economic assessments of year round HVAC integration. This underscores the need for simulation based studies that use high resolution hourly climate data to evaluate performance, reliability, and economic feasibility a gap directly addressed by the ongoing thesis research associated with this review.

6. Stirling Engines in CHP and CCHP Applications

The Stirling engine, invented in the early 19th century, is an external combustion engine operating on the Stirling thermodynamic cycle. Its ability to utilize diverse heat sources including biomass, natural gas, geothermal, and concentrated solar thermal energy makes it highly versatile for combined heat and power (CHP) and combined cooling, heating, and power (CCHP) applications. Compared to conventional internal combustion engines, Stirling engines offer several advantages, including high theoretical efficiency, low noise, long service life, and zero direct emissions when powered by renewable heat.

3.1 Stirling Engines in Combined Heat and Power (CHP)

Early applications of Stirling engines focused primarily on CHP, where waste heat is recovered for space or water heating. Moghadam et al. [6] developed an energy–exergy–economic (3E) methodology for optimal sizing of solar dish Stirling micro-CHP systems across different climates. Their results confirmed that Stirling-based CHP systems can achieve high overall efficiencies, especially in solar rich regions.

3.2 Stirling Engines in Combined Cooling, Heating, and Power (CCHP)

More recent research expanded to CCHP, where recovered thermal energy also drives absorption or adsorption chillers to provide cooling. Cheng and Huang [7] designed and simulated a Stirling-based tri-generation system that achieved an overall efficiency of 91%. Importantly, this figure refers to the combined utilization of electricity, heating, and cooling outputs, not just solar-to-electric efficiency. This distinction explains why system-level efficiency values are higher than the 25–32% solar-to-

electric efficiencies typically reported for dish/Stirling systems [18].

3.3 Hybrid Stirling Systems

Hybridization strategies have been proposed to improve performance and reduce payback time. Sheykhi et al. [19] proposed a hybrid system combining a Stirling engine with an internal combustion engine, achieving a 12% increase in overall efficiency compared to stand-alone Stirling configurations. Such hybrid systems reduce economic risk by ensuring reliable operation during periods of low solar availability.

3.4 Advantages of Stirling Based CCHP Systems

Stirling engines present several advantages for CHP and CCHP:

- High efficiency across a wide range of operating temperatures.
- Fuel and heat-source flexibility (solar, biomass, hybrid).
- Scalability, from residential micro-CHP to district-scale tri-generation.
- Low maintenance and long service life due to external combustion.

They also provide important environmental benefits (see Sec. 5.3).

3.5 Limitations and Challenges

Despite these benefits, challenges hinder large-scale commercialization:

- High capital costs of solar concentrators and Stirling engines.
- Solar intermittency, requiring hybridization or storage solutions.
- Limited market penetration, as most studies remain at the simulation or pilot-project level.
- Ongoing technical challenges related to working fluid selection and regenerator optimization.

3.6 Relevance for Building Applications

For buildings, Stirling engines in CHP or CCHP systems can address simultaneous heating, cooling, and electricity demands (tri-generation). When integrated with HVAC, these engines serve as decentralized energy hubs, enhancing reliability and reducing dependence on imported electricity. For Afghanistan where grid supply is unreliable and HVAC loads are significant Stirling-based CCHP systems could transform building energy management when powered by the country's abundant solar thermal resources.

7. Solar Dish/Stirling Systems: Modelling, Simulation, and Experiments

Dish/Stirling systems are considered the most efficient solar thermal power technology, converting concentrated solar radiation into mechanical work via the Stirling engine. The modularity of dish/Stirling units makes them particularly suitable for decentralized building scale applications, where electricity, heating, and cooling can all be derived from a single solar collector.

In conclusion, this study emphasizes the importance of optimizing the aspect ratio to enhance Savonius turbine performance and provides a valuable contribution to the existing literature. The findings, supported by experimental data, also serve as a foundation for future research in this field.

These results demonstrate that blade geometry significantly influences torque performance in Savonius turbines. While classical designs provide a foundational benchmark, both helical and especially optimized hybrid configurations offer notable improvements in aerodynamic efficiency. Future research may focus on further refining hybrid blade geometries and testing them under variable wind speeds and turbulence intensities to determine their applicability in real-world environments.

ABBREVIATIONS

TSR - Tip Speed Ratio
Cp - Power Coefficient
Ct - Torque Coefficient
RPM - -Revolutions Per Minute
Nm - Newton meter
Cv - Moment coefficient
A- Front View Area of Turbine
D-Diameter of Turbine
H-Height of Turbine
ρ = air density
V = wind speed
ω = rotational speed of the rotor
R = rotor radius

6. REFERENCES

[1] Sheldahl, R.E., & Klimas, P.C. (1977). Aerodynamic characteristics of three- and four-bladed Savonius rotors. Sandia National Laboratories Report, SAND76-0432.

[2] Kamoji, R.S., et al. (2009). Experimental and numerical investigation of Savonius wind turbine performance. Renewable Energy, 34(6), 1570–1577.

[3] Ghafoorian, M., et al. (2025). Enhancing self-starting capability and efficiency of hybrid Darrieus–Savonius vertical axis wind turbines. Machines, 13(2), 87. https://doi.org/10.3390/machines13020087

[4] Hosseini Rad, M., et al. (2025). Aerodynamic performance of helical Savonius turbines. Energy Science & Engineering, 13, 345–360. https://doi.org/10.1002/ese3.70185

[5] Liu, Y., et al. (2019). Performance improvement of hybrid vertical axis wind turbines equipped with helical blades. Energy Science & Engineering, 7, 145–158. https://doi.org/10.1002/ese3.70185

[6] Ghosh, A., et al. (2019). Aerodynamic efficiency analysis of Darrieus-Savonius hybrid wind turbines. International Journal of Energy Studies, 9(4), 637–678.

[7] Bakırcı, M. (2024). Numerical investigation on torque performance of Darrieus–Savonius hybrid designs. International Journal of Energy Studies, 9(4), 637–678.

[8] Eftekhari, M., et al. (2025). Performance improvement of hybrid vertical axis wind turbines equipped with helical blades. Energy Science & Engineering.

[9] Kacprzak, K., Sobczak, K., & Wolski, P. (2013). Experimental investigation of Savonius wind turbine with a new blade shape. Renewable Energy, 60, 578–585.

[10] Saha, U.K., Thotla, S., & Maity, D. (2008). Optimum design configuration of Savonius rotor through wind tunnel experiments. Journal of Wind Engineering and Industrial Aerodynamics, 96(8–9), 1359–1375.

[11] Menet, J.L. (2004). A double-step Savonius rotor for local production of electricity: A design study. Renewable Energy, 29(11), 1843–1862.

[12] Altan, B.D., & Atilgan, M. (2008). An experimental study on improvement of Savonius rotor performance with curtain arrangement. Renewable Energy, 33(11), 2549–2553.

[13] Islam, M., Ting, D.S.K., & Fartaj, A. (2008). Aerodynamic models for Darrieus-type straight-bladed vertical axis wind turbines. Renewable and Sustainable Energy Reviews, 12(4), 1087–1109.

[14] Burton, T., Jenkins, N., Sharpe, D., & Bossanyi, E. (2011). Wind Energy Handbook. Wiley.

[15] Hau, E. (2013). Wind Turbines: Fundamentals, Technologies, Application, Economics. Springer.

[16] Manwell, J.F., McGowan, J.G., & Rogers, A.L. (2009). Wind Energy Explained: Theory, Design and Application. Wiley.

[17] M. B. Akkuş, Z. Haksever and S. Teksin, Experimental and Numerical Analysis of Savonius Wind Turbine with End Plate on Various Types, Energy, Environment and Storage, vol. 2, pp. 61-70, 2022.

[18] Z. Zhao, et al., "Research on the improvement of the performance of Savonius rotor based on numerical study," 2009 International Conference on Sustainable Power Generation and Supply, IEEE, 2009.

[19] Teksin S., Kurt M., Investigation of the Solidity Ratio in a Horizontal Wind Türbine, Energy, Environment and Storage, vol. 1 (2), pp. 11-16, 2021. https://doi.org/10.52924/ISEQ8001

[20] Akkus MB., Haksever Z., Osmanlı S., Investigation Of The Performance Changes Of The Savonius Wind Turbine Rotors With The Same Front View Area Of Look By Change Of The Aspect Ratio, Energy, Environment and Storage, vol. 2 (3), pp. 13-22, 2022. https://doi.org/10.52924/WFVI2347